2022

Molecular Modeling of High-performance Polymers

Sagar Umesh Patil
Michigan Technological University, spatil4@mtu.edu

MOLECULAR MODELING OF HIGH-PERFORMANCE POLYMERS

By

Sagar Umesh Patil

A DISSERTATION

Submitted in partial fulfillment of the requirements for the degree of

DOCTOR OF PHILOSOPHY

In Mechanical Engineering-Engineering Mechanics

MICHIGAN TECHNOLOGICAL UNIVERSITY

2022

This dissertation has been approved in partial fulfillment of the requirements for the Degree of DOCTOR OF PHILOSOPHY in Mechanical Engineering-Engineering Mechanics.

Department of Mechanical Engineering-Engineering Mechanics

Dissertation Co-advisor: *Dr. Gregory M. Odegard*

Dissertation Co-advisor: *Dr. Susanta Ghosh*

Committee Member: *Dr. Ibrahim Miskioglu*

Committee Member: *Dr. Gowtham S*

Department Chair: *Dr. Jason R. Blough*

Dedication

To my late granparents

Mr. Rohidas Narayan Patil and Mrs. Taraben Rohidas Patil

Mr. Rajaram Somji Patil and Mrs. Dwarkhaben Rajaram Patil

For their blessings. I know you are always watching over me and are certainly proud of me.

To my parents, teachers, family, wife and friends

For always supporting me, who didn't hesitate to criticize my work at every stage - without which I would neither be who I am nor would this work be what it is today.

Contents

List of Figures

List of Tables

Preface

This dissertation demonstrates the implementation of molecular dynamics to predict the interfacial and thermo-mechanical properties of high-performance polymers and their composites. The systems includes polyimides, epoxies and carbon-nanotubes. This type of analysis is useful in selecting polymer matrices to design next-generation materials for human mission to Mars. Additionally, it presents the accuracy and efficiency of Reactive Interface Force Field to simulate crosslinking and mechanical deformations to predict thermo-mechanical properties of epoxies as a function of curing. This data is to provide useful data for process modeling of composite in a multiscale framework. This dissertation should be of interest to anyone interested in polymer research and has curiosity to learn molecular dynamics.

Chapter 2 is published in Elsevier's journal of Computational Materials Science. Chapter 3 is published in ACS' journal of Applied Polymer Materials. Chapter 4 is partly published in ACS' journal of Macromolecules. Chapter 5 will be published as a journal article in the future.

Superior high-performance computing system at Michigan Technological University is used to generate all simulated results in the work. I really appreciate Dr. Gowtham's

help with this. I would like to thank our collaborators Dr. Marianna Maiaru's research group of $iCOMM^2$ lab at University of Massachusetts, Lowell for helping us with the experimental validation of predicted properties and micro-scale analysis. This research was made possible by the generous funding from NASA Space Technology Research Institute's (STRI) The institute for Ultra-Strong Composites by Computational Design (US-COMP), grant NNX17AJ32G and the NASA grant 80NSSC19K1246. I am also thankful to Mechanical Engineering-Engineering Mechanics department of Michigan Technological University for supporting my Ph.D. journey through graduate teaching and graduate research assistantships.

Acknowledgments

I would like to express my gratitude to my patient and supportive advisor, Dr. Gregory Odegard, who has supported me throughout this research project. Thanks for your belief and trust in me. I really appreciate your willingness to accept my impromptu meeting requests and answering my questions after office hours and during vacations.

To my committee members, Dr. Susanta Ghosh, Dr. Ibrahim Miskioglu and Dr. Gowtham S., I thank you for generously providing your knowledge and expertise on the subject matter. Dr. Gowtham for helping with the HPC related questions and for teaching the FOSS101 and Scientific Computing course which prepared me better for the research.

I also would like to say special thanks to Dr. Marianna Maiaru for her unwavering support and guidance on the research project. Your inputs and feedback really helped me be a better researcher.

I would like to extend my sincere thanks to Dr. Mia Siochi, Dr. Kristopher Wise, Dr. Benjamin Jensen and Dr. Jake Gissinger from NASA Langley Research Center for their continuous support and valuable feedback during our group meetings. Additionally, this endeavor would not have been possible without the generous support

from NASA's Space Technology Research Institute's, the Institute for Ultra-Strong Composites by Computational Design (US-COMP) and the NASA grant. I appreciate all the discussions and feedback from my colleagues and collaborators from the US-COMP institute.

From the bottom of my heart I would like to say big thank you for all the CMMR Lab research group members for their energy, understanding and help throughout my project, especially to Dr. Matthew Radue for his guidance at the beginning of my research and our fun lunch time talks. I also would like to say special thank you to Dr. Sorayot Chinkanjanarot, Dr. William Pisani, Dr. Hashim Al Mahmud and Prathamesh Deshpande, without your help and wise guidance this project would have not been the same! Prathamesh, I really appreciate all the time spent with you in the office. I am also grateful to my lab mates, Swapnil Bamane, Prashik Gaikwad, Ivan Gallegos, Joshua Kemppainen and Khatereh Kashmari for their moral support. Dr. Ashley Kaiser, I have learnt a lot from you. Thanks for sharing your knowledge and being a wonderful friend.

I had the pleasure of working/collaborating with the members of $iCOMM^2$ lab from University of Massachusetts namely, Sagar Shah, Michael Olaya, Evagenia Plaka and Kalima Bukenya. I really admire your willingness to share your knowledge on the microscale analysis and experimental characterization. I have learnt a lot from you guys.

My friends, my family away from home, Sarang Pakankar, Armin Kalita, Dr. Nabhajit Goswami, Dr. Shabnam Konica, Dr. Upendra Yadav, Ivan Gallegos, Utkarsh Chaudhari, Komal Chillar, Sushree Dash for always being by my side. Thank you for encouraging me, listening to me, and entertaining me. For letting me be ME. I am thankful of all the times spent together from early morning breakfasts to late night dinners and parties, long drives, camping and shopping trips. I love you all!

My parents, my understanding father Mr.Umesh Patil and my lovely mom Mrs. Sangita Patil, for giving me this wonderful life, always believing in me and loving me unconditionally. I did it!

My grandparents, Dr. Sakharam (Bapu dada) and Mrs. Asha Chaudhari (Acchi mummy) for their blessings.

My beautiful wife, Ankita. I love you. Thanks for your patience, understanding and joining me to the finish line. I cannot wait to start our journey together!

I would be remiss in not mentioning my family, my uncles and aunts, Mr. Madhukar (Appa) and Mrs. Karuna (Bhabhi) Patil, Mr. Shriram and Mrs. Maya Chudhari, Mr. Sachin and Shewta Chaudhari. My in-laws, Mr. Dinesh and Mrs. Sapna Chaudhari. My sisters and brother-in-laws, Mrs. Harshada and Mr. Harshal Patil, Mrs. Kalpana and Hiralal Patil. My brother and sister-in-law, Mr. Pankaj and Mrs. Suvarna Patil. My neices and nephews, Damini (tinu), Rohit, Kaushik, Parth (duggu), Swara and

Khush. My cousins, Kinu and kunal patal, Gaurish, Yashika, Vedant and Radhey. I love you all so much! Their belief in me has kept my spirits and motivation high during this process.

Lastly, to the almighty God!

Jay Siyaram, Jay Ambe

List of Abbreviations

MD	Molecular Dynamics
NASA	National Aeronautics and Space Administration
STRI	Space Technology Research Institute
US-COMP	Institute for Ultra-Strong Composites by Computational Design
LAMMPS	Large-scale Atomic/Molecular Massively Parallel Simulator
HPC	High-Performance Computing
CNT	Carbon Nanotubes
flCNT	Flattened Carbon Nanotubes
PMC	Polymer Matrix Composite
IFF	Interface Force Field
IFF-R	Reactive Interface Force Field
PCFF	Polymer Consistent Force Field
ReaxFF	Reactive Force Field
CHARMM	Chemistry at HARvard Macromolecular Mechanics
AMBER	Assisted Model Building with Energy Refinement
OPLS	Optimized Potentials for Liquid Simulations
COMPASS	Condensed-phase Optimized Molecular Potentials for Atomistic Simulation Studies

MM2	Molecular Mechanics 2
CFF	Consistent Force Field
MMFF	Molecular Modeling Force Field
CHAMBER	CHarmm $\leftrightarrow$ AMBER
DMA	Dynamic mechanical analysis
RMW	Reduced Molecular Weight
NPT	Constant Pressure and Temperature
NVT	Constant Volume and Temperature
fs	Femtoseconds
ps	Picoseconds
ns	Nanoseconds
C	Carbon atom
F	Fluorine atom
H	Hydrogen atom
O	Oxygen atom
N	Nitrogen atom
S	Sulphur atom
Si	Silicon atom
DFT	Density Functional Theory
LDA	local-density approximation
GGA	generalized gradient approximation

RDP	Registry Dependent Potential
CoM	center of mass
RDP	Registry Dependent Potential
PEEK	Polyether ether ketone
MPa	MegaPascal
GPa	GigaPascal
G	Shear Modulus
K	Bulk Modulus
E	Young's Modulus
ν	Poisson's Ratio
σ	Yield Strength
T_{g}	Glass Transition Temperature
CTE	Coefficient of Thermal Expansion
ϵ_{sh}	Volumetric Shrinkage
$\dot{\varepsilon}$	Strain rate

Abstract

High-performance polymers are extensively used in the aerospace and aeronautics industries due to their low density, high specific strength, and high specific stiffness. These properties along with better infiltration with reinforcements [carbon nanotubes (CNTs), glass etc.] capability make them an excellent candidate to fabricate Polymer Matrix Composites (PMCs) tailored for specific applications. The applications range from products that are used every day to deep space exploration. These materials are subjected to varying temperatures and pressures during fabrication and in service. Therefore, the evolution of their intrinsic properties needs to be studied and their ability to sustain extreme environmental conditions in outer space needs to be investigated. Utilizing experimental techniques for this purpose is time-consuming and expensive. Predictive computational tools like molecular dynamics (MD) can be used for such studies as they are quick and inexpensive relative to experiments. Furthermore, it reduces the overall time in designing and deploying the next generation of composite materials.

In this work, MD is implemented to model self-assembled stacks of flattened CNTs (flCNTs) and polyimide composites to investigate the interfacial properties at the interface between flCNT and polyimides. Fluorinated and non-fluorinated polyimides are compared based on interaction energy, friction force and transverse strength. The

reactive interface force field (IFF-R) is validated to predict thermo-mechanical properties of epoxies for varying degrees of cure. These nanoscale properties provide a set of inputs for microscale analysis to predict the evolution of residual stresses for process modeling of composites. In order to use nanoscale mechanical properties as inputs, they need to be corrected for the strain-rate discrepancy associated with several orders of magnitude difference between experimental and simulated strain rates. A phenomenological approach to account for this strain-rate difference is developed based on experimental characterization data. Once the MD properties are corrected, they can be used in microscale analysis to accurately predict residual stresses.

Chapter 1

Introduction

Due to the increased interest in deep space exploration that is to Moon and beyond, there is a need for light-weight, ultra-strong materials for human mission to Mars. The current state-of-the-art material that is Carbon fiber IM7 8552 cannot be used to construct the space vehicles utilized in much missions. Because they are unable to meet the demands of increased payload and they lack the required specific strength and toughness to be used as structural material. Mass reduction driven by material innovation is critical for deep space exploratory missions such as manned mission to mars.

CNT based composites are the key to develop such materials because of their high specific strength and stiffness. But the properties of individual CNTs do not scale well

to larges assemblages because of inadequate non-covalent interactions with neighboring circular CNTs which causes slippage during deformation, poor load transfer and excessive CNT agglomeration. In addition, the process modeling for these materials in important to find optimum curing cycles and manufacturer resins with improved properties.

Downes et al. [2] showed that CNTs can be self-assembled into flattened stacks of CNTs (flCNTs) to achieve large surface-to-surface contact area that resembles graphitic surface. flCNT based composites are the key to develop light-weight, ultra-strong materials. But, there are many unexplored avenues with flCNTs. Such as the optimal polymer to fabricate flCNT composites to improve load transfer, optimal manufacturing method, failure behavior etc. Computational modeling can provide insights into these avenues.

Epoxies are thermosetting polymers that are extensively used in aerospace industries because of their excellent thermal, mechanical and electrical properties. The understanding of processing of the fiber-reinforced epoxy composites is important to optimize curing cycles to produce materials with properties tailored for specific applications. Using experimental techniques to fully characterize the material to measure properties as the material cures is time-consuming and expensive. Atomistic simulations can be used for the process modeling of composites.

MD is being used to study the behavior of material at nano-scale since 1950s. The

properties of material at bulk level is highly dependent on the atomic arrangement and the interactions between them. Some of the applications of MD include investigating the molecular configurations of carbon nanotubes, polymer and protein chains arrangements, predicting thermo-chemo-electro-mechanical properties and much more.

In this work, MD is implemented to predict interfacial characteristics between flCNTs and polyimides presented in **Chapter 2**. The effectiveness and accuracy of IFF-R force field to predict the thermo-mechanical properties of epoxies at fully cured state was accessed in **Chapter 3**. A comprehensive set of thermo-mechanical properties of DGEBF/DETDA epoxy as function of degree of crosslinking and temperature is presented in **Chapter 3**. Insights into the material behavior at nanoscale such as gelation, effect of cooling rate on the molecular configurations, effect of viscous nature of epoxies on properties are discussed in details. A phenomenological method to account for the strain rate discrepancy in MD predictions of mechanical properties is discussed in **Chapter 5**. In the last, the overall conclusions from this work are presented in **Chapter 6**.

1.1 Molecular Dynamics

Every MD recipe requires certain sets of inputs to execute. **Figure 1.1** shows the schematic of a MD simulation. First, the molecular structure and the overall composition of the system of interest. All the constituents needed to be modelled in order to get reliable outputs. Second, the initial position and velocities of atoms. Lastly, the force field that describes all the atomic interactions between these atoms and molecules. The choice of the force field based on the objectives of the work is crucial to get accurate results. The output consists of all the interactions resulting from the molecular motion, that is the energies between atoms, bulk-level properties of the systems and much more. This cycle from input to output based on the desired applications is described in all the chapters.

The LAMMPS [3] open source software to execute all the MD simulations. The MD simulations uses Newton's second law of motion to evaluate the forces that arises as a result of molecular motion. The trajectories thus obtained at each time increments are solved using numeric techniques. The choice of algorithms depends on the force field, atomic positions and bonding between atoms. The thermodynamics of the system is also accounted by applying microcanonical ensembles based on the modeling environment. The details of algorithms, ensemble, inputs and outputs can be found in the LAMMPS [3] documentation.

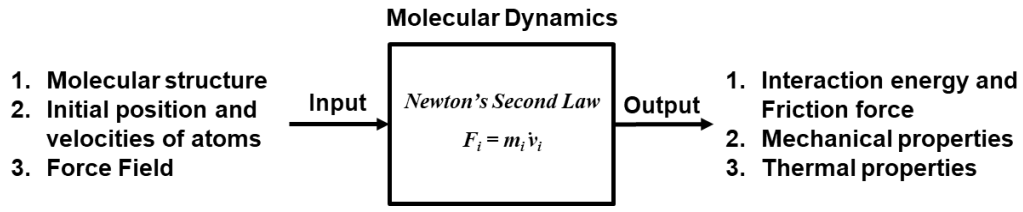

Figure 1.1: Molecular Dynamics (MD) Recipe

1.1.1 Learning Resources

Following are the resources to learn the principles of Molecular Dynamics (MD): [4–11]

1.2 Force Field

As discussed earlier, a force field is the major component of the MD simulation that describes all the interactions between the atoms and between the molecules present in the simulation cell. The force fields are classified into two major categories: fixed-bond force fields that allows stretching of bonds but does not allow bond formation or dissociation and reactive force fields that allows both bond formation and bond dissociation. The choice of force field is based on the project objectives and the systems (polymers, metals, ceramics etc) under study. **Chapter 3** discusses different force fields and provides a brief comparison. In this work, both fixed-bond and a

reactive force field is implemented. The following sections describes them in brief and more details are provided in the subsequent chapters.

1.2.1 Interface Force Field

The Interface Force Field (IFF) [12] was shown to accurately model organic-inorganic interfaces. IFF can be easily added to any fixed-bond force field like PCFF or CVFF. It is a class II force field which includes cubic, quartic and improper energy terms.

1.2.2 Reactive Interface Force Field

The Reactive Interface Force Field (IFF-R) [13] is an reactive version of IFF, where the bond dissociation is implemented using morse potential. IFF-R is computationally efficient than any other reactive force fields. Also, it efficiently models larger MD models of more than 30,000 atoms. Both IFF and IFF-R are validated in this work to predict bulk level thermo-mechanical properties of polymer systems.

Chapter 2

Interfacial Characteristics of Polyimide/flCNT composites

2.1 Introduction

New lightweight and strong structural materials are in demand for evolving aerospace vehicles. Mass reduction driven by material innovation is critical, for example, for human missions to Mars. It is estimated that the fuel mass required for a round trip to Mars may be up to 300 *lbs* per pound of vehicle mass [14]. Therefore, significant mass savings are necessary to make such missions affordable and to gain a margin for increasing payload.

To meet the challenge of developing exceptionally stiff and strong materials for aerospace applications, focused effort has been invested in engineering carbon nanotube (CNT)-based composites that exploit the outstanding mechanical properties of individual CNTs. However, individual CNT stiffness and strength values have generally not transferred well to large-scale assemblages. One weakness of CNT assemblages is the inadequate non-covalent interactions between adjacent circular CNTs, which leads to slippage of CNTs during deformation [15]. A recent fabrication method reported by Downes et al. [2] resulted in unique self-assembled stacks of flattened CNTs (flCNTs), which maximizes the contact area between CNTs, and thus the magnitude of non-covalent bonding. Additionally, Jolowsky et al. [14] demonstrated that this method is easily scalable to macro-scale composite panels resulting in excellent mechanical properties and load transfer.

The flCNT/bismaleimide (BMI) samples produced by Downes et al. [2] demonstrated excellent CNT alignment and long-range order. However, even though the CNT-CNT contact was enhanced by the induced flattening and stacking, the TEM-observed fracture surfaces evidenced intra-stack sliding in addition to complete stack pullout. Therefore, it appears possible that the mechanical properties of this flCNT based nanocomposite may be further enhanced by carefully engineering the interfaces. Moreover, the importance of dynamic interfacial friction within a CNT network has been revealed in a recent mesoscale modeling study by Wang et al. [16]. The employed mesoscopic distinct element method developed for CNT assemblies includes

a viscous friction model between CNTs (where friction force depends linearly on velocity), which can be directly calibrated from MD results [17]. Through exploratory modification of the CNT-CNT friction strength, Wang et al. demonstrated that enhancing the friction between tubes is a promising route toward achieving greater network strength [16]. While forming flattened CNT stacks may partly enhance friction within a CNT network due to the increased CNT-CNT contact, further improvements may be made by introducing the right kind of polymer to improve the interfaces. It is well-understood that the interfacial strength between the matrix and nanofiller has an important effect on load transfer in CNT-based composites [18–25]. Therefore, it is important to explore these flCNT/polymer interfaces to provide insight into the behavior of such systems.

Molecular Dynamics (MD) provides a way to analyze and design such interfaces on the molecular level. Simulations of a single CNT being extracted from a polymer matrix have been performed to determine the interfacial shear strength [20, 26–36] for direct comparison with experimental CNT pullout tests [37–39]. Within this modeling framework, one can directly modify the CNT-polymer interface, even with modifications that are extremely difficult or impossible to control in experiment, to predict the consequences on the interfacial strength. Moreover, MD has been effectively used to study the role of functionalization [26, 28, 32, 33], CNT geometry [29–31], CNT defects [33, 36], and polymer matrix [28, 35] on the interfacial strength. Additionally, molecular modeling has been applied to understand the friction of carbon interfaces, such

as, contact between CNTs or between the layers of a multi-walled CNT (MWCNT) [40–45] and diamond-diamond contact [46–51]. A critical factor in assessing the friction behavior is the commensuration between surfaces, that is, whether the lattices sliding against each other are aligned (commensurate) or misaligned (incommensurate) [40, 44, 52]. Researchers have used various experimental [19–21, 53–58] and MD [59–63] techniques to provide insight into the effect of pull-out tests on the interfacial properties in single-walled (SWCNT), double-walled (DWCNT), and MWCNT polymer composites. Although these studies have provided significant insight into CNT interfacial behavior, the behavior of flCNT/polymer interfaces has not yet been fully explored.

The objective of this study is to predict, prior to experimentation, the potential effects of infusing polymer into an assembly of flCNTs. The polymers of choice here are two aromatic thermoplastic polyimides and the composite systems are screened using three metrics:

1. the interfacial interaction energy,
2. dynamic interfacial friction behavior, and
3. transverse strength of the flCNT-polyimide interface.

The influence of the specific polyimide monomer structure on these metrics is discussed.

2.2 Molecular Modeling

The details of the MD simulation are discussed in this section. The LAMMPS software package [3] was used for all simulations discussed in this paper. The PCFF-IFF force field [12, 64, 65] was used to describe the interatomic forces in this study, as it was previously shown to yield accurate results for flCNTs [66] and contains all of the atoms types associated with the simulated polymer systems.

2.2.1 Polymer Systems

High-performance polyimide-based composite materials are extensively used in aerospace applications because of their excellent mechanical properties and high glass transition temperature (T_g) [67–69]. Although there are many experimental studies demonstrating the processing of aromatic polyimides [69], there are very few molecular modeling studies [70–75] exploring the influence of their molecular structure on the mechanical properties and reinforcement interface characteristics. In this work, two aromatic polyimides, NASA Langley Research Center's Colorless Polyimide 1 (LaRC CP1) and Huntsman Corporation's Matrimid 5218 (M5218) are modeled using MD. LaRC CP1 is a product of 4, 4 - (hexafluroisoroylidene) diphthalic anhydride (6 FDA) and 2,2 – bis [4-(4-aminophenoxy) phenyl] hexafluoropropane (BDAF),

whereas M5218 is a product of 3,3',4,4'-Benzophenonetetracarboxylic dianhydride (BTDA) and 4,6-diamidino-2-phenylindole (DAPI). **Figures 2.1** and **2.2** show the skeletal and molecular structures of both polyimides, respectively. LaRC CP1 is fluorinated ($-CF_3$ group) with 90 atoms/monomer, whereas M5218 is non-fluorinated with 62 atoms/monomer. The two systems were chosen to study the influence of fluorine atoms on the interfacial characteristics of the composites. For simplicity, herein LaRC CP1 will be referred to as "Fluorinated polyimide" and Matrimid 5218 will be referred to as "Non-fluorinated polyimide".

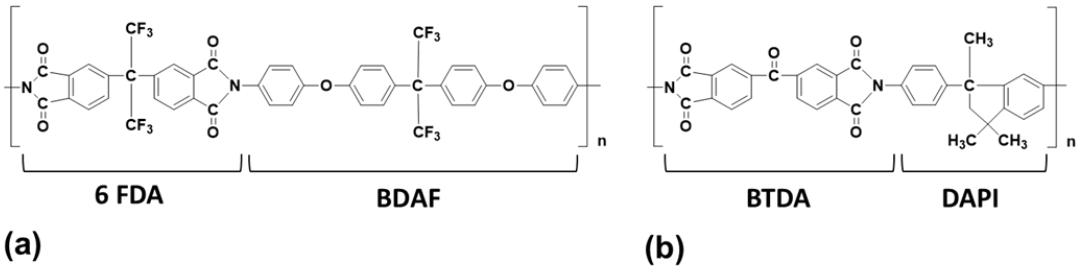

Figure 2.1: Skeletal structures of (a) Fluorinated polyimide and (b) Non-fluorinated polyimide.

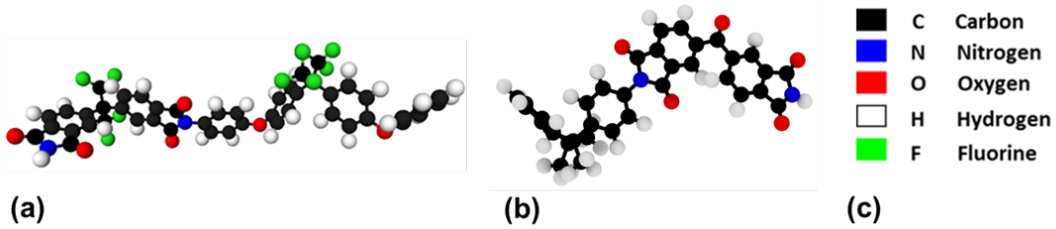

Figure 2.2: Molecular Structures of (a) Fluorinated polyimide and (b) Non-fluorinated polyimide monomers after molecular minimization under periodic boundary conditions in LAMMPS. (c) The color coding used for all the MD models.

In addition, PCFF-IFF is implemented in this study because of its accurate charge

assignment as charges have a significant effect on the interface properties and conformations of polar molecules. The charges are assigned based on various factors such as experimentally-measured electron densities and dipole moments as described in detailed elsewhere [12, 76]. PCFF-IFF is a class II force field in which the partial charges on atoms are calculated as per Extended Born rule [76, 77] based on bond increments. The detailed charge distribution on the polyimides shown in **Figure 2.1** can be found in the supplementary information (**Appendix A.1**).

2.2.2 Model Setup

Figure 2.3(a) shows a representative MD model where each flCNT is modeled as graphitic bi-layers, representing the key flattened portion. The rounded ends of the flCNTs are omitted in this setup, but are depicted for clarity by the dashed curves in **Figure 2.3**(b). Although the rounded ends connecting the bi-layers are not explicitly included, the model is not restrictive for the interfacial friction simulations. This is because the bi-layers translate together during the friction study described in **Section 2.4** approximately treating the layers as connected. The infiltrated polymer is modeled as complete layers located between the bi-layers. Note that boundaries are periodic in three dimensions, and therefore, the polymer regions at the top and bottom make up one layer. This layered setup was chosen to represent the basic features of the sp_2 carbon-polymer interaction, friction, and transverse strength. When thick

polymeric layers are considered, the described setup can offer fundamental insights into the interfacial features that are also present in a real system with polymeric material located between whole flCNT stacks [2].

The workflow implemented in LAMMPS to build the MD models of flCNT combined with fluorinated and non-fluorinated polyimides for all mass fractions includes the following steps:

1. Each isolated monomer of both polyimide systems was assigned PCFF-IFF parameters and modeled with two end hydrogen atoms to neutralize the partial charges on the molecule (**Figure 2.4**, step 1). These hydrogen atoms were deleted after polymerization. A molecular minimization simulation was run by using the `minimize` command in LAMMPS using the conjugate gradient (CG) algorithm to establish the equilibrium structures. In this paper, the term "equilibrium" implies that the molecular system is stable and at a minimum potential energy state. In step 1, the system consists of only the isolated monomer. In step 5, the model contains only polyimide monomers in the liquid phase, then after polymerization the system is in the solid phase.
2. An individual monomeric layer was first built without including the flCNT. The monomers were placed in a simulation box (**Figure 2.4**, step 2). The monomers were replicated to a desired mass fraction. Here, the mass fraction is defined as the ratio of molecular mass of polymer to the total molecular mass of the

system that includes the polymer as well as flCNTs. In this work, different models for mass fraction ranging from 10 % to 60 % were individually built for both monomers with sizes ranging from 30,000 – 60,000 atoms. The x and y dimensions were set at 101 and 51 $\mathring{A}$, respectively, since in a forthcoming step, a 101 $\times$ 51 $\mathring{A}$ pseudo-flCNT layer consisting of 23,616 atoms would be inserted, needing to completely span the x and y lengths. The z dimension was adjusted for the different mass fractions while the x and y dimensions remained the same to provide the same contact area between the polymer and flCNTs. After replicating the monomers, a molecular minimization simulation was run.

3. The monomers were densified to a targeted mass density of 1.2 g/cc (**Figure 2.4**, step 3). This density value was chosen as an initial guess, with the final mass density achieved in a subsequent step. This densification simulation was performed for 500 ps at 300 K using the `fix deform` command in LAMMPS, where the z dimension was gradually reduced at a rate of 10 $\mathring{A}/ns$. The dynamic run of 500 ps was enough to randomize the monomers. A video clip of the simulation of non-fluorinated polyimide (46 % mass fraction) rendered using OVITO [78] is included as a part of supplementary information (**Appendix A.2**). The video shows that the molecules displace and start dynamic motion as soon as the simulations starts. Also, the supplementary information document ((**Appendix A.2**) [79]) includes top view snapshots of the model at 0^{th}, 5^{th} and 45^{th} timestep. A 1.0 fs timestep was selected for all simulations in

this study. The box boundaries were non-periodic and reflecting using the `fix wall/reflect` command in LAMMPS such that they could be effectively placed between flCNTs in the subsequent step. Previous studies have demonstrated that densification simulations on complex monomers using these conditions results in uniform bulk MD models that predict accurate physical, thermal, and mechanical properties [80–83].

4. The single densified monomer layer was duplicated, creating a second identical layer. The duplicated layer was created to enable friction simulations. It was not necessary to create independently equilibrated second polymer layer for the friction simulations. The two layers were placed in a periodic simulation box at a separation of 10 $\mathring{A}$ in the z-direction. At this step, periodic boundaries were applied in three directions. However, the simulation box was bounded by the dimensions of the flCNTs (101×51 $\mathring{A}$) in the xy-plane. Thereby open regions were formed both below and above the layers. The flCNT layers were inserted into the openings to fashion the setup shown in **Figure 2.4** (step 4). This approach placed the monomer and flCNT layers immediately in close contact to keep the flCNT flat. Upon assembling the layers with a close fit, an energy minimization was performed.
5. The model was brought into motion by running a 100 ps simulation in the NPT ensemble, and the temperature and pressure were set to 300 K and 1 atm, respectively. An annealing simulation was performed to further drive the

monomer configurations to a structural equilibrium. Annealing was carried out by simulating the model at 750 K for 100 ps and then cooling it back down to 300 K over 6 ns, resulting in a cooling rate of 75 K/ns. The maximum temperature was selected to be greater than the glass transition temperature of the two polyimides. To allow the box volume to adjust for the changes in temperature, a barostat was set to maintain a pressure of 1 atm. The flCNT/monomer composite was equilibrated for 3 ns at 300 K and 1 atm to prepare for room temperature property prediction (**Figure 2.4**, step 5). The Nose-Hoover thermostat and barostat [84–86] were used for all the simulations described herein. The average pressure was maintained at 1 atm. After this stage, the model still contains polyimide monomers, hence the next step is polymerization.

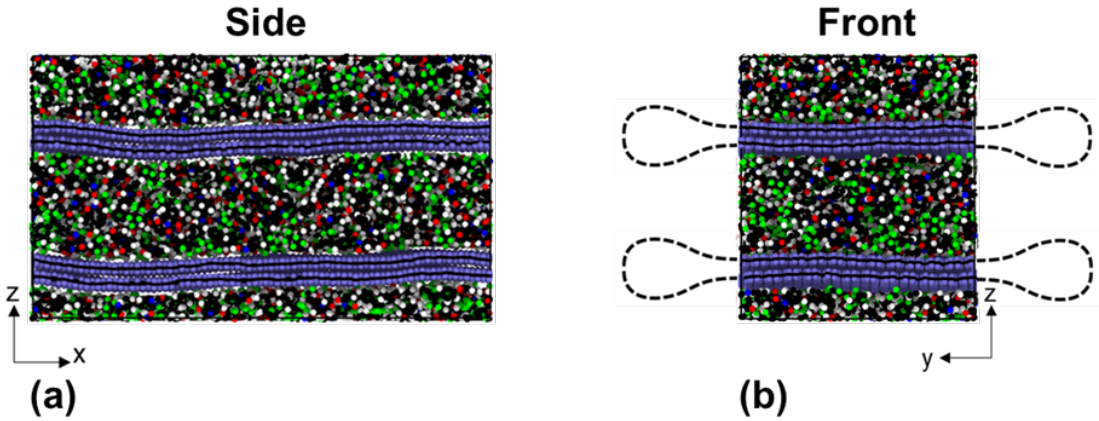

Figure 2.3: Representative model setup for the flCNT/Fluorinated polyimide composite (a) side view (b) front view showing the side lobes of flCNTs. The blue atoms attached to the flCNT carbon atoms represent the virtual π electrons.

It is important to note that previous studies employed course-grained models to allow

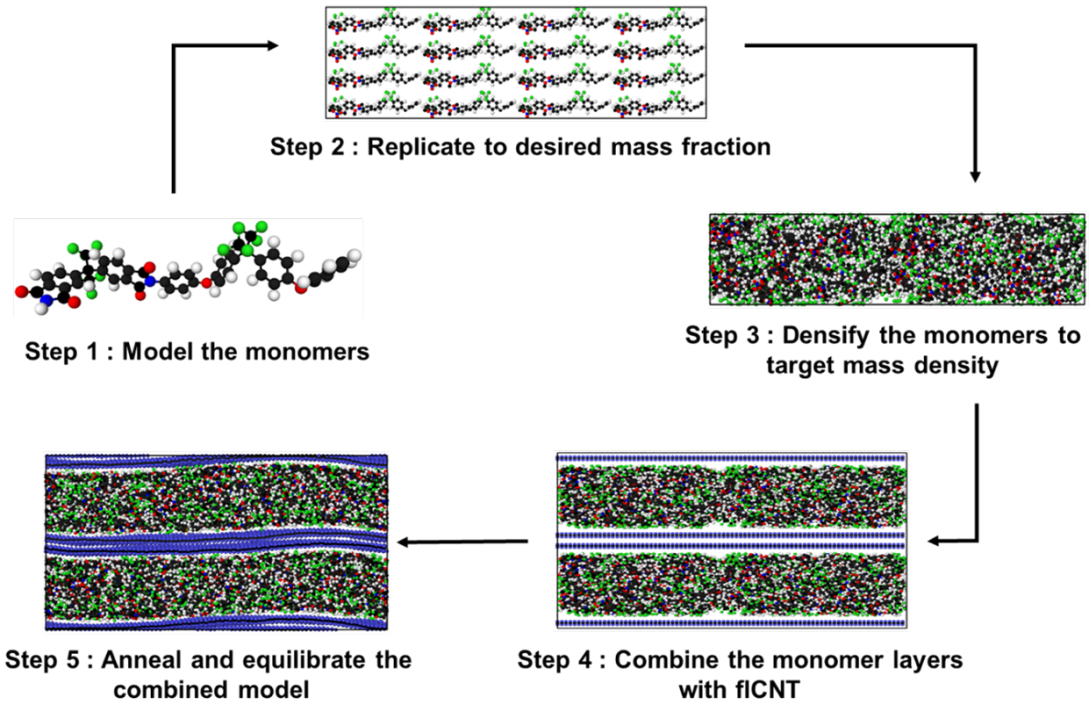

Figure 2.4: MD workflow to build the models for varying mass fractions. A representative fluorinated polyimide system is shown.

for higher effective relaxation times for interfaces [87–90]. Although these types of approaches may be useful for simpler monomer and interface structures, they do not capture the fine details that are required for this research that have a large influence on the predicted properties. Specifically, the full atomistic information is needed to capture the influence of the $-CF_3$ groups, particularly the partial charges on the C and F atoms. Also, some of the polymer layers studied herein are relatively thin and need the full atomistic information to accurately capture their molecular structure.

2.3 Polymerization

The polyimides undergo addition polymerization as they are linear-chained thermoplastics. The polymerization simulations were performed when the monomers were in the presence of the flCNTs to accurately capture interphase structures in the composite. Specifically, polymerization was performed using the `fix bond/react` command in LAMMPS [3]. Pre-reaction and post-reaction templates were made as specified by Gissinger et al. [91]. The total simulation time for polymerization was 4 ns, with the timestep set to 1 fs. Polymerization was carried out at 650 K in the NVT ensemble. The elevated temperature was used to thermally mobilize the atoms and increase the rate of reaction. The bond cutoff distance was set to 6 $\mathring{A}$. Reactions were permitted at any timestep, but the overall polymerization was controlled by setting the reaction probability to 0.99. As demonstrated by Gissinger et al. [91] the probability of 0.99 was used to create maximum bonds as per the templates. The temperature, bond cut-off distance, and probability were chosen to achieve maximum polymerization. The supplementary information document (**Appendix A.3**) includes the details about various simulations run at different settings of temperature and cut-off distance. Nevertheless, a clear plateau in the conversion of reactive groups was observed indicating that polymerization was permitted to run for a sufficient amount of time. As designed into the `fix bond/react` command, an `nve/limit` thermostat was used to moderate the kinetic energy of reacting atoms [91]. This thermostat was applied to atoms

included in the reaction templates for a predetermined number of steps following an initial bonding event. The stabilization thermostat was applied for 1000 steps. Both the fluorinated and non-fluorinated polyimide monomers were polymerized using the same settings to maintain consistency in the procedure. The hydrogen atoms in the model were deleted at the end of the simulation. After polymerization, annealing was again performed at 750 K for 100 ps followed by cooling back down to 300 K over 6 ns, resulting in a cooling rate of 75 K/ns. **Figure 2.5** shows the density profile of both polyimides after polymerization for similar mass fractions. The average mass densities of fluorinated and non-fluorinated polyimides far from the flCNTs is 1.43 g/cc and 1.20 g/cc, respectively. The experimental densities are 1.54 g/cc [92] for the fluorinated polyimide and 1.20 g/cc [93] for the non-fluorinated polyimide. Because PCFF-IFF has never been validated for the prediction of bulk densities of polyimides to the authors' knowledge, the difference in mass densities for each system is attributed to the inaccuracy of PCFF-IFF in predicting bulk density of polyimides.

Table 2.1 lists the molecular masses of the fluorinated and non-fluorinated polyimides after polymerization. As expected, the molecular mass of the polymer increases with the polymer mass fraction. The molecular masses of flCNTs in each model are same, which is 94,552.2 gm/mol.

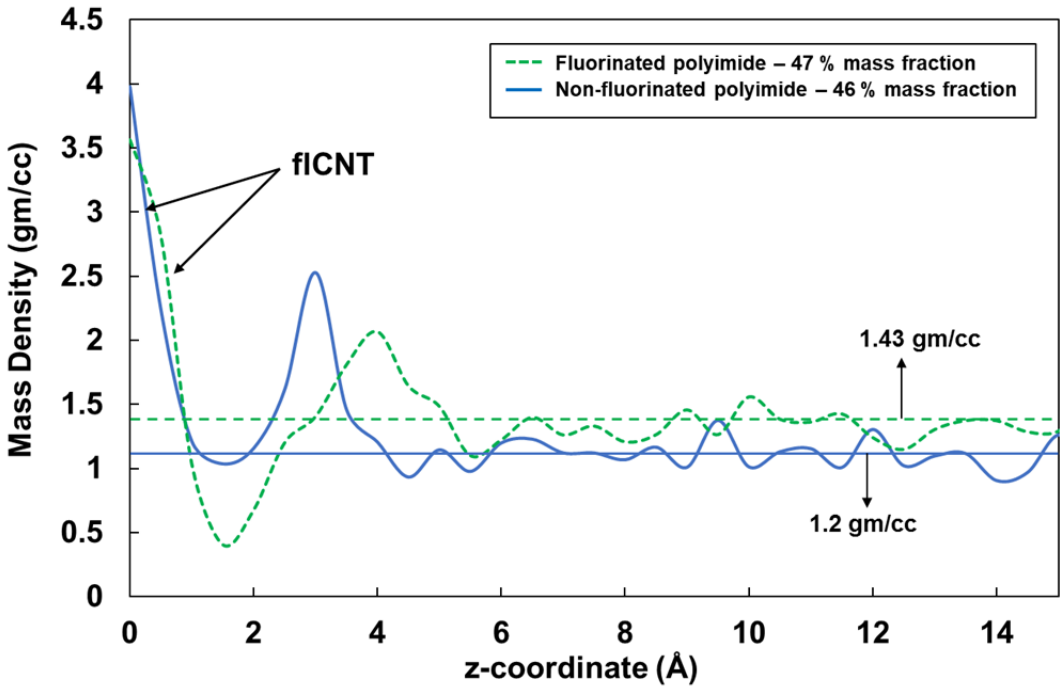

Figure 2.5: Mass density profiles after polymerization. The coordinate z = 0 corresponds to the center of the surface of the flCNT.

2.4 Interaction energy

After the polymerization and annealing steps, the models were simulated for 3 ns at 300 K and 1 atm using the NPT ensemble to compute the interaction energies between the polyimide layer and flCNT. The polyimide atoms were assigned to a group and the flCNT carbon atoms were assigned to another group. The interaction energy included the long-range interactions and used the `compute group/group` command. Similarly, the interaction energy was also computed for monomers prior to polymerization. This was done to reveal the role of polymerization on the interaction between the

Table 2.1
Molecular masses of fluorinated and non-fluorinated polyimides after polymerization.

Fluorinated polyimide		**Non-fluorinated polyimide**	
Mass fraction (%)	**Molecular mass** (gm/mol)	**Mass fraction** (%)	**Molecular mass** (gm/mol)
23	29,688.1	16	35,456.7
38	118,697.8	27	70,814.6
47	178,031.6	36	106,243.1
55	237,369.5	43	141,633.3
57	267,015.2	46	159,312.3
60	296,673.0	51	199,135.3
		54	221,255.2
		59	273,558.9

polyimides and flCNTs. The interaction energy was computed for each model with varying mass fractions.

2.5 Friction Simulations

Atomic friction arises from the atoms in a surface passing through a fluctuating potential induced by the atoms in a neighboring surface. When the surfaces are lattices, the non-bonded potential near the surface is periodic. When a surface slides in this periodic potential, atomic vibrations can be excited, which generally disrupts the collective sliding motion. In this way, energy put into sliding is dissipated via random atomic vibrations, and continued force must be applied to maintain constant-velocity sliding.

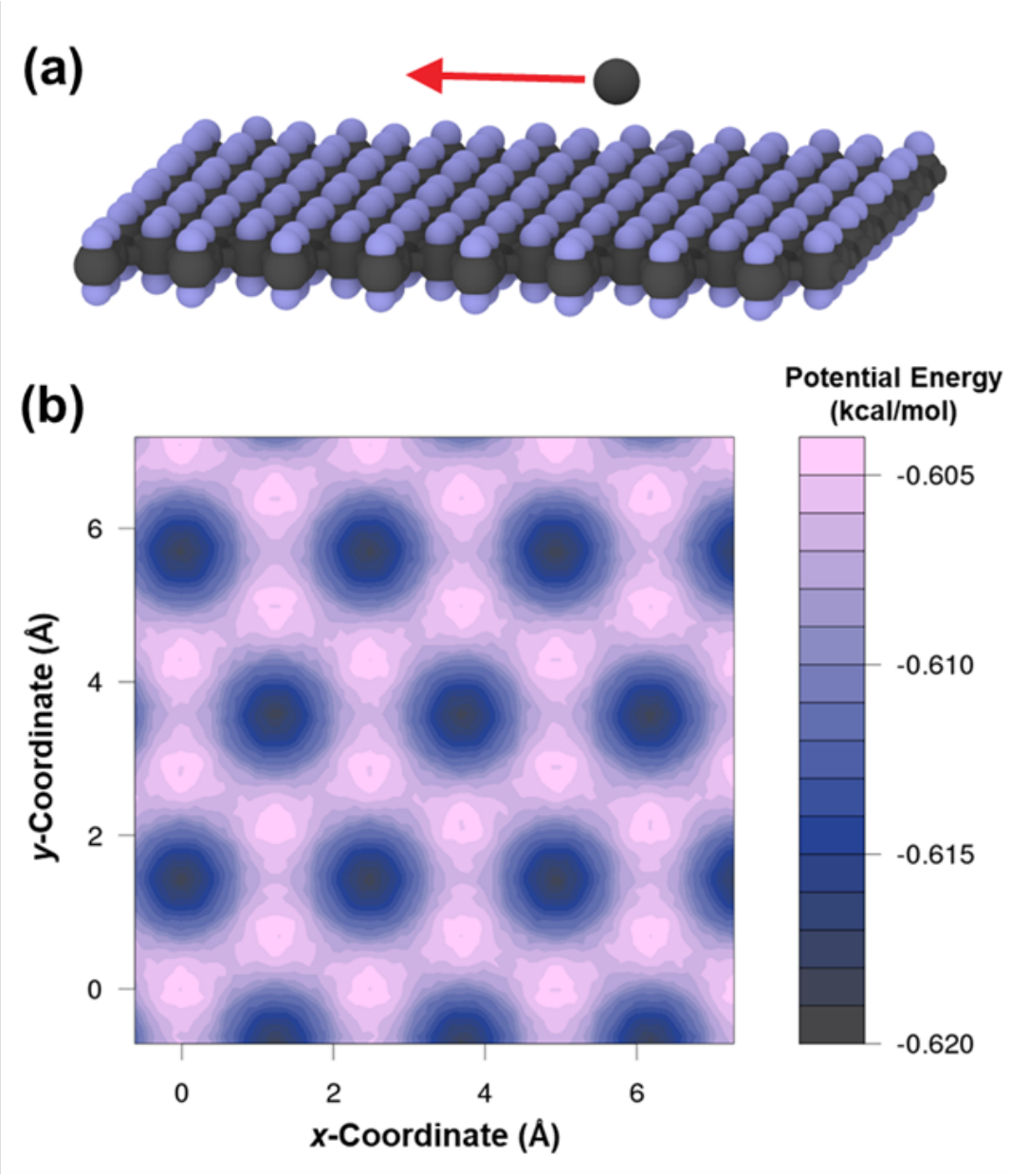

Figure 2.6: Scanning a neutral carbon atom over graphene with PCFF-IFF. The traversing atom is at a fixed distance (3.4 $\mathring{A}$) normal to the graphene plane. (a) Depiction of example. (b) Resulting potential energy surface.

As shown in **Figure 2.6**, the PCFF-IFF force field captures the general features of the pitted potential energy surface. In this case, a neutral carbon atom is scanned over graphene while remaining at a distance of 3.4 $\mathring{A}$ normal to the graphene plane.

Because the traversing atom is uncharged, the potential energy variations arise from the Lennard-Jones non-bonded potential. Larger potential energy variations are observed when the scanning atom is given a negative charge, adding repulsion with the virtual π orbitals. Even though the Lennard-Jones potential produces an uneven potential energy surface, the hills and valleys are small (about 0.015 $kcal/mol$ difference between the maximum and minimum energies). To examine the height and depth of the PCFF-IFF non-bonded energy, a helpful comparison can be made in the context of graphite and its stacking configurations. The energy between graphitic layers is dependent on the alignment of the atoms in adjacent layers. The highest energy configuration (AA stacking) occurs when the atoms exactly overlay the atoms in the next layer. Offsetting adjacent layers produces lower energy configurations, such as the AB stacking. This is known as the registry effect, or corrugation. Kolmogorov and Crespi computed the energy difference between the AA and AB stackings using DFT [94], which is reproduced in **Figure 2.7**. The local-density approximation (LDA) [95, 96] and generalized gradient approximation (GGA) [97] exchange-correlation functionals were used. Both functionals yield similar overall results. For the interest of this study, the stacking energy difference predicted by PCFF-IFF is added to compare with the DFT. These are molecular minimization simulations. For both the AA and AB stacking configurations, periodic boxes were used. The AA stacking configuration can be represented by a cell of one graphitic layer. To set the interlayer distance, the molecular minimization was performed while keeping the out-of-plane cell dimension

fixed. The AB stacking configuration has a period of two layers. A two-layer cell was made and again the out-of-plane cell dimension was set to control the interlayer distance. During minimization, the two-layer cell-maintained AB stacking, since it is the most energetically favorable configuration.

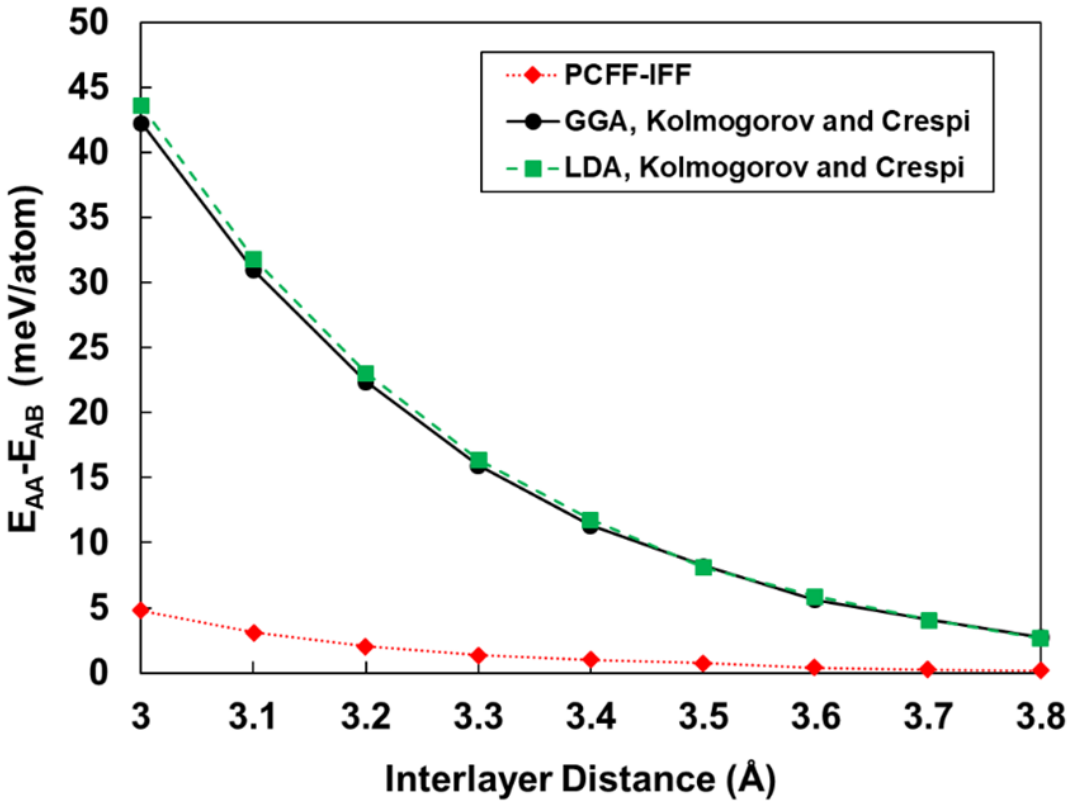

Figure 2.7: Energy difference between AA and AB stacking configurations of graphite. The DFT data is obtained from Kolmogorov and Crespi [1]. In the Kolmogorov and Crespi paper, two exchange-correlation functionals were used for generating the DFT results, namely, the local-density approximation (LDA) and generalized gradient approximation (GGA). Here, the energy difference predicted by PCFF-IFF is included to compare with DFT.

The data reveals that PCFF-IFF underestimates the magnitude of the registry effect, in spite of the inclusion of the virtual π orbitals. In general, Lennard-Jones potentials

are not suitable for reproducing the magnitude of the registry effect [94]. In order to accurately capture the registry dependence, a fundamentally divergent non-bonded potential is required, such as the Kolmogorov-Crespi Registry Dependent Potential (RDP) [94]. While the RDP is fit for modeling the friction forces between sliding flCNTs [44], its main limitation is that it is a carbon-only potential and cannot be applied to polymers. Ideally, a potential that can accurately approximate the registry effect and is broad enough to be applied to polymers is required. This would give an opportunity to approximate the π-π interactions between the aromatic rings in polyimides and the flCNT surface. In view of the available potentials, the small registry effect in PCFF-IFF is accepted cautiously, and therefore qualitative comparisons are made in this work.

Figure 2.8 shows a schematic of the friction simulation. To analyze the interface under sliding contact, simulations were performed in which one flCNT was displaced at a constant average velocity in the x-direction. It is important to note that these simulations refer to kinetic friction. Each flCNT layer (red and blue layers shown in **Figure 2.8**) was first defined like a non-periodic flake by grouping the atoms together as they were positioned in the initial simulation box. The center of mass (CoM) of this flake-like group was calculated. As the simulation progressed, the sliding atoms passed through the periodic boundary and yet the atomic positions were tracked as being in the next periodic image by use of image flags in LAMMPS. Therefore, the CoM of the flake-like group also shifted. The CoM, as defined in this manner, was

used to dictate the pulling force. A point moving in space (black dot on the bottom layer in **Figure 2.8**) at a constant velocity was also defined. The flCNT CoM was tethered to the moving point by applying a force proportional to the distance between the CoM and the moving point. This spring-like force was applied to all atoms in the layer to ensure that the CoM mainly followed the moving point at the same average velocity. The `fix spring` command in LAMMPS was used to execute the described velocity-controlled sliding. In the same manner, the other flCNT (top red layer in **Figure 2.8**) was fixed by tethering its CoM to the x and y-coordinates of the box center. For all spring forces, the spring constant was set to 0.7 nN/nm. Alternative methods exist for implementing velocity-controlled sliding. For example, the trajectories of a subgroup of flCNT atoms can be directly imposed; however, this disables the vibrations that these atoms would normally experience. The advantage of the method selected in this study is that all atoms are allowed to be in full motion.

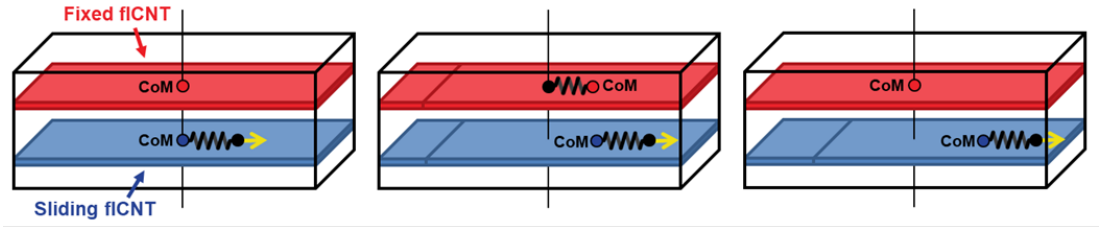

Figure 2.8: Schematic of friction simulation.

Each sliding case was simulated for 2 ns. Over the course of the simulation, the force on the sliding flCNT exerted by the polyimide layer was computed using the `compute group/group` command in LAMMPS, and the x-component of the force was taken as

the friction force. A time-average was calculated of the friction force throughout the simulation. In the same manner, the friction force between the fixed flCNT and the polyimide layer was also recorded. With the friction forces on both the sliding and fixed flCNTs, the magnitudes were averaged together to obtain the final friction value. **Figure 2.9** shows displacements of the flCNTs and polyimide layers plotted from a representative friction simulation. In this case, the sliding flCNT was prescribed a velocity of 100 m/s (1 $\mathring{A}/ps$), resulting in a total displacement of 1000 $\mathring{A}$ at the end of the simulation. The polymer layers were allowed to slide in the same direction, but due to the contact between the fixed flCNT and the polymer, it displaced at roughly half the velocity as the sliding flCNT in this case. The results are consistent for both the polyimides.

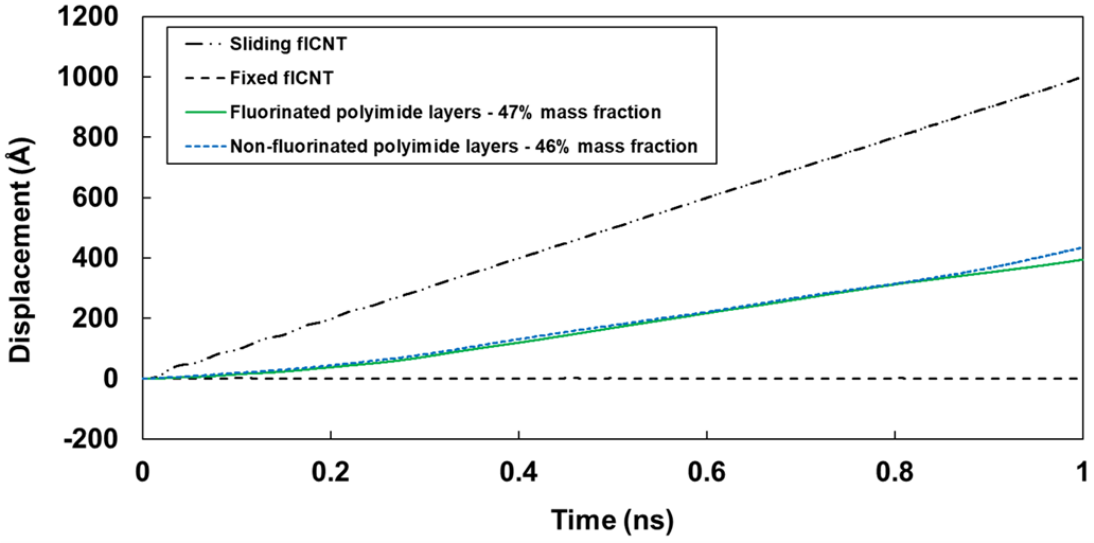

Figure 2.9: Displacement of flCNTs and polyimide layers during representative friction simulations. In this example, the sliding flCNT was prescribed a velocity of 100 m/s (1 $\mathring{A}/ps$).

The bare flCNT sliding simulations were performed in a similar manner to the flCNT-polymer simulations, with some minor differences. The commensurate model consisted of two flCNTs placed in a periodic cell. A molecular minimization was executed, and then the model was equilibrated with the NPT ensemble for 2 ns at 300 K. For this, the sliding flCNT was pulled along the zigzag direction. The incommensurate model consisted of two flCNTs in periodic cell. For one flCNT, the lattice was rotated an 10.9° angle relative to the other flCNT lattice. The box size was selected to closely match the commensurate model, and the angle was chosen to reduce the mismatch in length and width between the flCNTs. One flCNT was displaced at a constant average velocity in the x-direction by tethering the flCNT to a moving point traveling at a constant velocity. The other flCNT was held in place by tethering it to a fixed point. Tethering was accomplished by applying a spring force (with 0.7 nN/nm spring constant) proportional to the distance between the flCNT CoM and the point. The sliding simulation was executed for 1 ns. The friction force was computed as the time-average of the x-component of the force on the sliding flCNT exerted by the fixed flCNT. The average was taken over the entire duration of the simulation.

For both flCNT/polyimide and flCNT/flCNT friction simulations, similar barostat and thermostat settings were implemented. The Nose-Hoover thermostat and barostat [84–86] were used for all the friction simulations. The motion is damped by setting a barostat to apply 1 atm in all dimensions with a damping factor of 1000 timesteps while the thermostat was set with damping factor of 100. Increasing the

pressure in the z-direction forced the sliding surfaces closer and resulted in increased friction, which has been demonstrated in previous studies [46–49]. For controlling the temperature, only the fixed flCNT was thermostatted to maintain 300 K. The fixed flCNT was pulled in the sliding direction by the sliding of the polymer layers, and a restraining force was applied to all atoms in the fixed flCNT, resulting in the fixed flCNT atoms collectively translating back and forth in the x-direction. No thermostat was applied to the remaining atoms in the sliding flCNT and polymer layers. Therefore, the temperature was permitted to evolve as the sliding excited atomic vibrations at the interfaces.

Quantitative validation with experimental CNT-polymer shear strength measurements does not appear to be readily available due to the "pull-along" (instead of pull-out) setup adopted here. In these simulations, the flCNTs were effectively infinite, due to the periodic boundary conditions, and were not extracted from the matrix. However, for a finite CNT experiencing a pull-out force, the shear-lag model [98] indicates that the maximum shear stress will occur at the embedded end. Moving away from the end, the shear stress diminishes. Such a stress distribution cannot be expected from the periodic version. Nevertheless, experimental interfacial shear stress results can be qualitatively compared with the simulations results presented here.

2.6 Transverse Strength

The third metric considered for this study is the transverse strength. Here, the flCNT/ polyimide models were deformed in tension along the z-axis, which is transverse to the flCNTs. Thus, these simulations predicted the mechanical response of the flCNT/polyimide interface normal to the flCNT surface. Although previous studies [59–61, 99, 100] used MD simulation to predict a similar behavior for CNT/polymer and epoxy/clay interfaces, the analogous response for flCNT/polymer interfaces has not been addressed. In this work, the simulation boxes comprised of polymerized models of fluorinated and non-fluorinated polyimides at equal mass fractions were deformed in the transverse direction (along the z-direction) to a strain of 150 % at a strain rate of $2{\times}10^{8}\ s^{-1}$ over 7.5 ns with 1 fs timestep. The temperature and pressure were 300 K and 1 atm, respectively. The stress-strain response along the z-direction for the systems were recorded over the whole strain range. For objective comparison of the two materials, only one model of both systems was chosen for these simulations (47 % mass fraction of the fluorinated polyimide and 46 % mass fraction of the non-fluorinated polyimide). The peak strength is defined as the maximum stress value achieved during the simulation. The toughness is measured as the area under the stress-strain curve and the stiffness is calculated as the ratio of stress and strain in linear portion of the curve.

2.7 Results

2.7.1 Interaction Energy

Figure 2.10 displays the flCNT/fluorinated and flCNT/non-fluorinated interaction energy as the number of polymer monomers is varied. It is important to emphasize that lower interaction energy values (higher negative values) correspond to more stable interfaces. It is also important to emphasize that the data points represent single simulations, not averages of multiple replicate simulations. Although it is common to simulate multiple replicates for smaller models (5000 atoms) to predict accurate properties with smaller standard deviation to optimize simulation time [80, 81, 101], the models described herein comprise 30,000-60,000 atoms, and are thus not expected to have significant variability between replicate simulations. The curves shown in **Figure 2.10** are best-fit polynomial functions. **Figures 2.11** and **2.12** show the equilibrated polymerized models for three mass fractions of the fluorinated and non-fluorinated polyimides, respectively. For the range of polyimide concentrations studied, the interaction initially increases and then becomes constant at a mass fraction around 40 %. The magnitude of the initial increase is significantly high for the fluorinated polyimide. At low mass fractions (about 23 %), the monomers did not disperse enough to completely separate the two flCNTs, as shown in **Figure 2.11**(a).

As a result, the interaction energy is significantly impaired at the low mass fractions, but quickly increases as the monomer dispersion becomes more even. This was not a significant issue with the non-fluorinated polyimide, as shown in **Figure 2.12**.

Figure 2.10 also shows that the interaction energy curves shift upwards after polymerization for both systems. This likely occurs because the process of polymerization causes segments of the monomers to pull away from their natural alignment with the flCNT surface. Aromatic groups on polymers have a tendency to align with aromatic surfaces [83, 102]. If segments of the monomers that are aligned with the flCNT surface are pulled out of alignment during polymerization, the interaction energy is expected to reduce (shift upwards).

It is also evident from **Figure 2.10** that the fluorinated polyimide shows poor interaction with the flCNT relative to non-fluorinated polyimide. This behavior is likely due to the presence of fluorine atoms in the $-CF_3$ groups on the monomer. The relatively large $-CF_3$ groups provide steric hindrance which prevents the fluorinated monomers from aligning flat with the flCNT surface. This effect is seen in other fluorinated polymers as well as in CNTs functionalized with fluorine atoms [103–105], whereas non-fluorinated monomer can easily align flat with the flCNTs, as described above. According to Grainger and Stewart [105], the lower interaction energy for fluorinated polyimide is due to the higher ionization potential and lower polarizability of fluorine atoms. **Figure 2.5** shows that the mass density peak of the polymerized

non-fluorinated polyimide system is closer to the flCNT surface relative to the fluorinated polyimide. **Figure 2.13** shows a comparison of the orientation of phenyl rings with respect to flCNT surface in both polyimide systems. The dotted vertical lines in **Figure 2.13** represent the polymer density peaks shown in **Figure 2.5**. Note that **Figure 2.1** shows that the fluorinated polyimide monomer has 6 phenyl rings as compared to 4 rings in the non-fluorinated monomer. The non-fluorinated polyimide still has more phenyl rings with orientation less than 30°relative to the fluorinated polyimide, thus reinforcing the tendency of the $-CF_3$ groups to disrupt the phenyl ring alignment.

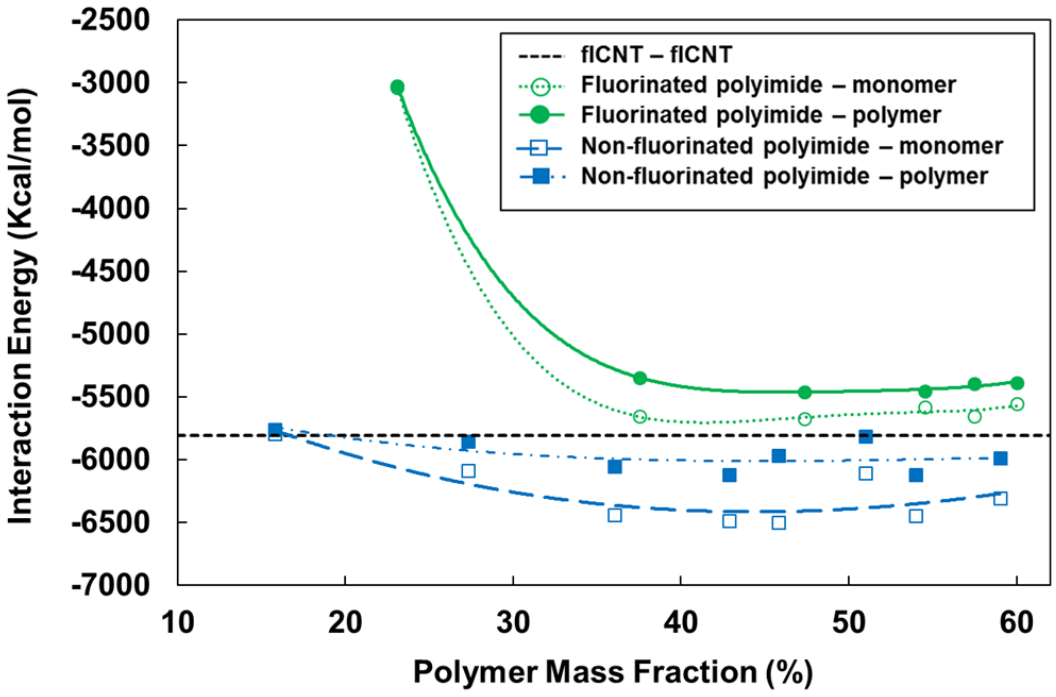

Figure 2.10: flCNT/polyimide interaction energy for varying levels of polymer mass fraction.

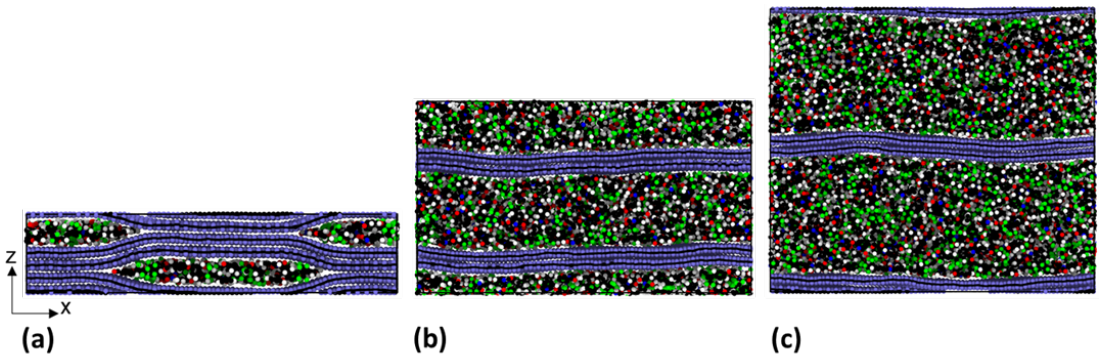

Figure 2.11: Molecular models of polymerized flCNT/Fluorinated polyimide polymer composite with mass fraction (a) 23 % (b) 47 % (c) 60 %.

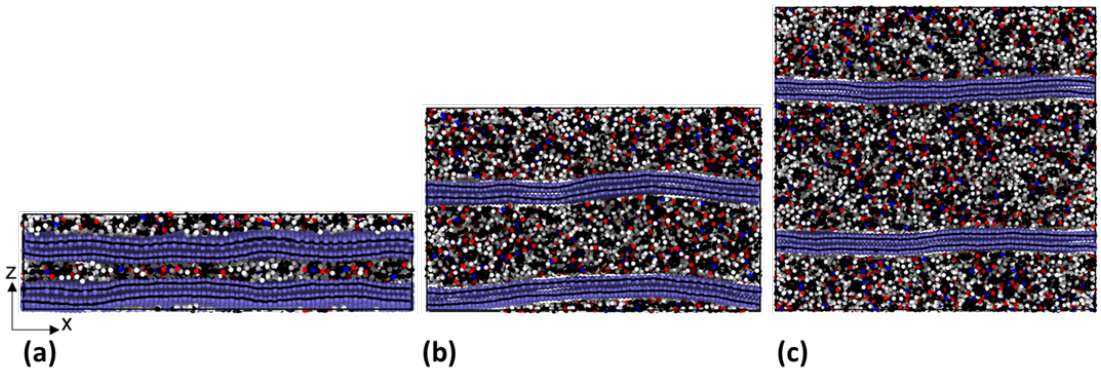

Figure 2.12: Molecular models of polymerized flCNT/Non-fluorinated polyimide composite with mass fraction (a) 16 % (b) 46 % (c) 59 %.

2.7.2 Friction

Figure 2.14 shows a representative plot of friction force vs displacement of a sliding flCNT for the fluorinated polyimide (47 % mass fraction) at a velocity of 100 m/s. The plot shows the initial static friction peak followed by steady kinetic sliding.

Figure 2.15 shows the friction results obtained from the sliding simulations. All the

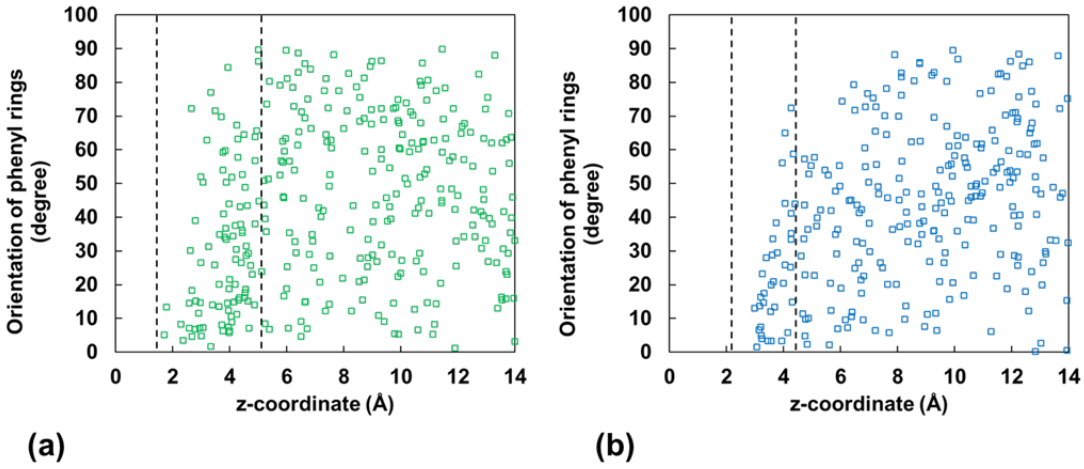

Figure 2.13: Orientation of phenyl rings in (a) fluorinated polyimide/flCNT with 47 % mass fraction and (b) non-fluorinated polyimide/flCNT composites with 46 % mass fraction.

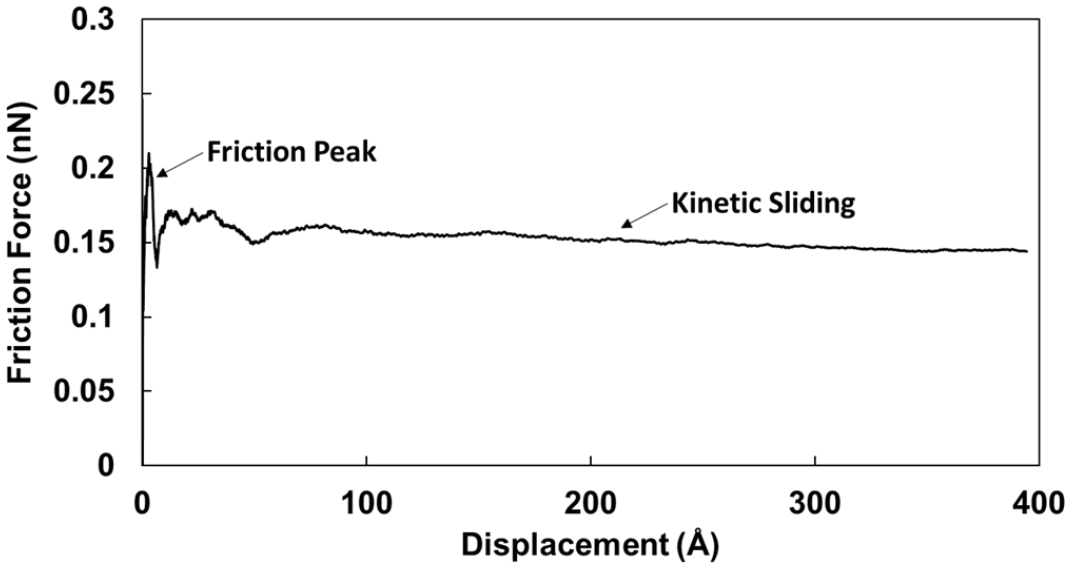

Figure 2.14: Plot of friction force vs displacement of a moving flCNT for fluorinated polyimide with 47 % mass fraction at 100 m/s sliding velocity.

data points are fitted with a power law curve and the y-axis is plotted on a logarithmic scale. A comparison is made between the sliding of flCNT against flCNT and the

sliding between flCNT and polyimide layers in monomeric and polymeric forms. Considering the bare flCNT friction, it is critical to consider the commensuration between surfaces. The friction between the two graphitic planes (commensurate and incommensurate) is computed similarly to that of between flCNT/polyimide as described in **Section 2.4**. Indeed, the commensurate case resulted in friction forces 2-3 orders of magnitude greater than the incommensurate case, depending on the sliding velocity. This is consistent with previous studies [40, 44, 52]. To expound on the importance of commensuration, consider **Figure 2.6** which demonstrates the non-bonded energy variation experienced by a single atom moving parallel to a flCNT-like sheet. In the case of an entire flCNT sliding against another, the notion must be broadened as all atoms in a layer will undergo the non-bonded energy variations (induced by the adjacent flCNT layer), moving in-and-out of potential energy wells. It is important to note the movement of an atom along the energy surface relative to the other atoms in the same layer. When the atoms enter and exit the energy wells in sync, there are significant net potential energy changes as the layers slide along one another [44]. This occurs when the layers are commensurate. When the flCNTs are incommensurate, at any given time some atoms will be in low potential energy locations and others in high energy positions, such that the net non-bonded potential energy is mostly unchanged as the one layer is shifted along the other [44]. The lack of energy corrugation in the incommensurate case results in extremely smooth sliding. Whereas, in the commensurate scenario, the coordinated virtual "interlocking" of atoms by their

non-bonded interactions and the breaking of such interlocking results in appreciable energy-dissipating vibrations and consequently higher friction.

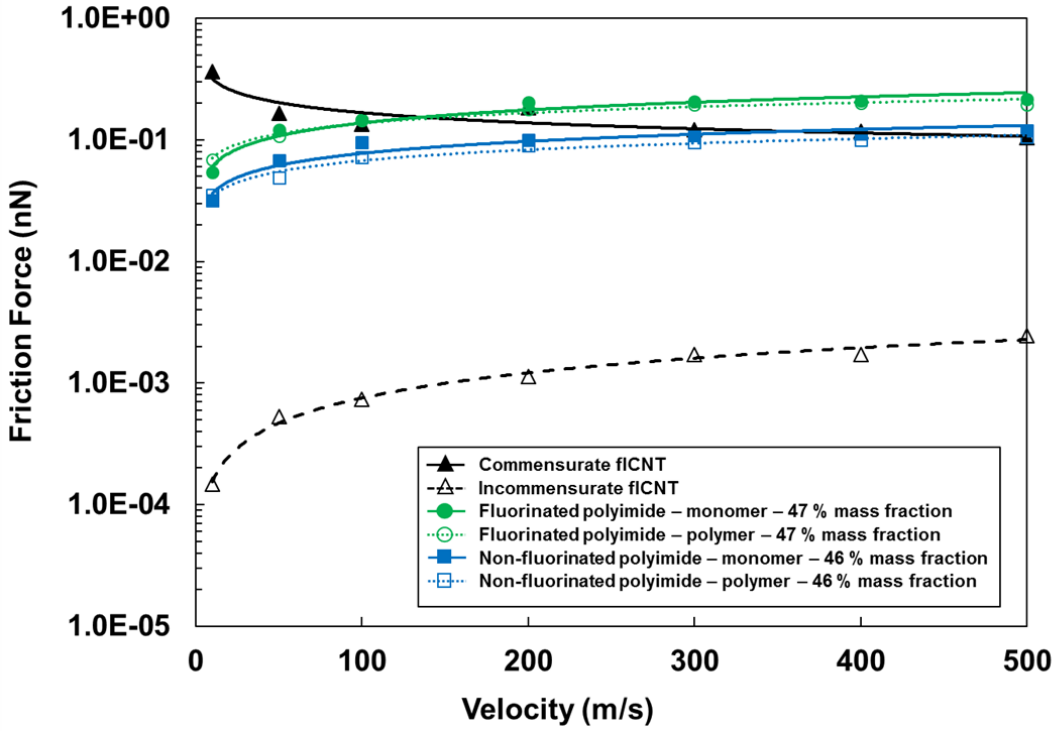

Figure 2.15: Comparison of bare flCNT friction and flCNT-polyimide friction for both fluorinated and Non-fluorinated polyimides. All friction forces are plotted for a range of sliding velocities. Two cases of flCNT-flCNT sliding are shown, namely, commensurate and incommensurate.

Figure 2.15 also reveals other interesting trends. The incommensurate flCNT/flCNT case and all flCNT/fluorinated and flCNT/non-fluorinated polyimide models demonstrate generally increasing friction with increasing sliding velocity, which is predicted by the Prandtl-Tomlinson model and various modifications thereof [106–109]. The commensurate flCNT/flCNT model shows mainly decreasing friction with increasing sliding velocity over the range of velocities modeled. The steady friction decrease

can be compared to Xu et al.[44], where decreasing friction between commensurate flCNTs was shown for sliding velocities above 100 m/s. They also observed that the flCNT/flCNT friction first increased with increasing velocity for low sliding velocities and then peaked at about 100 m/s before declining. However, in this work, only the decreasing friction regime is observed. Presumably the peak friction occurs for velocities at or below 10 m/s. By including a Langevin force to the Prandtl-Tomlinson model to account for thermal effects, Nakamura et al. [1] showed declining friction at high sliding velocities, which was identified to occur from a double-slip event. In their model, as the velocity increases, the friction force also increases but can drop down when a critical velocity is reached, comparable to the trends observed by Xu et al. [44].

Further comparison with Xu et al. [44] reveals that the friction forces observed in that study (on the order of 0.1 nN/nm^2) are greater than the PCFF-IFF models (on the order of 0.001 nN/nm^2). The discrepancy is mainly attributed to the difference in force field. Recall that **Figure 2.7** shows that the Lennard-Jones non-bonded potential used in this study does not capture the full magnitude of the corrugation between sp_2 carbon surfaces, whereas Xu et al. [44] used Kolmogorov and Crespi's potential, which was specially designed to accurately reproduce the registry effect in pure carbon materials. Another factor in the discrepancy between Xu et al. [44] and this study is the direction of sliding. In the present study, the flCNTs were pulled in the zig-zag direction; however, Xu et al. [44] opted to slide flCNTs along the

armchair direction. The energy barrier in the armchair direction has been computed to be about double that of the zigzag direction [44]. The energy barrier discrepancy could be about 7 $meV/atom$ due to the choice in the sliding direction and about 10 $meV/atom$ due to differences in force fields, as seen in **Figure 2.7**. It can be concluded that such a difference has a substantial impact on the friction force.

The primary significance of **Figure 2.15** is the comparison between the friction with and without polyimides. The incommensurate friction case is taken to most accurately represent commensuration between flCNTs in a stack, because CNT chiralities will most likely vary between adjacent flCNTs [110]. In comparison to incommensurate flCNT/flCNT friction, the presence of polyimides results in an increase of two orders of magnitude in the friction force. These results can be qualitatively compared with experimental pullout studies and interfacial shear strength calculations. The friction force between sp_2 carbon layers has been experimentally measured, for example, by telescoping multi-walled CNTs (MWCNTs) [56, 111, 112]. Cumings and Zettl [111] determined the static and dynamic interfacial shear strength (pullout force per unit area) between the nested layers of MWCNTs to be 0.66 and 0.43 MPa, respectively. For two MWCNT samples, Yu et al. [56] computed the interfacial shear strength to be 0.30 and 0.08 MPa. The authors attributed the difference in shear strengths to different degrees of commensuration between sliding layers. The CNT interlayer shear strength can be contrasted with the CNT-epoxy shear strength, which can be experimentally measured by attaching a CNT to an atomic force microscopy tip and

extracting the CNT from a polymer matrix. Cooper et al. [39] obtained CNT-epoxy shear strengths for different samples in the range of 35-376 MPa. This is roughly 2-3 orders of magnitude greater than the interfacial shear strengths reported between nested CNT layers, which is in agreement with our study.

Figure 2.15 also reveals that the friction force is higher with the fluorinated polyimide than with the non-fluorinated polyimide for equal mass fractions. This is likely because the fluorine atoms in the fluorinated system offer steric hindrance and interlocking, leading to nanoscale surface roughness which prevents its sliding against the flCNT surface as observed in the literature [103–105]. The non-fluorinated polyimide, which shows good alignment with flCNT surface, as discussed above, offers little resistance to sliding, thus lowering the friction force. In addition, **Figure 2.15** shows no significant improvement in friction force in both polyimides between their monomeric and polymeric forms.

Figure 2.16 shows the magnitude of the friction force for a range of mass fractions of polymerized fluorinated and non-fluorinated polyimides. The data is fitted using power law curves. The non-fluorinated polyimide data demonstrates friction force increases with increasing velocity, and there is no significant difference in the friction force for three mass factions (16 %, 46 %, and 59 %). The fluorinated polyimide models at mass fractions of 23 %, 47 % and 60 % show the same friction force trends as seen with the non-fluorinated polyimide.

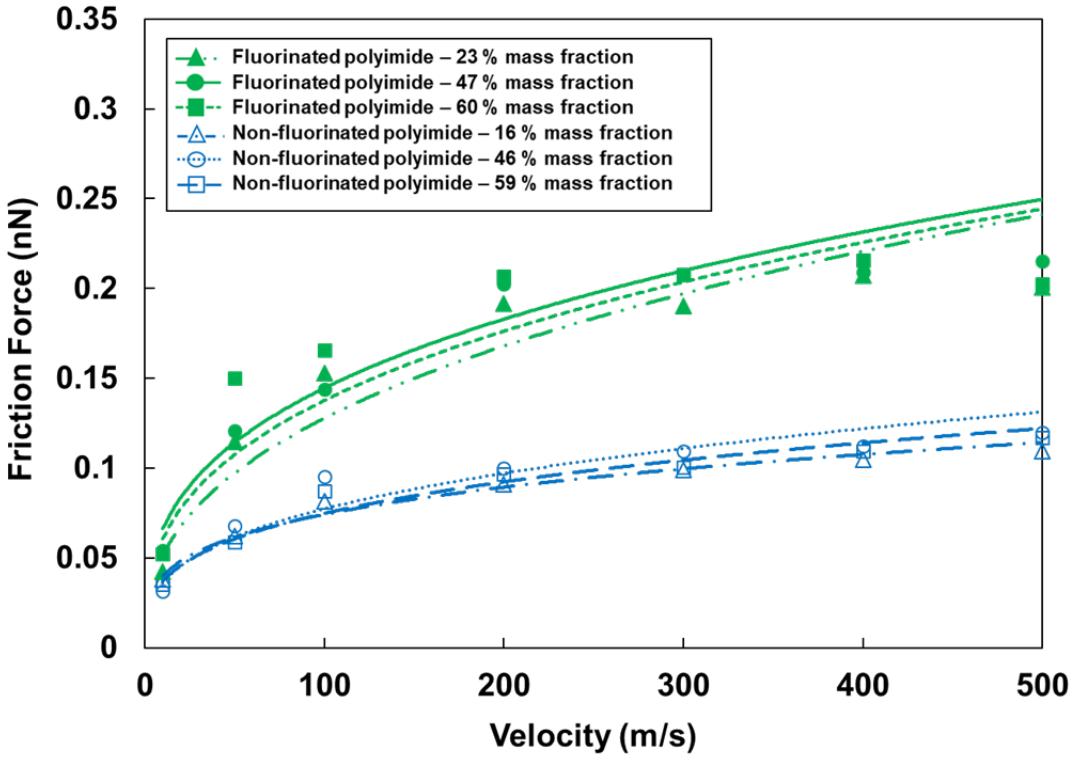

Figure 2.16: Comparison of friction force versus velocity between polymerized fluorinated and non-fluorinated polyimides for varying mass fractions.

Figure 2.17 shows the effect of the mass fraction of the polyimide systems on the friction force at a velocity of 10 m/s. The data points are fitted with linear functions. The results show that the friction force does not significantly change with varying mass fraction, as it more strongly depends on the surface roughness between the flCNT/polyimide interface, as described above for the fluorinated and non-fluorinated polyimides. **Figures 2.15** to **2.17** are replotted in terms of shear stress (friction force divided by contact area between flCNT and polyimides) and are included as **Figures A.4** to **A.6** in the supplementary information (**Appendix A.4**).

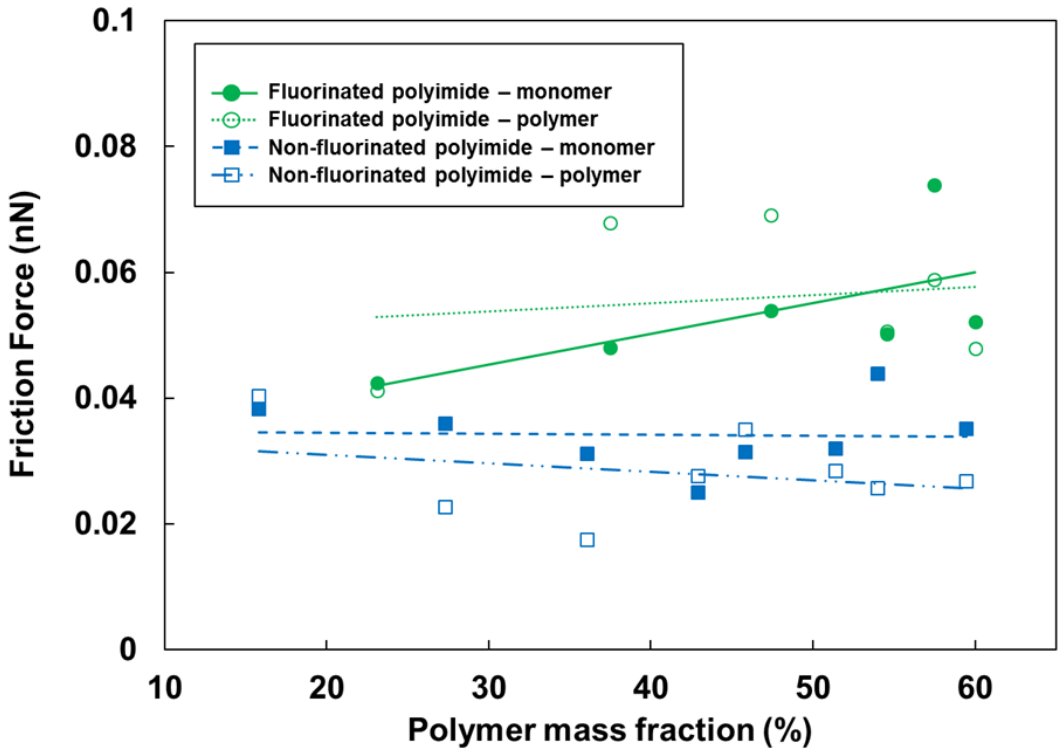

Figure 2.17: Effect of varying mass fraction on flCNT-polyimide friction force for both fluorinated and non-fluorinated polyimides. Friction simulations were performed with a sliding velocity of 10 m/s.

2.7.3 Transverse Tension

Figure 2.18 shows the results of the transverse strength simulations for both flCNT/polyimide systems. **Table 2.2** provides the peak strength, stiffness, and toughness values as defined in **Section 2.4**. The fluorinated polyimide exhibits a higher peak strength and toughness, thus offering higher resistance to delamination than the non-fluorinated system. This is likely because of the interlocking of fluorine atoms on the flCNT surface, as described above. The stiffness in transverse tension is almost the

same for both systems. Snapshots of the fluorinated system in **Figures 2.19** and **2.20** show that as the strain increases the polyimide chains stretch and eventually separate from each other before separating from the flCNT surface, indicating that the flCNT/polyimide interaction is initially stronger than interaction of the polymer chains. Awasthi et al. [59] observed a similar result with polyethylene-graphene interface pull-out simulations.

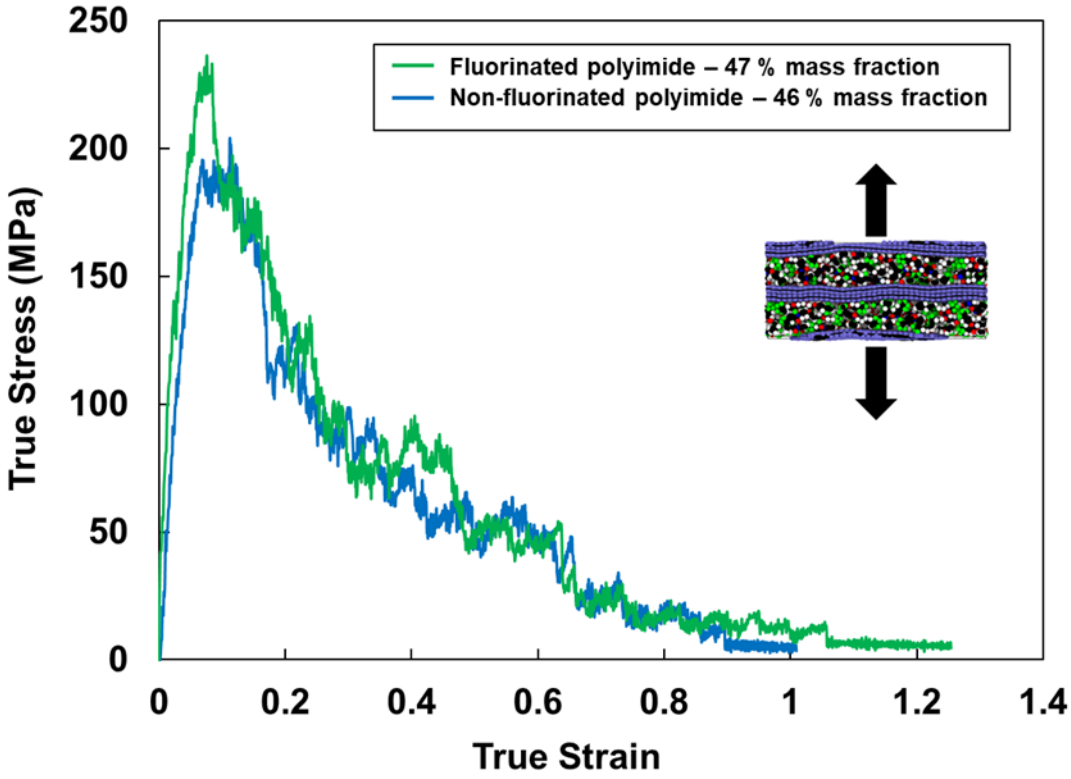

Figure 2.18: Stress-strain plot for transverse strength simulations for both polymerized fluorinated and non-fluorinated polyimides.

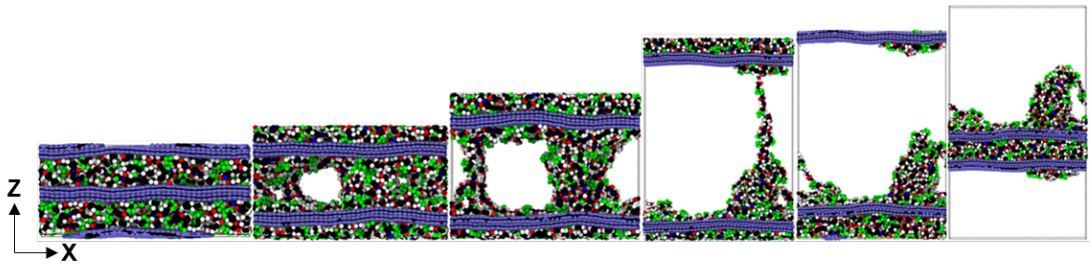

Figure 2.19: Snapshots of the fluorinated polyimide undergoing transverse deformation.

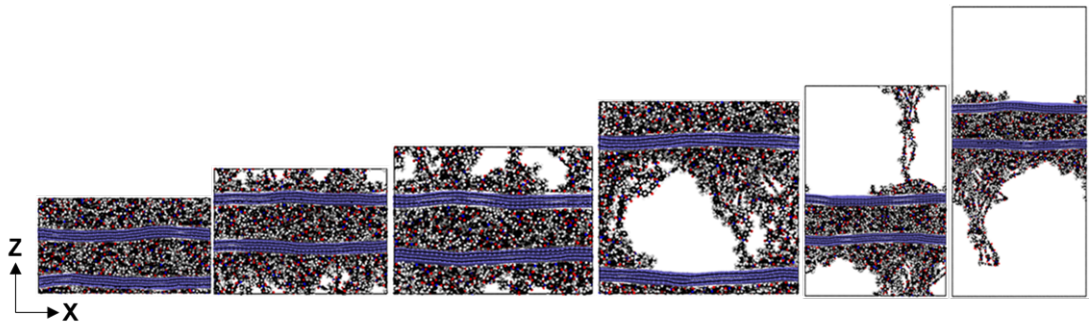

Figure 2.20: Snapshots of the non-fluorinated polyimide undergoing transverse deformation.

Table 2.2
Transverse strength results for fluorinated and non-fluorinated polyimide.

Polymer	**Stiffness** (GPa)	**Toughness** (MJ/m^3)	**Peak Strength** (MPa)
Fluorinated polyimide	3.56	73.94	236.57
Non-fluorinated polyimide	3.70	65.10	204.07

2.7.4 Polyurea

Along with polyimides, this work also describes the modeling of polyurea to predict the interaction energy, friction force and transverse strength of polyurea/flCNT

composite. The simulation settings and result analysis methods implemented here are similar to as described in **Sections 2.4, 2.5, 2.6, 2.7**. **Figure 2.21** shows the molecular structure of polyurea.

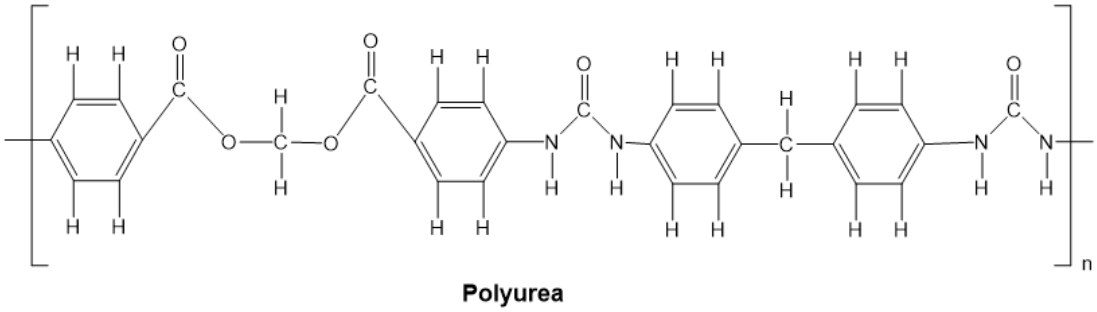

Figure 2.21: Skeletal structure of polyurea.

Figure 2.22 shows the interaction energy for both polyimides and polyurea for varying mass fraction before and after polymerization. as expected, the monomer polyurea has the highest interaction energy and remains unchanged with varying mass fraction. This is likely because of its ability to align flat with the flCNT surface due to π-π interaction between the phenyl rings in flCNT and polyurea as well as cation-π interaction between phynyl rings in flCNT and nitrogen atoms in polyurea molecules. After polymerization, the interaction energy reduces because of the newly formed covalent bonds between the monomers that restricts their motion and alignment as shown in **Figure 2.23**. Similar trend was observed with PEEK [113] as the PEEK and polyurea molecules has similar atom types and some degree of similar molecular structure. **Table 2.3** presents the Interaction energy and friction force of flCNT/polyurea composite for varying mass fraction. The friction force analysis was not

performed for polymerized models as modeling of polyurea was conducted to qualitatively verify interaction energy results for other polymers [79, 113, 114] by comparing their alignment at flCNT/polymer interface.

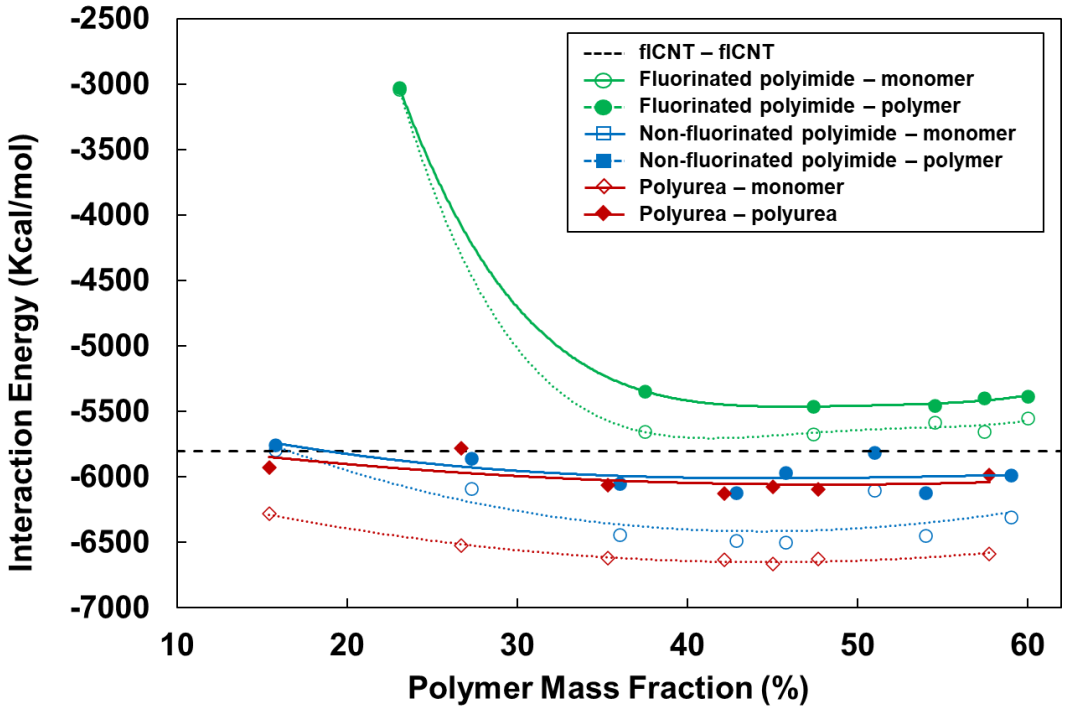

Figure 2.22: flCNT/polymer interaction energy for varying levels of polymer mass fraction.

Figures 2.24 and **2.25** confirm the observations from **Figure 2.22**. More number of phenyl rings in polyurea have an alignment of less than 30°at the interface of flCNT/polymer as compared to fluorinated polyimide. **Figure 2.24**a shows that the interface of flCNT/fluorinated polyimide has more fluorine atoms (green colored) that prevents its alignment as compared to lesser nitrogen atoms (blue colored) in flCNT/polyurea composite in **Figure 2.24**b.

Table 2.3
Interaction energy and friction force of flCNT/polyurea composite for varying mass fraction .

Mass fraction (%)	Interaction Energy ($Kcal/mol$)		Friction Force (nN/nm^2)
	Monomer	Polymer	Monomer
15	-6280	-5926	0.0003510077
27	-6526	-5778	0.0002854647
35	-6622	-6060	0.0002804045
42	-6636	-6128	0.0002149645
45	-6664	-6074	0.0002079665
48	-6624	-6097	0.0002847730
58	-6588	-5985	0.0002356513

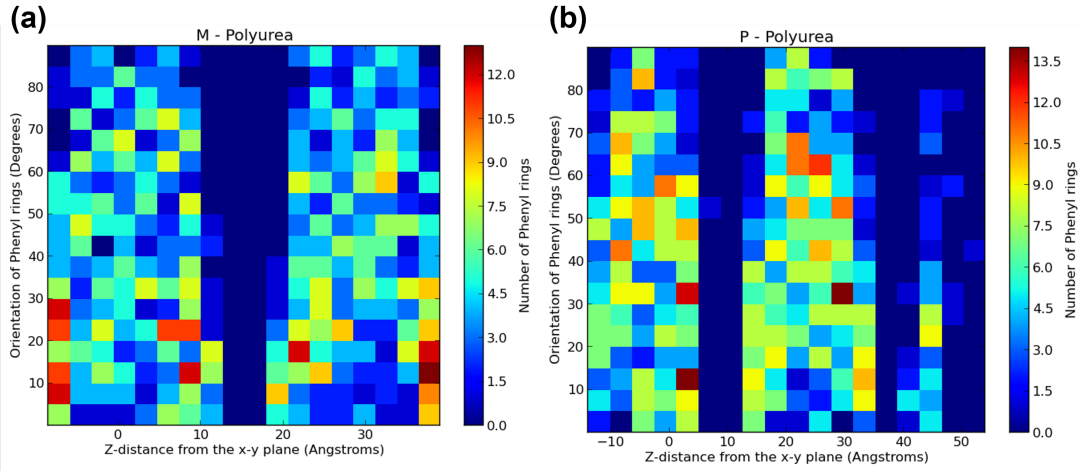

Figure 2.23: Orientation of phenyl rings in polyurea/flCNT composite 45 % mass fraction composite in (a) monomer and (b) polymer form.

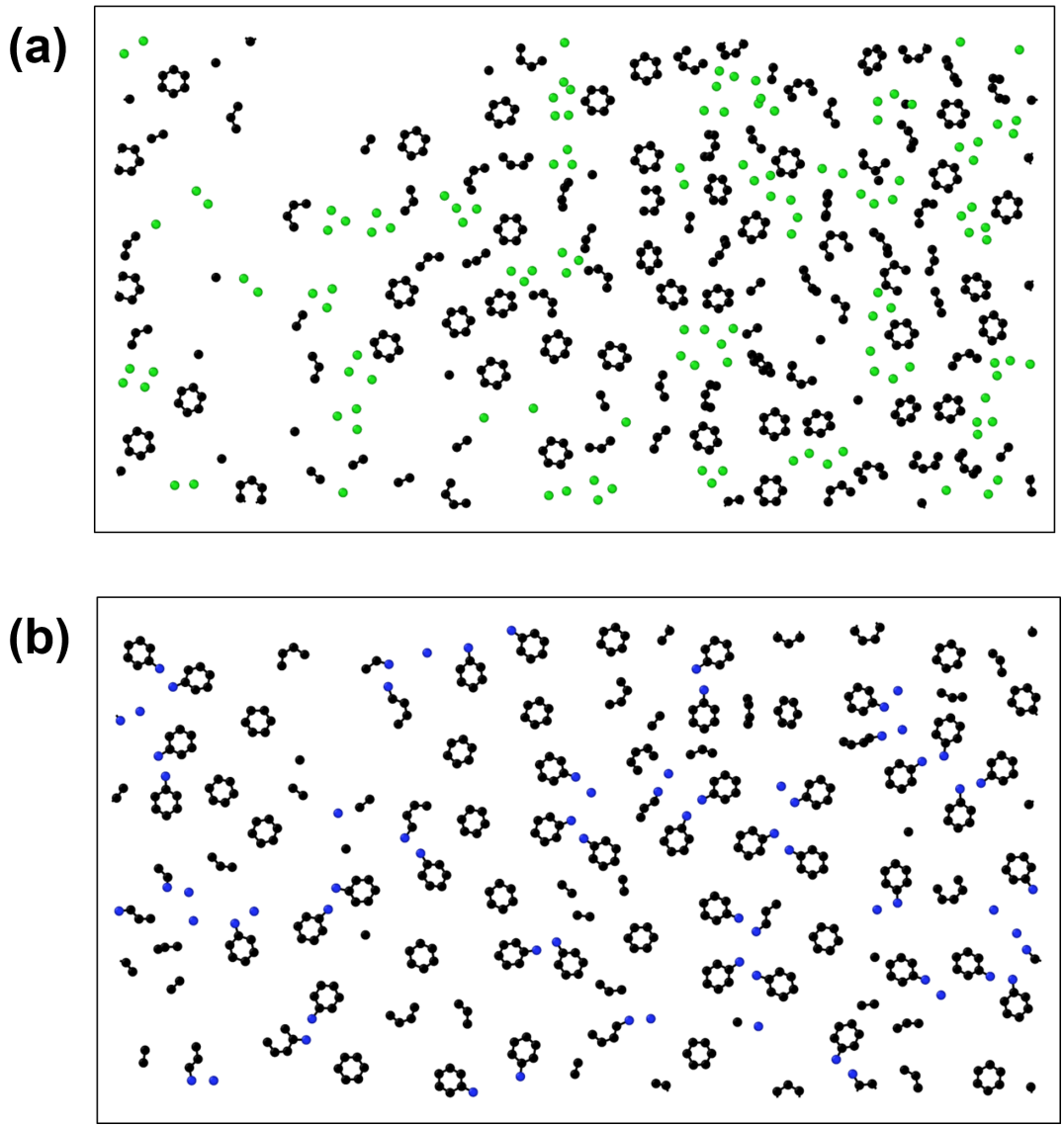

Figure 2.24: Snapshots of polymer surface at the interface of flCNT-polymer for (a) fluorinated polyimide with 47 % mass fraction and (b) polyurea with 45 % mass fraction composites. Both polymers are in monomeric form.

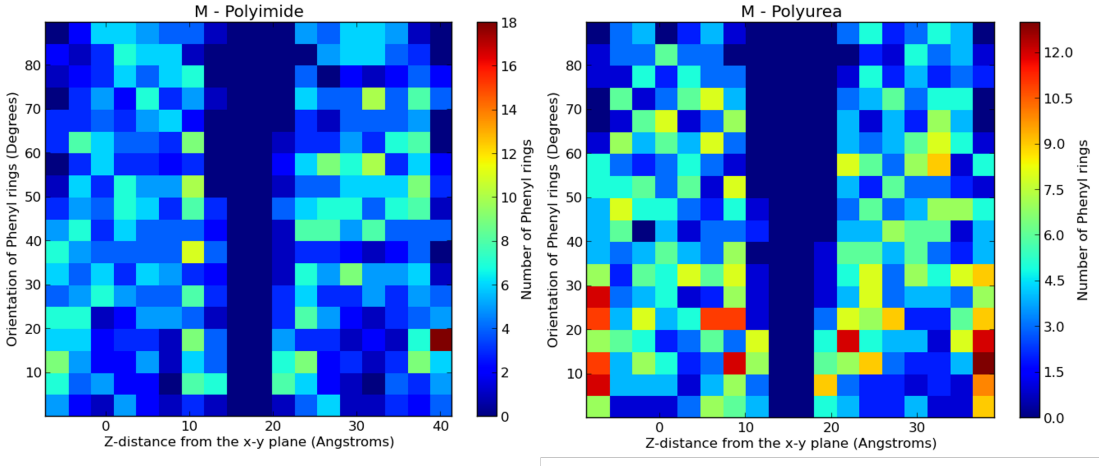

Figure 2.25: Orientation of phenyl rings in fluorinated polyimide/flCNT with 47 % mass fraction (left side), and polyurea/flCNT with 45 % mass fraction composites (right side). Both polymers are in monomeric form.

2.8 Conclusions

Original flCNT/polyimide MD models were developed to study the effect of infiltrating fluorinated and non-fluorinated polyimides within flCNT stacks. The fluorinated and non-fluorinated polyimide systems were compared based on three criteria: interfacial energy, friction force, and transverse strength at the flCNT/polyimide interface. The fluorinated polyimide exhibited a lower interaction energy but higher friction force relative to the non-fluorinated polyimide. In transverse tension, the fluorinated polyimide demonstrated a higher peak adhesive strength. These behaviors are mostly a result of the increased steric hindrance associated with the fluorine groups in the fluorinated polyimide. While reduced flexibility of the fluorinated polyimide reduces the chemical interaction and thus interaction energy at the interface, it provides mechanical interlocking which improves the frictional resistance and adhesion at the flCNT/polyimide interface.

It was also determined that the presence of polyimide dramatically enhanced the friction force over that of bare incommensurate flCNTs. This enhancement was observed for both flCNT/polyimide systems. The results suggest that when the polyimide is successfully infiltrated, regardless of the concentration or level of polymerization, it should improve the friction of the interfaces within the material.

In the design of flCNT-based nanocomposites, careful consideration is needed in selecting a high-performance polymer system to yield the desired properties. The molecular insights gained in this research can help guide the selection of polymer matrices for structural composites used in future human missions to Mars.

Chapter 3

Validation of Reactive Interface Force Field for Thermo-Mechanical Property Prediction of Epoxies

3.1 Introduction

Epoxy-based composite materials are the primary structural material used in most modern commercial and military aircraft. Their high specific strength and specific modulus make them ideal for this purpose. There is strong interest in developing higher-performing fiber/epoxy composites for improved durability for future aircraft

and for reduced weight for crewed deep-space vehicles. Predictive computational modeling can be used to greatly facilitate the development of new epoxy resins and epoxy composites.

Molecular Dynamics (MD) simulation is a powerful tool for predicting the effect of molecular structure on thermo-mechanical properties of epoxy resins. A key component of MD simulation is the selection of an appropriate force field to describe the interaction between the atoms in an MD model. Force fields contain a series of energy terms associated with different degrees of freedom in a discrete molecular system, including the bonded terms (bonds, angles, dihedrals) and non-bonded terms (electrostatic interactions, van der Waals interactions, hydrogen bonding). Over the years, force fields have evolved greatly. The Class I force fields, such as CHARMM [115], AMBER [116], DREDING [117], and OPLS [118], contain simple bonded terms that are typically harmonic and uncoupled. Class II force fields, such as COMPASS [77], MM2 [119], CFF [120], and MMFF [121]; are computationally more expensive, but include higher-order bonded energy terms and additional bonded cross-interaction terms (e.g. bond-angle, bond-dihedral, angle-dihedral) for improved accuracy.

Reactive force fields are particularly useful for simulating systems that undergo large mechanical deformations and/or have chemical reactions. Perhaps the most well-known reactive force field is ReaxFF [122]. ReaxFF is well-proven to predict chemical reactivities and material properties under a wide range of conditions for various

chemical species. However, the powerful strengths of ReaxFF come at a cost. MD simulations using ReaxFF are computationally demanding and separate parameter sets must be established to simulate specific conditions and sets of elements. That is, there is not a single ReaxFF parameter set that can be used as a workhorse for a wide range of material systems. For polymers, this is a particular problem because engineering resins contain a wide range of atom types (C, H, O, N, S, F, Si, etc.). Currently, there is no single ReaxFF parameter set that can be generally used for all polymer systems, although the Liu et al parameter set [123] has been shown to work well for predicting the mechanical response of epoxies [80, 81], epoxy-based composites [83, 124], and PEEK [101]; and the parameter set of Damirchi et al. [66] has been shown to simulate epoxy/CNT interaction accurately.

The Interface Force Field (IFF) [12] is a unique force field that is built on various Class I and Class II force fields (such as the PCFF force field [125]) to accurately simulate a wide range of materials and material interfaces [126–130]. It allows the simulation of various materials types, such as metals, ceramics, polymers, and biomacromolecules at the same time, and in higher accuracy than available before. Broad applicability and higher accuracy are related to order-of-magnitude improved representations of chemical bonding, interpretability of all parameters, and systematic validation of structures and energies. Recently, a modified version of IFF has been developed to allow the simulation of bond dissociation [13]. This so-called Reactive Interface Force Field (IFF-R) uses Morse potentials to describe covalent bond interactions instead

of traditional fixed-bond harmonic potentials. Thus, IFF-R can effectively simulate covalent bond disassociation associated with large mechanical deformations. IFF-R has been proven to work well for predicting physical and mechanical properties of carbon nanotubes and crystalline polyacrylonitrile, cellulose, and FCC iron [13]. However, it has not yet been explored for high-performance thermosetting resins with an amorphous molecular structure.

The objective of this paper is to demonstrate the consistency of IFF-R for three resins with different sets of epoxide and amine monomers. Predicted thermo-mechanical properties using IFF-R are compared to the corresponding experimental values. Using simple strain rate scaling for mechanical properties, it is shown that IFF-R predicts mass density, elastic properties, yield strength, glass transition temperature, and thermal expansivity that are consistent with experiments. In this paper, the modelled materials are described first, followed by an explanation of the MD modeling protocols. The experimental methods are described next, and a comparison of the predictions and measurements follows.

3.2 Materials

3.2.1 Material System and Force Field

Two epoxy polymer systems were considered in this study. These two systems are described below, as indicated by

1. EPON 862/EPIKURE W: Diglycidyl ether bisphenol F (DGEBF) with a diethyltoluenediamine (DETDA) curing agent
2. EPON 828/OMICURE 33-DDS: DGEBA with a 3,3' diaminodiphenyl sulfone (33DDS) curing agent

The molecular structures of the EPON 862/EPIKURE W (henceforth referred to as EPON 862/DETDA), and EPON 828/OMICURE 33-DDS (henceforth referred to as EPON 828/DDS) systems are shown in **Figures 3.1** and **3.2**, respectively. These systems were chosen because they are both highly benchmarked.

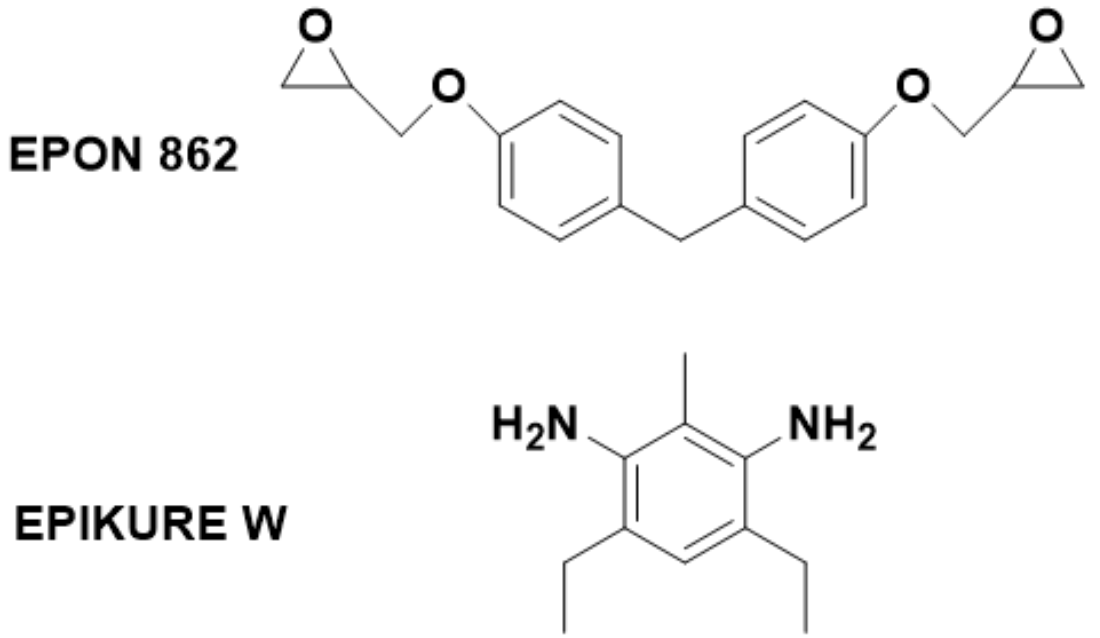

Figure 3.1: EPON 862/DETDA molecular structure.

3.3 MD Simulation Settings

The LAMMPS (Large-scale Atomic/Molecular Massively Parallel Simulator) software package was used for all MD simulations described herein [3], utilizing the IFF-R force field. The virtual π orbitals that have been used previously with IFF [79] were not used in the current study because no aromatic reinforcement surfaces were simulated (e.g. graphene or carbon nanotubes). The Lennard-Jones diameters were chosen per guidelines described by Heinz et al. [12]. Nose-Hoover algorithms were used for both the thermostats and barostats for all of the simulations discussed herein [84–86]. The MD modeling algorithm consisted of three stages: model building, crosslinking, and

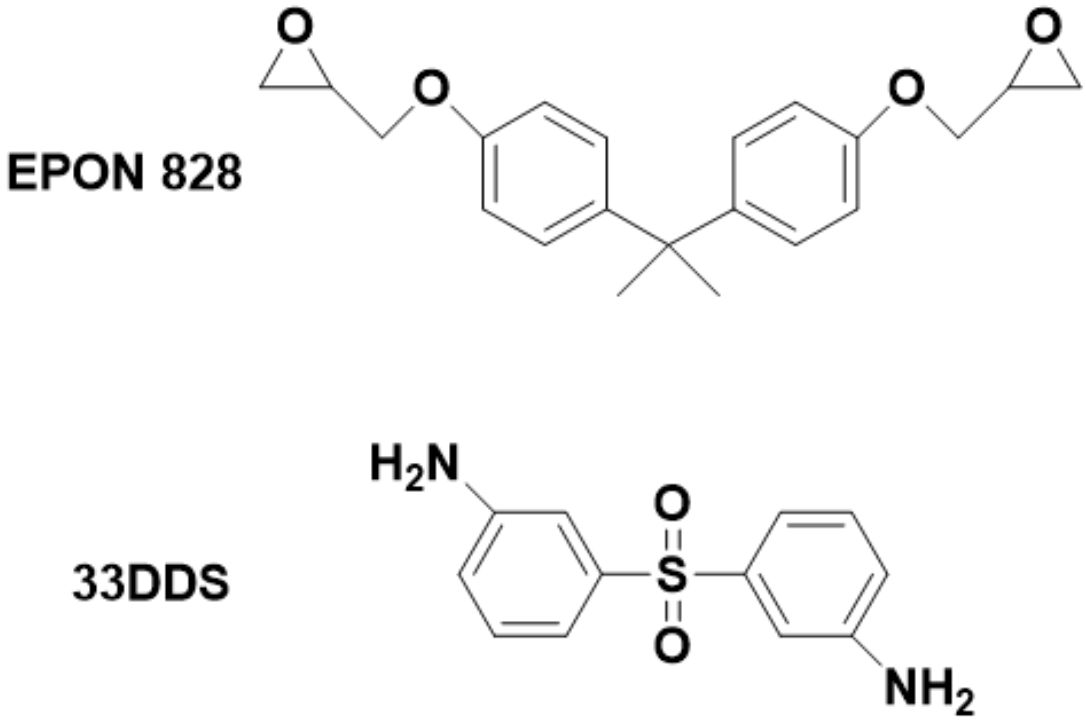

Figure 3.2: EPON 828/DDS molecular structure.

property prediction.

In the first stage, the MD models were assembled, densified, annealed, and equilibrated to their equilibrium densities at room temperature. The models were initially built with the monomers in a low-density mixture, which was gradually compressed to a target mass density at room temperature. After reaching the target density, the models were annealed in the NVT (controlled volume and temperature) ensemble by ramping up to an elevated temperature immediately followed by a ramp down to room temperature. The annealing process was followed by an equilibration at room temperature in the NPT (constant pressure and temperature) ensemble. **Table 3.1**

shows the simulation parameters for all three epoxy systems. Replicates of both systems were built for statistical sampling purposes, which is also listed in **Table 3.1**. Unless noted otherwise, the pressures for all NPT simulations were all set to 1 atm.

Table 3.1
MD simulation parameters for model building, densification, annealing, and equilibration.

Simulation parameter	**EPON 862/DETDA**	**EPON 828/DDS**
Epoxy/crosslinker monomers	90/45	170/85
Total number of atoms	5,265	10,795
Target mass density	1.17 g/cc	1.17 g/cc
Replicates	5	5
Densification temperature	300 K	300 K
Densification simulation time (time steps)	8 ns (1 fs)	4 ns (0.1 fs)
Annealing temperature	500 K	500 K
Annealing ramp rate	20 K/ns	20 K/ns
Equilibration temperature	300 K	300 K
Equilibration time (time steps)	1 ns (1 fs)	2 ns (1 fs)

In the second stage, the models were crosslinked using the `fix bond/react` command [91] in LAMMPS to the maximum crosslink density possible, where the crosslink density is defined as the ratio of the total number of covalent bonds actually formed to the total number of covalent bonds that could potentially be formed. As discussed previously [12], it is unrealistic to achieve crosslink densities of 100 % for epoxies. The simulation conditions used for the crosslinking process for each epoxy system are provided in **Table 3.2**. For both systems, an NPT simulation was used to obtain the equilibrated mass density after crosslinking. The parameters for this equilibration

are provided in **Table 3.2**.

Table 3.2
MD simulation parameters for model crosslinking and final equilibration.

Simulation parameter	**EPON 862/DETDA**	**EPON 828/DDS**
Crosslinking simulation time (time steps)	6 ns (0.1 fs)	3 ns (0.1 fs)
Crosslinking simulation temperature	450 K	800 K
Average crosslink density	92 %	93 %
Equilibration simulation time (time steps)	1 ns (1 fs)	1 ns (1 fs)
Equilibration temperature	300 K	300 K

In the third stage of MD simulation, the crosslinked systems were subjected to mechanical and thermal loads to predict Young's modulus, yield strength, glass transition temperature (T_{g}), and the coefficient of linear thermal expansion (CTE). For the thermal properties, each MD model was subjected to steady heating to an elevated temperature and subsequent cooling to room temperature. The NPT ensemble was used to observe the density and volume over the entire temperature range. The density-temperature relationship was fitted with a bilinear regression model using the "segmented" package in R [131]. From an initial estimate, the optimal breakpoint was calculated, which was taken to be the T_{g}, as shown with a representative case in **Figure 3.3**. Additionally, the volume-temperature ($V - T$) plot was fit with a cubic polynomial regression model above and below T_{g} to obtain the CTE at constant pressure, as given by

$$\alpha = \frac{1}{3V}\left(\frac{dV}{dT}\right)_p \tag{3.1}$$

Figure 3.3 also shows a representative volume-temperature graph as well as the slope of the $V - T$ curves above and below T_g. The MD parameters associated with the thermal property calculations for each polymer system are given in **Table 3.3** .

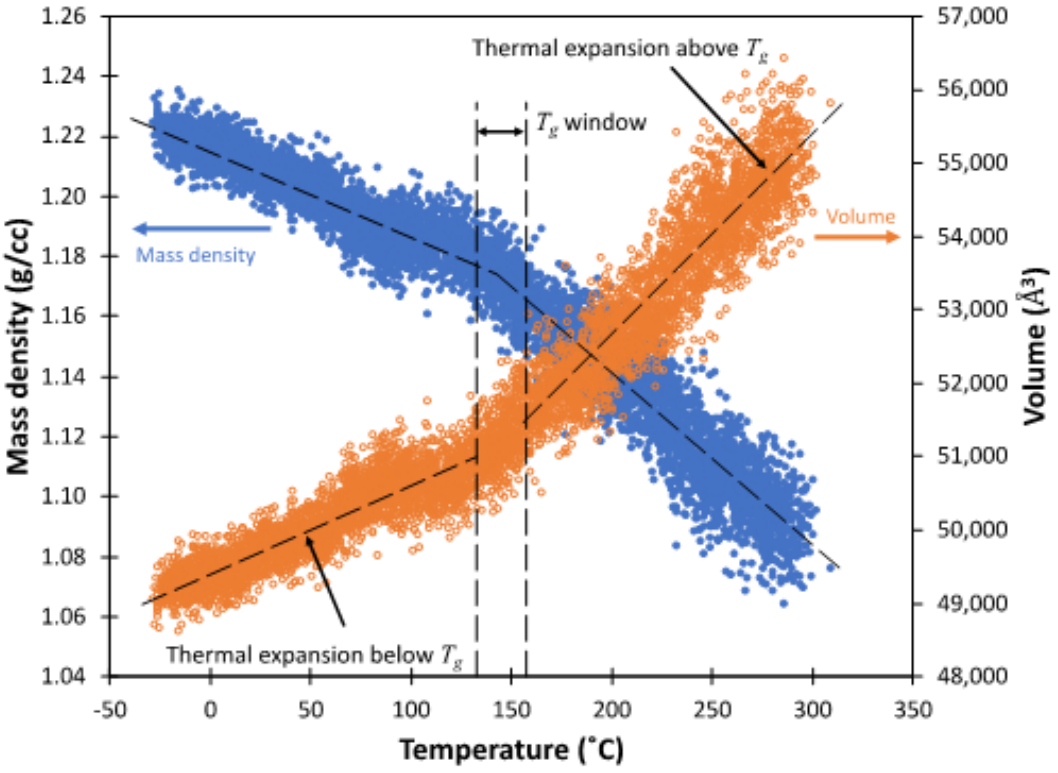

Figure 3.3: Density and Volume of a representative EPON 862/DETDA MD model as a function of temperature.

To determine the bulk modulus (K), the MD models were subjected to an elevated pressure (5000 atm) at room temperature (NPT ensemble), and the corresponding

Table 3.3
MD simulation parameters for thermal and mechanical property calculations.

Simulation parameter	EPON 862/DETDA	EPON 828/DDS
Temperature range	250 – 600 K	250 – 600 K
Heating rate	50 K/ns	50 K/ns
Cooling rate	50 K/ns	50 K/ns
Shear deformation	10 %	10 %
Shear deformation strain rate (time steps)	2×10^{7} s^{-1} (1 fs) 2×10^{8} s^{-1} (1 fs) 2×10^{9} s^{-1} (1 fs)	2×10^{7} s^{-1} (1 fs) 2×10^{8} s^{-1} (1 fs) 2×10^{9} s^{-1} (1 fs)

equilibrium volume was compared to that from the ambient pressure (1 atm) at room temperature. The bulk modulus was subsequently calculated as described in detail elsewhere [132]. To determine the shear moduli (G), shearing deformations were performed in the yz, xy, xz planes [83] at 300 K and three different strain rates (for the EPON 862/DETDA and EPON 828/DDS systems) using the simulation parameters provided in **Table 3.3**. **Figure 3.4** shows a representative shear stress-shear strain curve for the EPON 862/DETDA system at a strain rate of 2×10^{8} s^{-1}. For the stress-strain curve associated with each replicate, shearing plane, and strain rate, the bilinear breakpoint was determined by observing the strain at which the slope changed significantly. The shear modulus was calculated as the slope of the line before the breakpoint. The Young's moduli (K) and Poisson's ratios (ν) for each model were determined from the corresponding values of bulk modulus and the average shear modulus using standard isotopic elasticity equations [133]:

$$E = \frac{9KG}{3K+G} \tag{3.2}$$

$$\nu = \frac{3K-E}{6K} \tag{3.3}$$

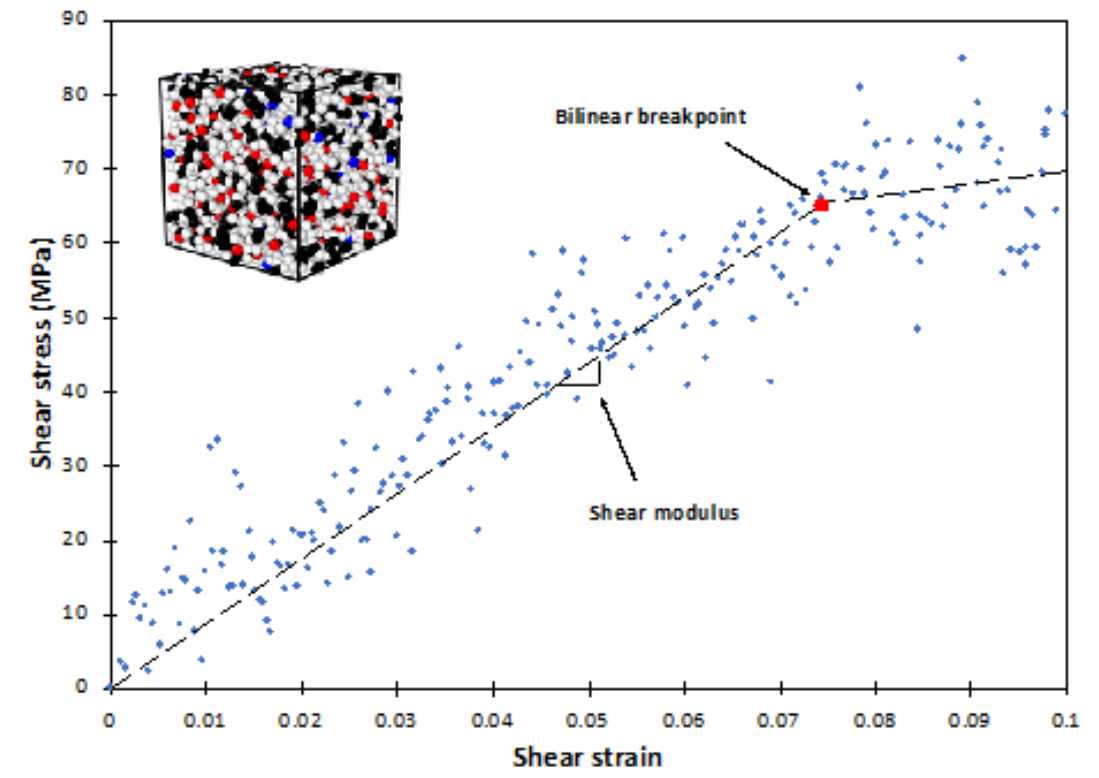

Figure 3.4: Representative shear stress/strain curve for EPON 862/DETDA.

For the uniaxial yield strength, the von Mises stress was determined from the individual stress components during the shear deformations:

$$\sigma_{\mathrm{vM}} = \frac{1}{2}\sqrt{\left[(\sigma_x-\sigma_y)^2+(\sigma_y-\sigma_z)^2+(\sigma_z-\sigma_x)^2+6\left(\tau_{xy}^2+\tau_{xz}^2+\tau_{yz}^2\right)\right]} \qquad (3.4)$$

The corresponding yield strength was the von Mises stress at the same breakpoints determined for the shear modulus, described above. Thus, the yield strength was determined for each replicate, shearing plane, and strain rate. **Figure 3.5** shows a representative von Mises/shear strain curve for the EPON 862/DETDA system at a strain rate of $2\times10^8\ s^{-1}$, with the breakpoint and yield strength value shown. The overall procedure for comparing the computationally-derived bilinear breakpoint with the laboratory length-scale yield stress is consistent with previous work [80]. It has been previously shown that for polymers at this length scale, observed yield is typically characterized by chain segment configurational changes [134–136], which is classically described by the Argon theory [137, 138].

3.4 Cooling rate effect on Glass Transition Temperature

It is important to note that no cooling rate correction factors were used for the T_{g} predictions performed herein, as have been employed previously [139–141] for MD

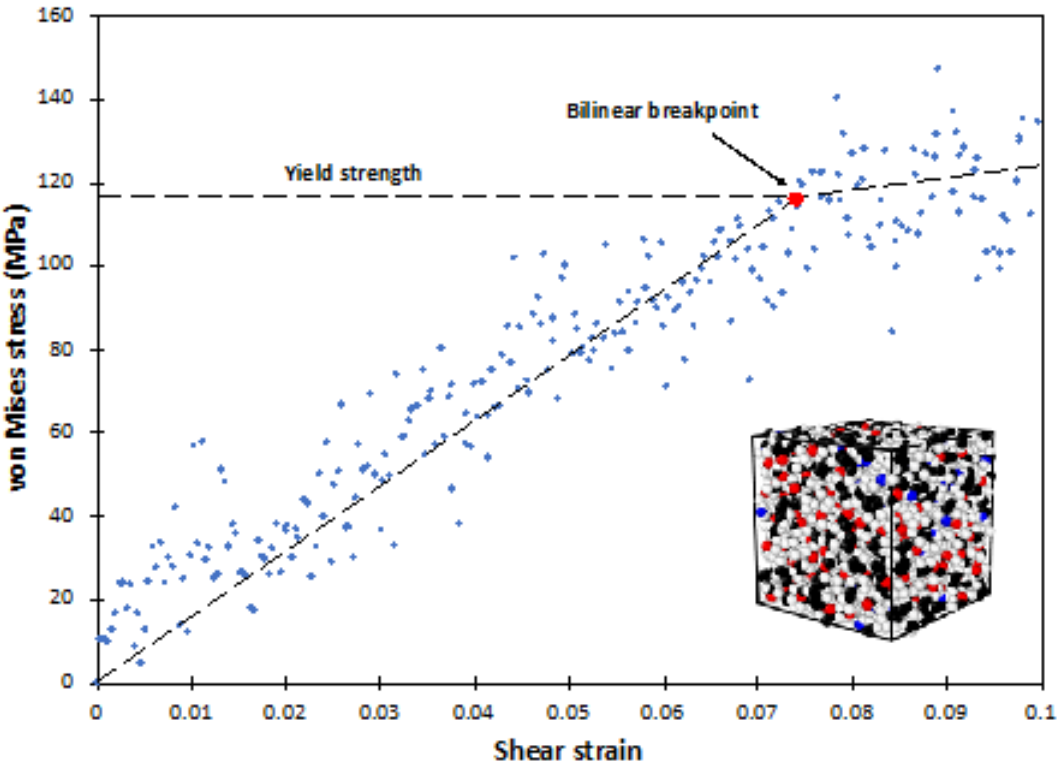

Figure 3.5: Representative von Mises/shear strain curve for EPON 862/DETDA.

predictions of T_g. It is well-known that cooling rates affect the experimental measurement of T_g [142–146]. Under laboratory conditions, rapid cooling through the T_g window does not provide the polymer molecular structure enough time to respond (via chain segment configurational changes) to rapid drops in free volume. This essentially "locks in" a non-equilibrated molecular configuration that contains different levels of free volume relative to a fully equilibrated system [144–146]. This same effect is generally not observed for heating-related T_g measurements [144]. This section discusses this phenomenon and the decision to not use correction factors for the T_g predictions in this study.

Amorphous polymer systems contain finite amounts of free volume, that is, volume pockets that do not contain any mass (a more rigorous definition is provided elsewhere [144]). At equilibrium, the amount of free volume in an amorphous polymer is dependent on the temperature of the system. In general, higher temperatures correspond to higher levels of free volume, due to increasing levels of atomic motion and repulsion, and thus thermal expansion. For a given state of temperature and free volume, there corresponds an equilibrium state of polymer chain segment configurations. It is important to note that reaching such equilibrium states at temperature below T_g can take significant amounts of time (days, weeks, years), whereas above T_g, reaching equilibrium states occurs much quicker (minutes, hours) [144].

As temperatures change, thermodynamic drivers for chain configurational changes activate. However, even though changes in temperature can be carefully controlled, the corresponding equilibrium chain configurations can take a considerably longer period of time to occur. If the cooling rate is faster than the ability of the network to respond accordingly, then the thermal contraction of the system will lock-in chain configurations that are out of equilibrium, and changes in the free volume will not be able to keep up with the thermal contraction. The faster the cooling rate, the greater the discrepancy between thermal contractions and reductions in free volume. The greater this discrepancy, the faster the system approaches the glass transition window. Thus, higher cooling rates result in higher values of "apparent" T_g.

During experimental measurements of T_g via cooling through the transition window, the specimen is initially held at the elevated temperature for a finite amount of time (seconds, minutes, hours) before ramping down. During this hold the polymer network approaches an equilibrium in terms of polymer configuration and free volume corresponding to the elevated hold temperature. When the cooling commences, the cooling rate effect described above activates.

During MD simulation of the cooling from the rubbery state (above T_g) to the glassy state (below T_g), this same effect of cooling rate on the apparent T_g is not necessarily observed. Because of the very short time scales associated with MD (nanoseconds), the cooling rate is necessarily orders of magnitude greater than that of experiment. For the simulations discussed herein, the model creation and densification occurred at room temperature (below the T_g value for both of the modeled epoxy systems). Thus, the equilibrium molecular chain segment configurations associated with the models corresponded to those at equilibrium at room temperature. Although the MD modeling process involved an annealing step and a temperature ramp-up for heating T_g predictions, these excursions to elevated temperatures occurred on very short timeframes (nanoseconds), which is orders of magnitude smaller than timeframes typically associated with high-temperature structural relaxation (seconds, minutes, hours). Therefore, at the beginning of the MD cool-down simulations for T_g prediction, the systems already had their glassy equilibrium state chain segment configurations (even though they had free volume levels of the rubbery state), and were

thus immune to experimentally-observed cooling rate effects. The predicted T_g values therefore directly relate to the T_g values experimentally measured using either heating methods or relatively slow cooling rates. Thus, no cooling rate correction factors were neither needed nor used.

3.5 Strain rate effect

The measured elastic and strength properties of polymer materials are generally dependent on the applied strain rate due to their viscoelastic nature. Molecular dynamics (MD) simulations are computationally demanding and can only simulate phenomena on very small times scales (nanoseconds). If an MD simulation includes a simulated deformation of a material to predict a mechanical property, the deformation must occur on the order of nanoseconds. Under typical laboratory conditions, experimental mechanical testing occurs over much higher time scales, such as seconds, minutes, or hours. Thus, the time scales of MD simulations and experimental testing differ by several orders of magnitude, as does their corresponding strain rates. Therefore, it is expected that predicted and measured mechanical properties should also differ significantly. This discrepancy is typically referred to as the strain rate effect.

Odegard et al. [80] first quantified the strain rate effect for the EPON 862/DETDA

system using MD techniques and the ReaxFF force field [122, 123]. MD simulations were used to predict the elastic modulus and yield strength of this epoxy system at two strain rates: $1{\times}10^{8}\ s^{-1}$, $2{\times}10^{8}\ s^{-1}$. These properties were compared to experimentally-measured modulus and yield strength values on the same material system reported by Littell et al. [147] at three strain rates: $1{\times}10^{-5}\ s^{-1}$, $1{\times}10^{-3}\ s^{-1}$, and $1{\times}10^{-1}\ s^{-1}$. Thus, the strain rates differed by as much as thirteen orders of magnitude. These comparisons of modulus and strength showed a significant discrepancy between measurements and predictions, but they also showed a clear scaling trend of the properties due to the strain rate effect. This observation was verified by Radue et al. [81] for the same epoxy system. In the current study, an approach similar to Odegard et al. [80] and Radue et al. [81] is taken for reporting Young's modulus and yield strength. That is, the predicted mechanical property values will be compared to the experimentally-measured values with the expectation that there will be a discrepancy due to the strain rate effect.

3.6 Experimental work

For mass density measurement specimens of the EPON 862/DETDA system, the neat resin was degassed at room temperature in a speed mixer at 900 *rpm* under vacuum. The curing agent was added, and the mixture was thoroughly mixed for 5 *minutes* and then further degassed in a vacuum chamber at room temperature under vacuum

for 30 *minutes*. The mixture was then cured in small aluminum dishes isothermally at 177 $^{\circ}C$ until fully cured and then cut into small pieces of varying masses for mass density measurements. A total of 10 specimens were fabricated. The mass density measurements used the Archimedes Principal method (ASTM D792).

Dynamic Mechanical Analysis (DMA) was used for the T_{g} measurements of the EPON 862/DETDA system. The DMA specimens were prepared in a closed silicone mold. Both parts of the epoxy system were thoroughly mixed in a 100:26.4 parts-by-weight stoichiometric ratio. The uncured mixture was placed into an oven set to 80 $^{\circ}C$ for 20 *minutes*. Pre-heating the resin helped reduce the viscosity for easy degassing, which was performed in a vacuum chamber for 20 *minutes* at room temperature. The degassed mixture was injected into the pre-heated silicon mold and allowed to fully cure at 177 $^{\circ}C$ for 150 *minutes*. Three fully-cured DMA specimens were then demolded and sanded to average dimensions of $35 \times 12 \times 3$ mm, conforming to the ASTM D7028-07 standard.

A TA Instruments Q800 DMA was used to determine the T_{g} of the three specimens. During the test, a sinusoidal displacement with an oscillation frequency of 1 Hz was applied to the specimens. The specimens were subjected to temperature sweeps (ramping from 20 $^{\circ}C$ to 250 $^{\circ}C$ at 5 $^{\circ}C/min$) in a single cantilever beam configuration. The tanδ response of the specimens was monitored over the entire range, and the peak tanδ value was taken as the corresponding T_{g} value.

3.7 Results

The results of MD predictions and experimental measurements are presented in this section. All uncertainty values represent the standard error of replicate simulations/measurements. **Tables 3.4** and **3.5** list the predicted mass density values for the EPON 862/DETDA and EPON 828/DDS systems, respectively, along with the corresponding densities from the experiments described herein for the EPON 862/DETDA system and from the literature for EPON 828/DDS systems [148]. The results indicate that the MD predictions with IFF-R agree closely with experiment for both systems.

Tables 3.4 and **3.5** list the predicted and experimental thermal properties of the two epoxy systems. The experimental T_g results for the EPON 862 system are those described herein, while the remaining results are from the literature [148–150]. The predicted T_g values are listed for both the heating and cooling cycles. The results indicate that the predicted properties generally match the experimental values closely for T_g, CTE below T_g, and CTE above T_g. It's important to note that the predicted heating and cooling values for T_g in **Tables 3.4** and **3.5** are in agreement with each other. This observation supports the discussion above regarding the effect of cooling rates on the predicted thermal response of an amorphous polymer modeled with the MD procedure used herein. Because the MD systems were initially formed

and densified below T_g, the sub-T_g configurational structure is locked in and thus the general approach to T_g prediction (heating vs cooling) does not affect the results.

Table 3.4
Properties for EPON 862/DETDA.

Property	**MD prediction**	**Experiment**
Mass density (g/cc)	1.204 ± 0.003	1.193 ± 0.001
T_g ($^\circ C$)	154.8 ± 9.1 (heating) 155.1 ± 3.0 (cooling)	153.8 ± 0.3
CTE below T_g ($\times 10^{-5}$ C^{-1})	7.95 ± 0.33	6.41 [149]
CTE above T_g ($\times 10^{-5}$ C^{-1})	16.01 ± 0.60	18.59 [149]

Table 3.5
Properties for EPON 828/DDS.

Property	**MD prediction**	**Experiment**
Mass density (g/cc)	1.226 ± 0.002	1.240 [148]
T_g ($^\circ C$)	184.7 ± 3.7 (heating) 183.7 ± 10.6 (cooling)	159 – 186 [148], [150]
CTE below T_g ($\times 10^{-5}$ C^{-1})	6.58 ± 0.20	6.90 [150]
CTE above T_g ($\times 10^{-5}$ C^{-1})	16.40 ± 0.87	17.6 [150]

Figures 3.6 and **3.8** show the predicted and experimental [147, 148, 151] Young's modulus and yield strength values, respectively, of the two epoxy systems with respect to the strain rate. For the experimental values from Gilat et al. [151], the published strain-rate dependent shear tests results were used for the data points in **Figures 3.6** and **3.8**. The shear modulus and shear stress at yield were obtained from the published stress-strain curves and analyzed with the same procedure as described elsewhere [80]. These values were subsequently converted to Young's modulus

(assuming a Poisson's ratio of 0.4 [147]) and yield strength as explained above for the predicted values from MD simulation. A best-fit logarithmic regression of the EPON 862/DETDA experimental values (from both experimental references) is included on each graph and extrapolated to the simulated strain rates.

The data in **Figures 3.6** and **3.8** demonstrates that the predicted properties show general agreement with the experiment considering the influence of the strain rate. It is important to note that the magnitude of discrepancy between the experiment and predictions is significantly smaller than that reported by Odegard et al. [80] for the ReaxFF force field [122] with the Liu parameter set [123]. Specifically, the comparisons of modulus of Odegard et al. [80] showed a predicted modulus that was about 68 % higher than the measured modulus at the 1×10^{-1} s^{-1} strain rate. The predicted yield strength was about 100 % greater than the measured yield strength at the same strain rate. In the current study, at the same experimental and computational strain rates, the predicted modulus is about 22 % higher than the experimental modulus, and the predicted yield strength is about 33 % higher. This difference in the discrepancies in predicted and measured properties from two different force fields indicates that the force constants and functional forms associated with different force fields can have a significant impact on the magnitude of the apparent strain rate effect. Because force constants are phenomenological in nature, there is no clear physical reasoning for this. Regardless, it is clear that IFF-R predicts properties that are closer to those measured experimentally than does ReaxFF with the Liu parameter

set, and the apparent strain rate effect is substantially smaller.

It is also important to discuss the trendlines for the 862/DETDA experimental data shown in **Figures 3.6** and **3.8**. The logarithmic trendlines were used only for the purpose of showing an approximate linear trend on the logarithmic strain rate scale. That is, they have no physical significance. For the modulus trend shown in **Figure 3.6**, the logarithmic trendline demonstrates an excellent fit to both the experimental and predicted data. For the yield strength data shown in **Figure 3.8**, the trendline does not match the predicted data with the degree of accuracy found in **Figure 3.6**. This simply means that a logarithmic trendline does not completely capture the physics of the strain rate effect on the yield strength. It is close, but not perfectly accurate. Perhaps, in the future, more data can be captured and more sophisticated fitting techniques can be explored to capture the physical trends observed with yield strength over numerous orders of magnitude of strain rate.

Tables 3.6 shows a comparison of the Young's modulus predictions of the 862/DETDA system with the predictions from other MD-based studies from the literature [80, 81, 152–154]. Experimental values from the literature are also included in the table [147, 151]. Although there are numerous MD-based studies in the literature for the 862/DETDA system, only those with reasonable mass density predictions were chosen for this comparison. From the data in the table, the Class I force fields generally show the closest agreement with experiment, and do not appear to show any

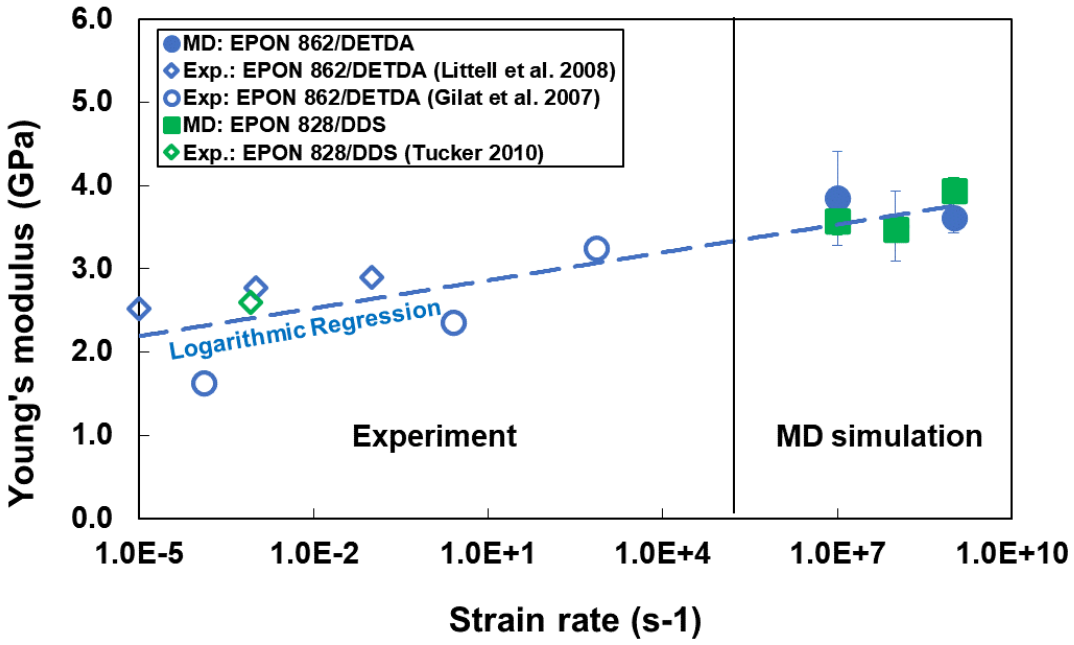

Figure 3.6: Young's modulus vs strain rate for both epoxy systems. The EPON 862/DETDA logarithmic regression line is fit to both sets of EPON 862/DETDA experimental data.

significant strain rate effect. The predictions with ReaxFF generally show the largest values of Young's modulus and the largest magnitude of strain-rate effect, while the IFF-R predictions are slightly smaller than the ReaxFF predictions. It is important to note that experimental measurements of Young's modulus at MD-level strain rates are not available, so the true magnitude of the strain rate effect is not known. However, the trend in the data in **Figure 3.6** shows reasonable evidence that a significant strain rate exists, which indicates that the IFF-R and ReaxFF predictions are more reasonable than the Class I predictions.

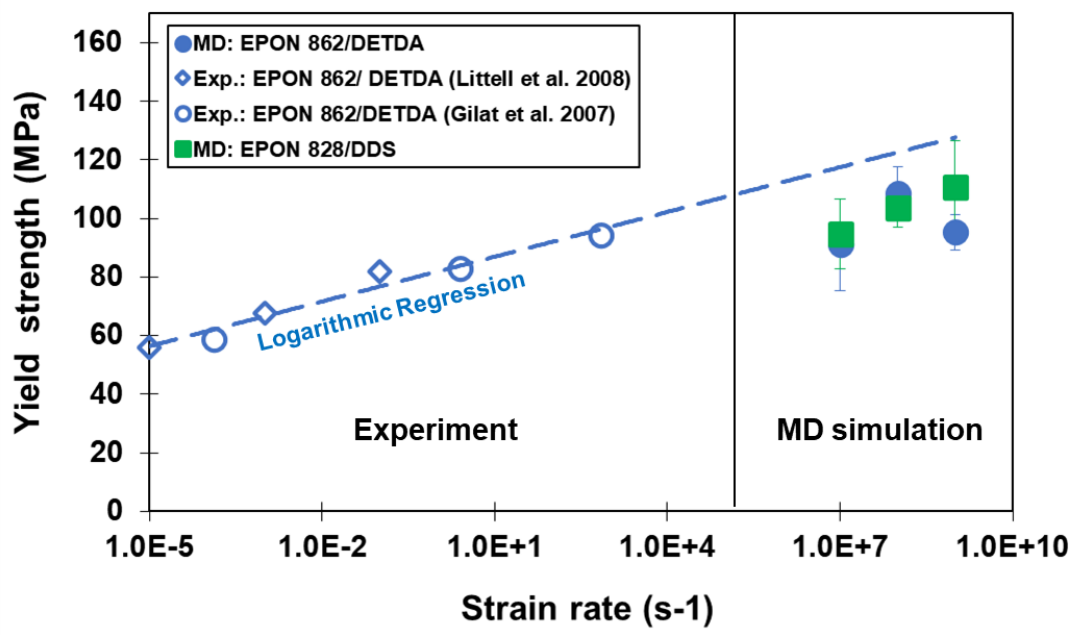

Figure 3.7: Yield strength vs strain rate for both epoxy systems. The EPON 862/DETDA logarithmic regression line is fit to both sets of EPON 862/DETDA experimental data.

Table 3.6
MD predicted Young's modulus for EPON 862/DETDA.

Simulation study	**Force field (type)**	**Predicted Young's modulus** (GPa)
Current study	IFF-R [13] (Class II/reactive)	3.5 – 3.8
Odegard et al. [80]	ReaxFF [122, 123] (Reactive)	4.9 – 5.1
Radue et al. [81]	ReaxFF [122, 123] (Reactive)	3.5
Vashisth et al. [154]	ReaxFF [122, 155] (Reactive)	5.0 – 6.0
Kallivokas et al. [153]	DREIDING [117] (Class I)	2.6
Bandyopadhyay et al. [152]	OPLS [118] (Class I)	2.3
Experiment [147, 151]	-	1.6 – 3.3

The predicted Poisson's ratios of the EPON 862/DETDA and EPON 828/DDS systems were 0.40 ± 0.01 and 0.41 ± 0.01, respectively. The experimental value of the Poisson's ratio for the EPON 862/DETDA system is 0.40 [147], which matches

the prediction. Poisson's ratio values that approach the isotropic elastic limit (0.5) typically are not significantly affected by viscoelastic effects [156], thus they are not expected to demonstrate a significant strain rate effect.

Figures 3.8 and **3.9** shows the Young's modulus and yield strength of EPON 862/DETDA system calculated from bulk modulus and shear modulus, that is from the (K,G) pair and predicted directly from the tensile MD simulations. No significant difference was observed in the predicted values from both methods. The tensile simulations were performed similar to as described in [80] with an axial tensile strain of 10 % and a strain rate of $2\times10^{8}\ s^{-1}$.

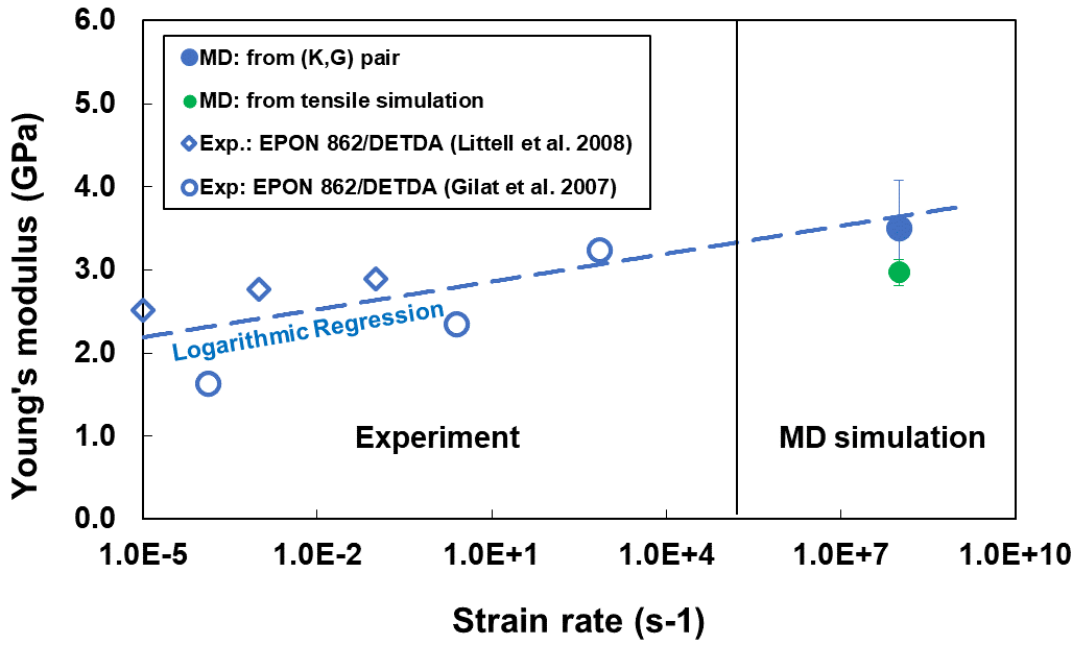

Figure 3.8: Young's modulus vs strain rate for EPON 862/DETDA epoxy systems predicted using (K,G) pair and from tensile simulations. The EPON 862/DETDA logarithmic regression line is fit to the EPON 862/DETDA experimental data.

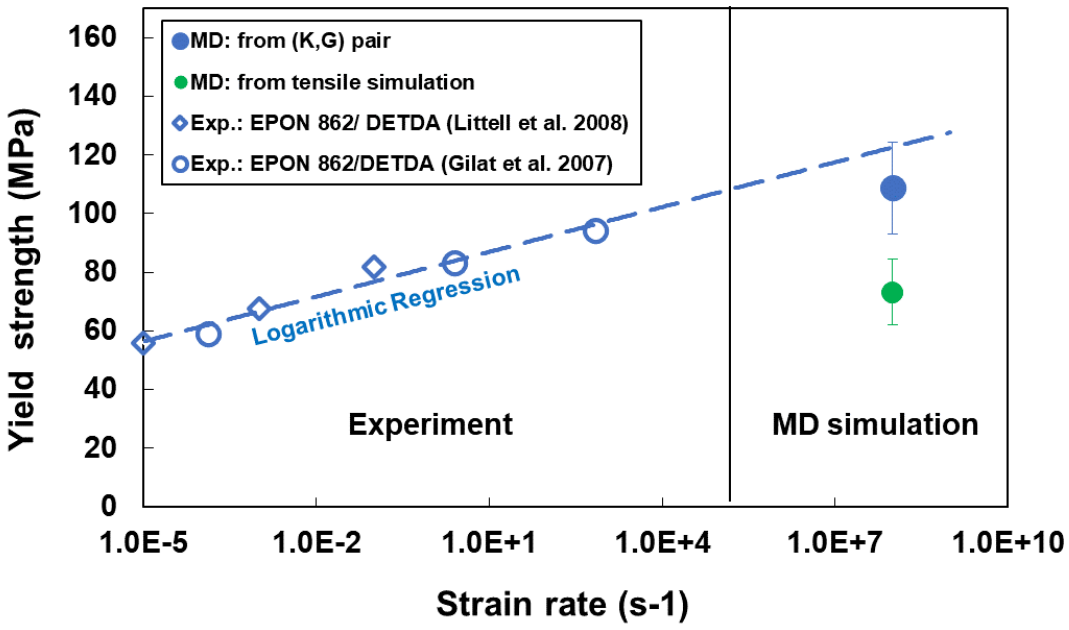

Figure 3.9: Yield strength vs strain rate for EPON 862/DETDA epoxy systems predicted using (K,G) pair and from tensile simulations. The EPON 862/DETDA logarithmic regression line is fit to the EPON 862/DETDA experimental data.

3.8 Conclusions

In this study, the accuracy of IFF-R for amorphous polymer systems was assessed. MD simulations were used to predict the thermo-mechanical properties of three different fully cured/crosslinked epoxy systems with an aromatic crosslinking agents. The results indicate that IFF-R yields values of mass density, Young's modulus, Poisson's ratio, yield strength, T_{g}, and CTE that are consistent with experimental measurements.

The importance of these results is in the utility of IFF-R relative to other force fields used for simulating amorphous polymer systems. IFF-R incorporates the advantages of fixed-bond force fields (simulation efficiency, mathematical simplicity, physical relevance of force constants) with the advantages of reactive force fields (accurately simulating the response of covalent bonds stretched to large deformations). As a result, IFF-R is an efficient force field with force constants that can be easily accessible, and can simultaneously predict the behavior of material systems subjected to relatively large deformations. The results of this study verify that IFF-R yields predicted thermal and mechanical properties that are consistent with experiment. With this verification, IFF-R can now be used to confidently and efficiently simulate similar material systems subjected to large deformations in which the bond stretching moves beyond the harmonic regime. This is a significant advancement in the field of

molecular-level polymer design and simulation.

Chapter 4

Reactive Molecular Dynamics Simulation of Epoxy for the Full Crosslinking Process at Room and High Temperatures

4.1 Introduction

Thermosetting epoxies are an excellent candidate to be utilized for variety of applications in the aerospace industry. They possess excellent mechanical, thermal, and

electrical properties [157]. In addition, epoxies are widely-used for benchmarking research as they are inexpensive, and epoxy-based composites are relatively easy to fabricate following simple curing protocols [158]. During the curing of composite panels, the epoxy matrix is subjected to elevated temperatures and the corresponding thermo-mechanical properties evolve as the curing progresses. Additionally, the epoxy matrix experiences shrinkage during the cure process. Because the evolving matrix thermo-mechanical properties and shrinkage drives the development of residual stresses in composite panels during the curing process, a better understanding of the evolution of these properties is important for optimizing the composite processing parameters. The full experimental characterization of composite property/shrinkage evolution is time-consuming and expensive.

Molecular dynamics (MD) is a powerful tool to simulate molecular behavior and provide insight into the effect of temperature, pressure, and other design parameters on the complex networked molecular structure that epoxies possess [140, 159]. As a result, these simulations can also provide atomistically-informed predictions of the evolution of thermo-mechanical properties and shrinkage of epoxy during processing. All MD techniques utilize a force field to describe the interaction of bonded and non-bonded atoms in the molecule. The correct choice of force field based on the design objectives is necessary to accurately simulate molecular behavior and predict accurate properties [113, 160].

For decades, MD simulations of polymer-based engineering materials have been mostly limited to using fixed-bond force fields with harmonic bonds, that is, force fields that do not simulate the formation or scission of covalent bonds. Specifically, MD modeling studies3 for neat epoxies have employed various fixed-bond force fields such as OPLS-UA [152, 161], CHARM and cff91 [132], CVFF [162, 163], PCFF [134], Dreiding [139, 153, 164–167], and COMPASS [168–171], AMBER [172], MMFF [173]. Reactive force fields allow for the direct simulation of the formation and/or scission of covalent bonds during the simulated deformation process, thus allowing for accurate predictions of strength and mechanical properties at large deformations. In particular, the reactive force field ReaxFF has been used to simulate epoxy systems and accurately predict mechanical properties [80, 81, 154]. However, ReaxFF is highly complex, thus MD simulation times utilizing this force field are prohibitively long and limited to relatively small simulations.

Recently, Winetrout et al. [13] developed the Reactive Interface Force Field (IFF-R) which combines the efficiency of a fixed-bond Interface force field (IFF) [12] with the capability of simulating bond scission. IFF-R replaces the traditional harmonic bond-stretching potential with a morse potential to model covalent bond dissociation in response to large local mechanical deformations. Pisani et al. [174] used IFF-R to simulate polyamide nanocomposites, and Odegard et al. [175] demonstrated the capability of IFF-R for accurately predicting mechanical properties of fully-cured epoxy systems. However, IFF-R has not yet been used to simulate partially-cured

epoxy systems.

All of the MD modeling studies of epoxy cited above provide predicted properties for either a fully cured epoxy or a semi-cured epoxy at a limited number of intermediate crosslinking densities. None of these studies provide predicted properties for a large range of crosslink densities, which is necessary for comprehensive, multiscale process modeling methods for optimizing thermo-mechanical properties of epoxy composites and minimizing process-induced residual stresses [176–181]. Further, the accuracy of predicted mechanical properties using MD are highly dependent on the accurate prediction of the mass density, which represents the bulk density of the polymer [173]. All the MD studies discussed above that employ fixed-bond force fields show a significant discrepancy between their MD predicted mass density and the experimentally measured bulk density of the respective material. This discrepancy manifests in inaccurate prediction of mechanical properties, which adversely effects the prediction of residual stresses in a multiscale process modeling framework. The above-cited studies that utilize ReaxFF demonstrate accurate prediction of mass density but do so at the expense of model size and efficiency.

This work utilizes MD simulation to accurately predict the physical and mechanical properties of an epoxy system at varying degrees of cure ranging from fully uncrosslinked to fully crosslinked states at room temperature (300 K, 27 $^{\circ}C$). This

study implements IFF-R to accurately predict physical and mechanical properties corresponding to large deformations. The modeling approach is validated herein using experimental characterization of the epoxy system. The results of this study provide the input necessary for comprehensive process modeling of epoxy composites, and key insight into the gelation process of epoxy during curing.

4.2 Molecular Modeling

4.2.1 Material System and Force Field

For this study, an epoxy system comprised of diglycidyl ether bisphenol F (DGEBF) resin and diethyltoluenediamine (DETDA) hardener was modeled using the IFF-R force field. **Figure 4.1** shows the molecular structures of both monomers. The LAMMPS [3] software package was used to perform all the MD simulation for this work. The properties predicted are the bulk mass density (ρ), post-gelation volumetric shrinkage, bulk modulus (K), shear modulus (G), Young's modulus (E), Poisson's ratio (ν), and yield strength (σ). The energy terms associated with IFF-R and ReaxFF are described in the supplementary information (**Appendix B.1**).

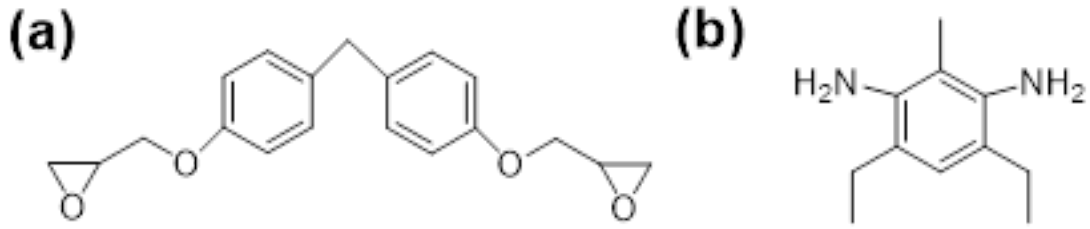

Figure 4.1: Molecular structure of (a) DGEBF (EPON 862) resin and (b) DETDA (Epikure W) hardener.

4.2.2 Model Setup

For the first step in the MD modeling procedure, a series of equilibrated MD models were constructed. First, both the monomers were assigned IFF-R parameters and combined in a large orthogonal simulation box with a resin-to-hardener ratio of 2:1. The system was replicated to produce 90 monomers of DGEBF and 45 monomers of DETDA to create a low-density MD model containing 5265 atoms. To allow the monomers to mix, a fixed-volume and fixed-temperature (NVT) simulation was performed over 100 ps with 1 fs time steps at 600 K. Following this mixing simulation, the simulation box was slowly compressed (densified) to a target density of 1.17 g/cc. This simulation occurred at 300 K over 8 ns at 1 fs time steps. After densification, an annealing simulation was performed, during which the temperature was ramped from 300 K to 600 K and then slowly cooled to 300 K at a 20 K/ns cooling rate with the NVT ensemble. A fixed-pressure and fixed-temperature (NPT) simulation was

performed at 300 K and 1 atm for 1 ns with 1 fs timesteps to allow the atoms to reconfigure and attain stable energy positions. By repeating this procedure, 5 different replicates were created to account for statistical deviations in predicted properties. The Nose-Hoover thermostat and barostat were implemented for all the simulations discussed herein [84–86]. Once all the 5 replicates were annealed and relaxed, the next step was crosslinking.

4.2.3 Model Setup

The DGEBF/DETDA epoxy system follows a two-step crosslinking reaction [81]. In the first step, the epoxide ring of one DGEBF monomer opens, and the exposed epoxide carbon reacts with a nitrogen from a primary amine ($-NH_2$) of DETDA and forms a hydroxyl group and a secondary amine ($-NH$). In the second step, the newly formed secondary amine reacts with the epoxide carbon of another DGEBF monomer to form a tertiary amine ($-N$) and a second hydroxyl group. The `fix bond/react` command developed by Gissinger et al. [91] in LAMMPS was implemented to simulate these reactions. This command allows for the simulation of user-defined crosslinks. The required pre-reaction, post-reaction, and mapping templates were created accordingly. These simulations were performed at 450 K with 0.1 fs timesteps. Individual models with crosslinking densities varying from 0 to 0.95 were

created for all 5 replicates. Here, the crosslinking density (ϕ) is defined as the ratio of number of crosslinks formed to the maximum possible crosslinks that could be formed in the entire system. A video titled crosslinking.mp4 showing the covalent bond breaking and formation between two DGEBF monomers and one DETDA hardener is added in the supplementary information (**Appendix B** [182]). The video is rendered using OVITO [78] visualization software. During these simulations, the density and volume of the simulation boxes were tracked. Following the crosslinking, an NPT simulation was performed for each crosslinking density at 300 K for 1 ns at 1 fs timesteps to relax the model and to predict the final density and volume. The volumetric shrinkage was calculated as the percent change in the volume of the crosslinked model at specific crosslinking densities, with respect to the uncrosslinked model. For all simulations, the Nose-Hoover barostat was set to maintain a 0.101 MPa (1 atm) pressure on all sides of the simulation box.

Two crosslinking strategies were investigated as shown in **Figure 4.2**. For the non-sequential approach, each crosslinked model was generated starting from the same uncrosslinked ($\phi = 0$) model. That is, crosslinking steps were performed directly from 0 to 0.1, 0 to 0.2, and so on, up to the last step, 0 to 0.95. For the sequential approach, each crosslink density was achieved from the increment before it. That is, crosslinking was performed from 0 to 0.1, then 0.1 to 0.2, and so on up until the final increment of 0.9 to 0.95. The progressive building of crosslinks in the sequential strategy mimics the actual curing of polymers and hence was adopted for this study. In addition,

a comparison of properties such as mass density, post-gelation volumetric shrinkage and bulk modulus predicted from both strategies is included in the supplementary information (**Appendix B.2**). For both the strategies, a crosslinked MD model was built individually for each crosslinking density at 450 K and was cooled to 300 K. Afterwards, an NPT simulation at 300 K and 1 atm was run for 1 ns to relax the models and allow the crosslinked molecules to attain minimum energy states.

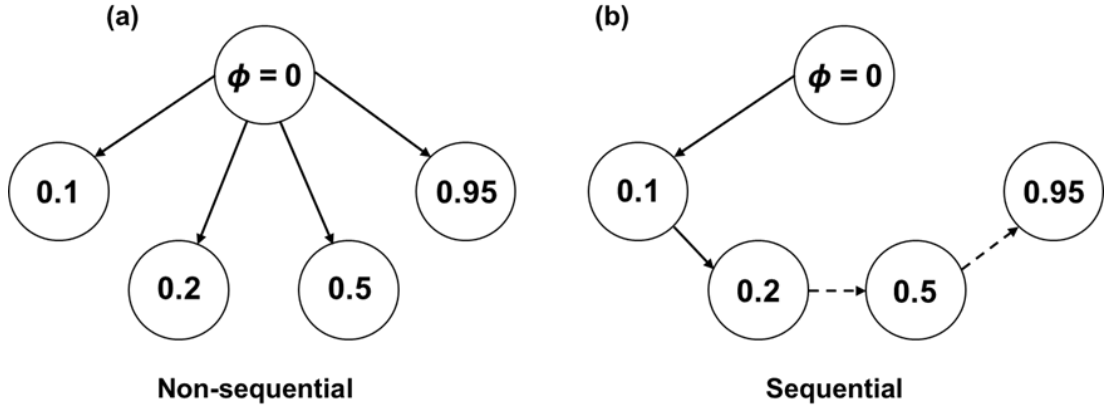

Figure 4.2: Crosslinking strategies (a) non-sequential, (b) sequential.

4.2.4 Gel point prediction

According to Flory [183], an infinite network is formed at the polymer gel point where a single molecule is large enough to span the entire length of the system. Here, the largest molecule represents the largest cluster (group of connected polymer units) in the simulation box. **Figure 4.3**a shows the growth of largest cluster as a function of varying crosslinking density for a representative system. The gel point can be

predicted via MD simulation by tracking the molecular weight of the largest cluster, the molecular weight of the second-largest cluster, or the weight-averaged reduced molecular weight (RMW) of the system [162, 184, 185]. The RMW is the molecular weight of the entire system except the largest cluster. When using the largest cluster metric, the inflection point at which the largest cluster molecular weight drastically increases marks the gel point. When using the other two metrics, the gel point occurs at the point where the corresponding molecular weight reaches a peak value.

In this work, the gel point was predicted using all three methods. **Figure 4.3**b shows representative results for all three metrics for one replicate. The average gel points of the five replicates were 0.63, 0.60, and 0.62 for the largest cluster, second-largest cluster, and RMW metrics, respectively. These values agree well with other modeling results from the literature for the same epoxy system [162, 184, 185]. **Figure 4.3**a shows representative snapshots of the largest cluster at different crosslinking densities, demonstrating the evolution of an infinite network in a periodic simulation box. The Cluster analysis modifier in OVITO [78] visualization software was implemented to generate these images. When the crosslinking begins, the simulation box contains only monomers. As the crosslinking progresses, covalent bonds form between the monomers and the network starts to grow. In **Figure 4.3**a, at 0.2 crosslinking density, the network formation initiates. At a crosslink density of 0.4, the network is not yet large enough to span the entire simulation box. Finally, at 0.7 the largest cluster spans the simulation box, which indicates that a continuous load-carrying covalent

bond network exists in each direction, and the polymer has reached the gel point. The gel point generally varies between replicates and is highly dependent on the starting molecular configuration. The value of $\phi = 0.6$ was chosen as the gel point of this system for calculation of the post-gelation volumetric shrinkage because it is the simulated value that is closest to the average gel points predicted using all three metrices.

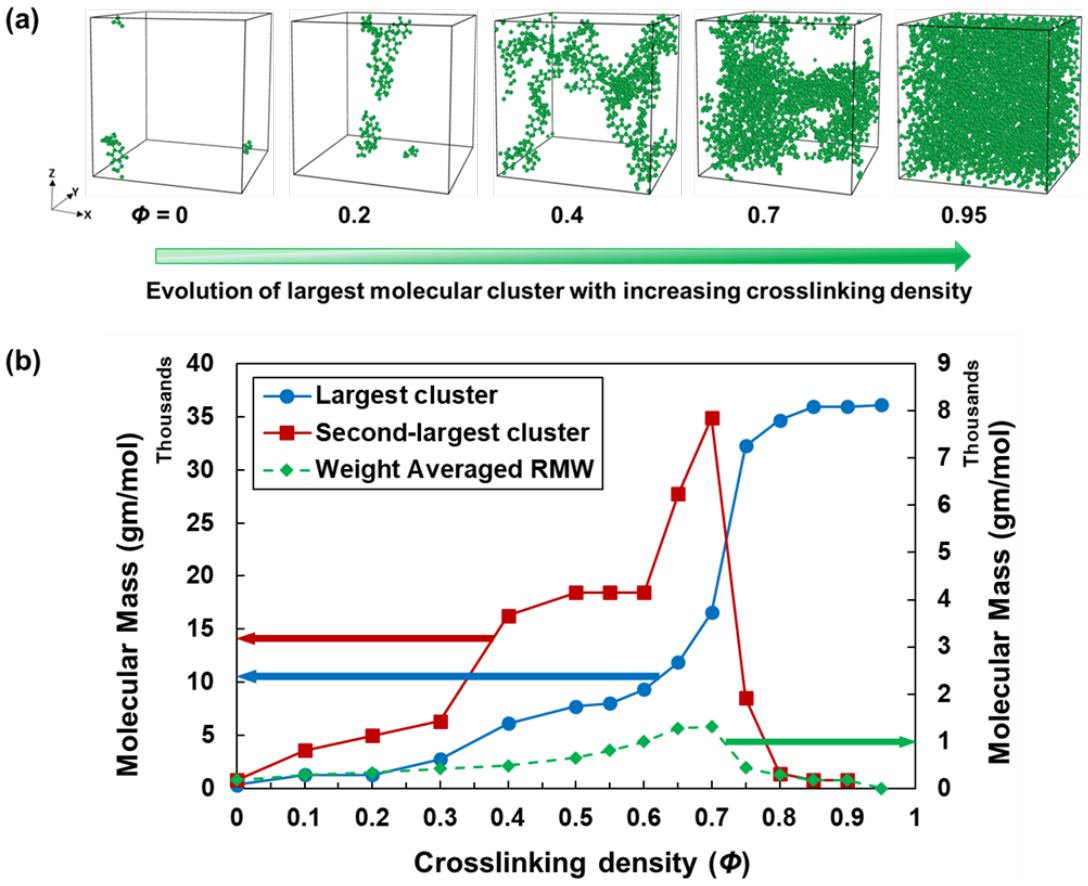

Figure 4.3: (a) Snapshots of largest cluster and (b) Molecular mass as a function of varying crosslinking densities for a representative system.

4.2.5 Mechanical deformations Simulations

The next step in the analysis was to perform simulated mechanical deformations. Here, K, G, E, ν and σ for each crosslinking density for all replicates were predicted by implementing the similar simulation procedures as outlined by Odegard et al. [175]. For each replicate and crosslink density, K was predicted from 1 atm and 5000 atm NPT simulations at 300 K, and G was determined from shear deformations in the three principal planes. The (K, G) pair was then used to predict the (E, ν) pair using the standard relations for linear elastic isotropic materials [133]. The yield strength was predicted using the von Mises stress calculated from the shear deformations [175]. A detailed description of the procedure and necessary equations implemented in this work to predict the mechanical properties using the MD simulation results is included in the supplementary information (**Appendix B.4**)

4.3 Experimental details

The experimental procedure for the measurement of the mass density is described by Odegard et al. [175]. This section describes the measurement of gel point, volumetric shrinkage, and mechanical properties for the DGEBF/DETDA epoxy.

4.3.1 Specimen Preparation

The DGEBF/DETDA epoxy resin system components were first measured according to a stoichiometric ratio of 100:26.4 (parts by weight) and then mixed thoroughly by hand for two minutes at room temperature. Significant air entrapment as a result of the mixing process was observed. To eliminate the trapped air, the uncured resin mixture was first heated in an oven held at 80 $^{\circ}C$ for 20 *minutes*, then degassed at room temperature for an additional 20 *minutes*. The heating step served as a means to reduce the resin viscosity for a more effective degassing procedure. For the gel point and volumetric shrinkage characterization described below, the degassed mixture was directly tested in this state. For the mechanical characterization, the degassed mixture was injected into an open-faced mold for full curing of tensile test specimens. The specimens were manufactured according to ASTM D638 Type I specifications. Once fully cured and cooled to room temperature, each specimen was water-polished to eliminate any irregularities found in the cross-sectional area along the gage length of the specimen as a result of curing in open-faced molds. After polishing, a black/white contrasting speckle pattern was applied to the specimens in preparation for 2-D Digital Image Correlation (DIC) strain measurement [186, 187] during tensile testing.

4.3.2 Gel point and volumetric shrinkage testing

In order to experimentally evaluate the gel point and the post-gelation chemical shrinkage (ϵ_{sh}) of the DGEBF/DETDA epoxy, a rotational rheometer (ARES-G2, TA Instruments) with a parallel plate setup was used. The resin mixture, prepared following the aforementioned procedure, was injected between the parallel plates which had an initial gap $h_0 = 1.5 \pm 0.05\ mm$. The mixture was then rapidly heated to the desired temperature and allowed to soak under isothermal conditions. For this study, the tests were conducted at two isothermal temperatures of 150 $^\circ C$ and 170 $^\circ C$.

Gel point measurements were carried out in gap-control mode. As the resin mixture cured, it was subjected to an oscillating shear strain which induced a shear stress in the curing resin. The complex shear modulus G, decomposed into its elastic storage shear modulus G' and viscous loss shear modulus G'', was measured by the rheometer. The point during the cure process at which both G' and G'' intersect (have equal values) indicates the transition of the material from a primarily liquid/viscous to solid/elastic phase. This point was used to determine the time to gelation [139]. Considering the time-temperature history of the rheology test, the degree of cure corresponding to the gel time was calculated from the kinetic model for DGEBF/DETDA [188]. An average gel point, across four tests performed at the two different isothermal temperatures, was found to be 0.71, which is in excellent agreement with experimental data found

in the literature for the DGEBF/DETDA [189] epoxy system.

Evaluation of post-gelation volumetric shrinkage (ϵ_{sh}) was performed with the same rheometer setup as the gel point measurement. To measure post-gelation chemical shrinkage (as determined above), the instrument was operated in force-control mode during which a normal force of 0.1 N was applied to maintain contact between the shrinking specimen and the plates. The linear variation ($h - h_0$) in the gap h resulting from the chemical shrinkage in the specimen was continuously monitored by the instrument. The ϵ_{sh} resulting from the cure was computed using

$$\epsilon_{\text{sh}} = \left[1 + \frac{1}{3}\left(\frac{h - h_0}{h_0}\right)\right]^3 - 1 \tag{4.1}$$

This relationship assumes that there are no in-plane strains in the specimen and the material is incompressible (ν=0.5). The average post-gelation volumetric shrinkage in the fully-cured specimens was 2.36 $\pm$ 0.08%. With the knowledge of the time-temperature history of the test, the degree of cure was computed using the kinetic model described elsewhere [188]. Figures showing the measured post-gelation volumetric shrinkage as a function of time and degree of cure are included in the supplementary information (**Appendix B.3**).

4.3.3 Mechanical testing

The tensile test specimens were tested according to ASTM D638 guidelines to determine the tensile stiffness, Poisson's ratio, and 0.2 % offset yield strength. Each specimen was subjected to a uniaxial tensile load using an MTS Model 43.104 electromechanical test machine in displacement control mode with a crosshead displacement rate of 2 mm/min. During specimen deformation, photographs were captured at even intervals throughout the test up to the point of fracture. A FUJIFILM X-T3 26.1-megapixel camera was utilized for acquiring the photographs.

The open-sourced DIC platform Ncorr [186, 187] built within Matlab was used for the DIC analyses after tensile testing was completed. In performing DIC analyses, deformations of the patterned specimens under loading were measured relative to a reference (undeformed) image through image recognition algorithms [186]. As a result, axial and transverse full-field strains within a user-specified region of interest (ROI) were calculated for each photograph taken during a given test. In this characterization procedure, the full-field strains were averaged for each photograph and then correlated to the corresponding time, load, and displacement readings provided by the MTS apparatus. The ROI was selected to be within the gage area as specified in ASTM D638-14. Post-processed data was in the form of stress-strain curves; one for each test specimen.

Characterization of modulus, Poisson's ratio, and offset yield strength was performed using only data from tests in which the specimen fractured within the gage area as designated by ASTM D638. Young's modulus was calculated by performing a fit of the initial linear region of the stress-strain curve up to 1 % strain. Poisson's ratio was determined by taking a linear fit of the negative of the strains in the transverse direction divided by the strains the axial direction. The yield strength was measured as the stress corresponding to the strain 0.2 % offset from a deviation of the proportional limit of the stress-strain curve. The strain rate was estimated by calculating the average of the slope of adjacent strain-time datapoints.

4.4 Results

This section describes the results of the MD simulations. For each of the plots provided in this section, the black dots represent MD predictions, and the error bars represent the standard error associated with the predictions of the replicate models. All curve fits to the MD data shown in this section were performed using equations that best matched the form of the data using OriginPro [190] data analysis software. The MD predicted properties for the fully crosslinked model ($\phi = 0.95$) are compared with experimentally measured values from the current work and from the literature.

4.4.1 Mass density

Figure 4.4 shows the mass density as a function of crosslinking density at room temperature. The predicted mass density at 300 K for the fully crosslinked system ($\phi = 0.95$) is found to be 1.207 $\pm$ 0.003 g/cc. This value agrees well with the experimentally-measured value of 1.193 g/cc for fully cured DGEBF/DETDA epoxy in this work. The MD prediction at $\phi = 0.95$ is also compared with experimental value of 1.20 g/cc from the literature [191, 192]. The mass density gradually increases with increasing crosslinking density. This can be attributed to increased network connectivity due to the formation of covalent bonds between the monomers, which reduces the distance between monomers and thus increases the mass density. It can also be seen from **Figure 4.4** that the MD predicted mass density for the fully crosslinked system agrees well with the experimental data from literature and from this work. It is also noteworthy that the literature values show closer agreement with the predictions than the experimental values from this work. This suggests that there is a wide range of experimental values due to differences in the sample preparation procedures and mass density measurement techniques. The mass density data was fitted with a second-order polynomial with $R^2 = 0.998$ as defined by

$$\rho\left(\frac{g}{cc}\right) = \left(-0.065 \times \phi^2\right) + (0.142 \times \phi) + 1.128 \tag{4.2}$$

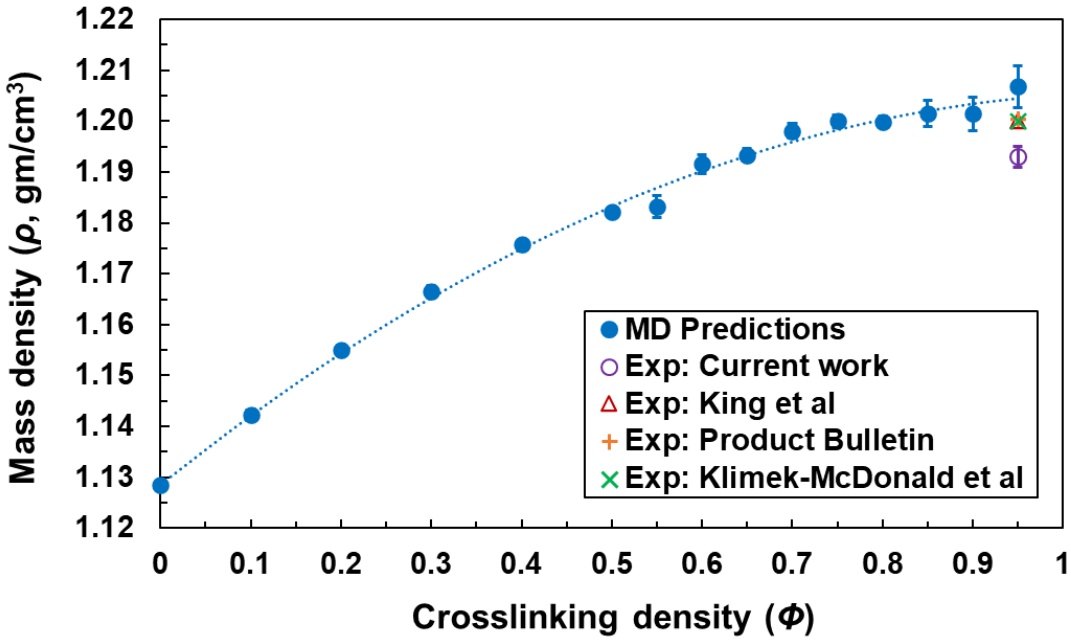

Figure 4.4: Predicted mass density as a function of crosslinking density at room temperature.

4.4.2 Volumetric shrinkage

Figure 4.5 shows the total volumetric shrinkage as a function of crosslinking density at room temperature. The predicted shrinkage for the fully crosslinked system ($\phi = 0.95$) is 6.496 ± 0.184 %. This agrees well with the shrinkage observed during experimental curing of epoxy resins [140]. The volumetric shrinkage gradually increases with increases in crosslinking density because of the formation of covalent bonds. The MD data was fitted using a second-order polynomial with $R^2 = 0.994$ showing a non-linear dependence between volumetric shrinkage and crosslinking density as defined

by

$$\text{Volumetric shrinkage } (\%) \;=\; \left(-5.806 \times \phi^2\right) + (12.146 \times \phi) + 0.044 \qquad (4.3)$$

A similar non-linear trend was observed for this epoxy system using the Dreiding force field [166].

The inset in **Figure 4.5** shows the post-gelation volumetric shrinkage, which is calculated as the change in volume of the crosslinked model with respect to volume of model at $\phi = 0.60$ at the onset of gelation. The MD predicted post-gelation volumetric shrinkage at $\phi = 0.95$ is 1.543 ± 0.417 % at room temperature. This value agrees well with the experimentally measured value of 2.36 ± 0.08 % in this work. The MD data was fitted using a linear curve fit with $R^2 = 0.912$ showing a linear dependence between post-gelation volumetric shrinkage and crosslinking density as defined by

$$\text{Post-gelation volumetric shrinkage}\,(\%) \;=\; (3.545 \times \phi) - 2.003 \qquad (4.4)$$

This linear dependence between post-gelation shrinkage and crosslinking density is in general agreement with the experimentally-observed linear dependence between post-gelation shrinkage and degree of cure as shown in supplementary information

(**Appendix B.3**).

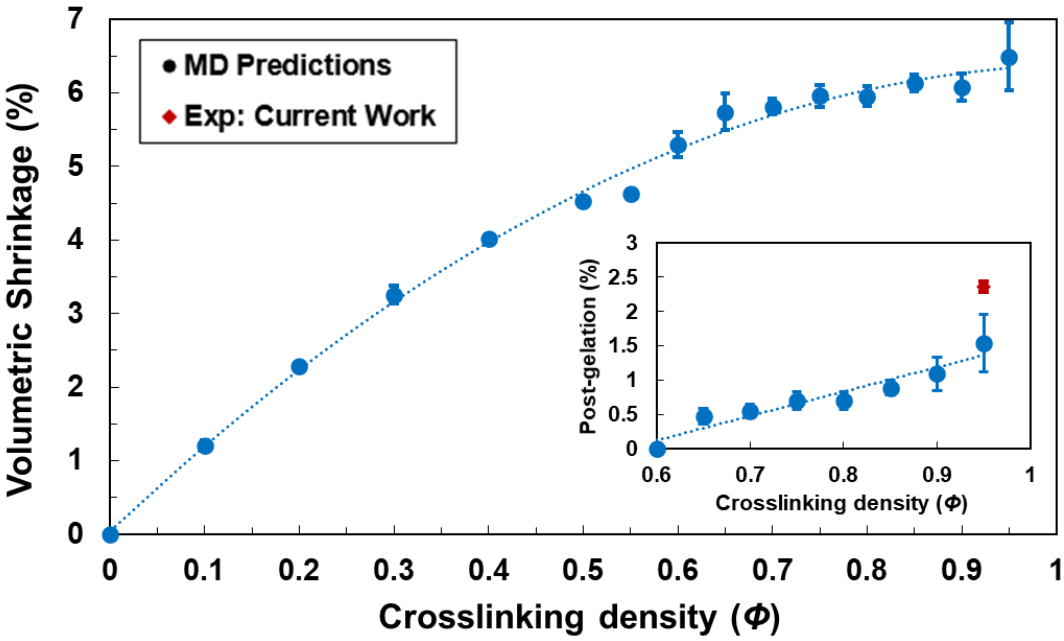

Figure 4.5: Predicted volumetric shrinkage as a function of crosslinking density at room temperature. Post-gelation volumetric shrinkage as a function of crosslinking density at room temperature (inset).

4.4.3 Bulk Modulus

Figure 4.6 shows the predicted bulk modulus as a function of crosslinking density. A bulk modulus of $5.546 \pm 0.107\ GPa$ was predicted for the fully crosslinked system ($\phi = 0.95$). The bulk modulus gradually increases with crosslinking density, and as it reaches gelation at $\phi = 0.60$, the value approaches a constant value as the material transforms to a solid phase after gelation. Because it is difficult to measure K experimentally, MD predictions are an efficient means of determining this at varying

crosslinking densities. The MD data in **Figure 4.6** was fitted with a quadratic curve fit with $R^2 = 0.986$ showing a non-linear dependence between K and crosslinking density as defined by

$$K(GPa) = (-1.157 \times \phi^2) + (2.743 \times \phi) + 4.283 \tag{4.5}$$

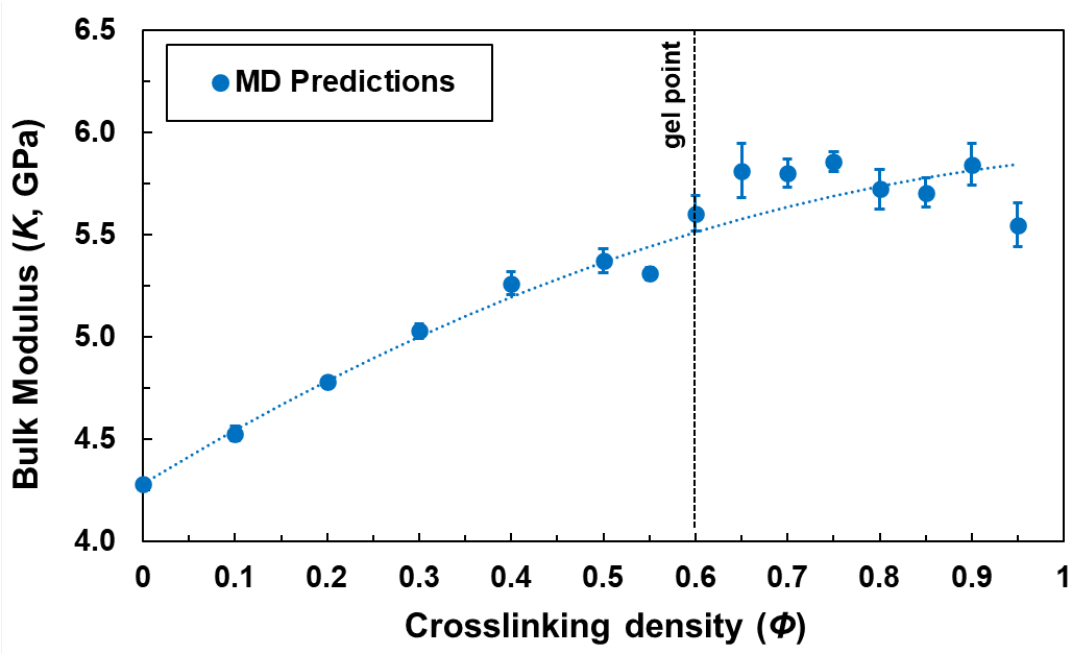

Figure 4.6: Predicted bulk modulus as a function of crosslinking density at room temperature.

4.4.4 Shear Modulus

Figure 4.7 shows the predicted shear modulus as a function of crosslinking density. A shear modulus of $1.222 \pm 0.267\ GPa$ was predicted for $\phi = 0.95$. This value is compared with the experimentally-measured values at three different strain rates from Littell et al. [147]. The variation between MD predictions and experimental measurements is due to the orders-of-magnitude difference in strain rates [80]. The shear modulus for the uncrosslinked epoxy is a finite value also because of the strain-rate effect [80]. Due to the unavailability of experimental data for intermediate crosslinking densities in the literature, the comparison with MD predictions was not made here for shear modulus, Young's modulus, Poisson's ratio, and yield strength. However, the comparison with the maximum crosslinking density ($\phi = 0.95$) qualitatively validates the predictions for all other values as the same procedure was followed to predict the properties for the entire range of crosslinking densities. The MD data in **Figure 4.7** was fitted with a linear curve fit with $R^2 = 0.984$ showing a linear dependence between G and crosslinking density as defined by

$$G(GPa) \;=\; (0.969 \times \phi) + 0.154 \tag{4.6}$$

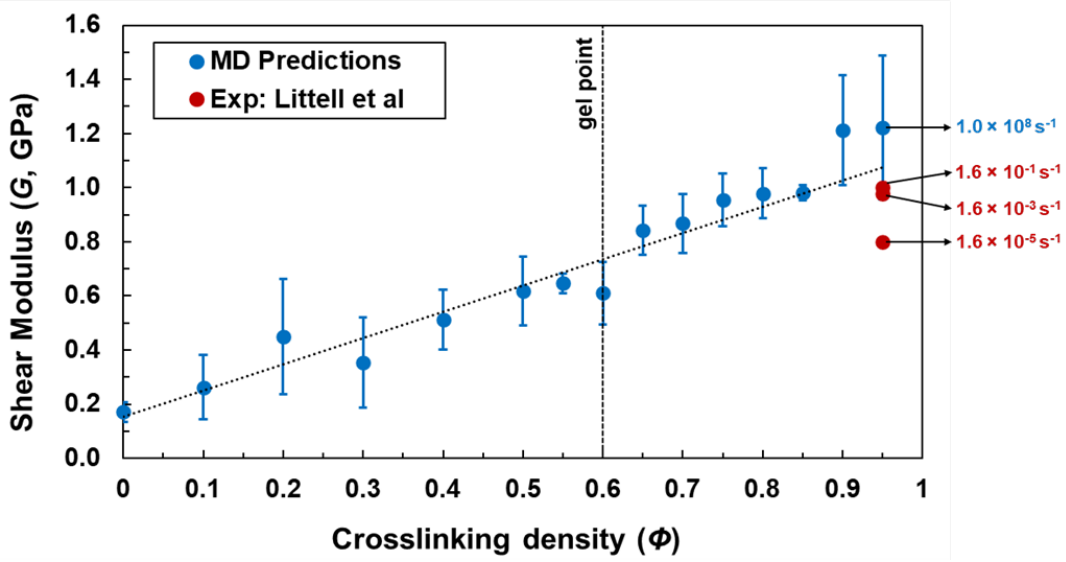

Figure 4.7: Predicted shear modulus as a function of crosslinking density at room temperature. Callouts refer to the corresponding strain rate.

4.4.5 Young's Modulus

Figure 4.8 shows the predicted Young's modulus as a function of crosslinking density. $E = 3.407 \pm 0.701\ GPa$ was predicted for $\phi = 0.95$. Also shown in the figure are experimentally-measured values at different strain rates [147, 151]. The experimentally-measured value of 2.230 GPa at $2.22\times10^{-4}\ s^{-1}$ strain rate in this work agrees well with the other experimental data from literature. Despite the strain rate difference between MD simulations and experiments, the predictions at $\phi = 0.95$ match well with the higher strain rate ($7\times10^{2}\ s^{-1}$) experimental data from the Split-Hopkinson Bar test of Gilat et al. [151] (results analyzed by Odegard et al. [175]). Overall, the Young's modulus gradually increases with increasing crosslinking density.

This gradual increase is due to the increased network connectivity, which makes the material stiffer and able to sustain load. No significant change in the magnitude can be seen in the predictions above $\phi = 0.70$, as the material attains gelation. The MD data in **Figure 4.8** was fitted with a linear curve fit with $R^2 = 0.985$ showing a linear dependence between E and crosslinking density as defined by

$$E(GPa) \;=\; (2.732 \times \phi) + 0.461 \tag{4.7}$$

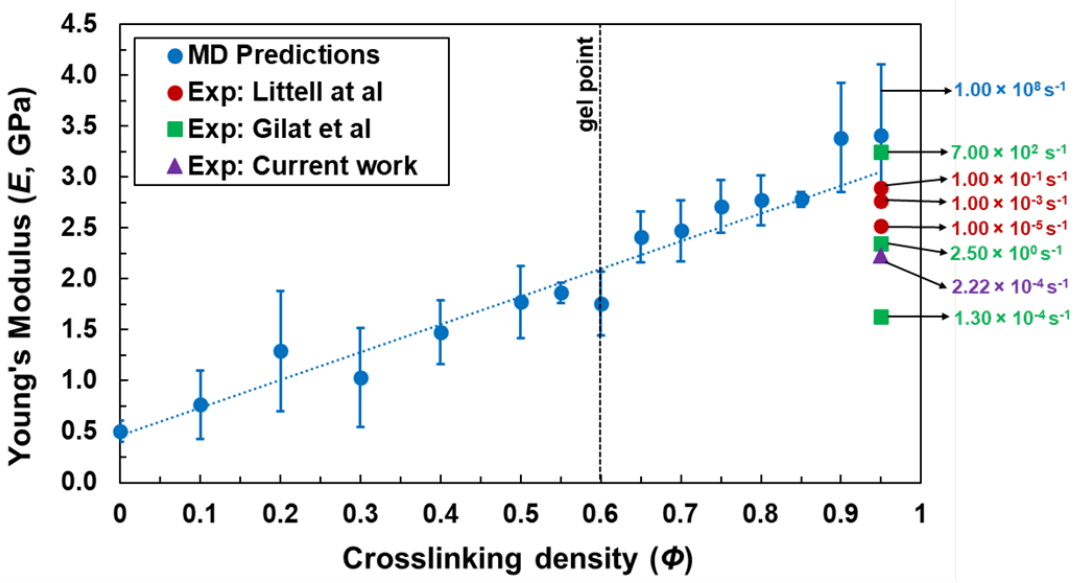

Figure 4.8: Predicted Young's modulus as a function of crosslinking density at room temperature. Callouts refer to the corresponding strain rate.

4.4.6 Poisson's ratio

Figure 4.9 shows the predicted Poisson's ratio as a function of crosslinking density. A Poisson's ratio of 0.398 ± 0.019 was predicted for $\phi = 0.95$ and 0.480 ± 0.004 was predicted for $\phi = 0$. Also shown in the **Figure 4.9** are the experimentally-measured values at different strain rates from Littell et al. [147]. The experimentally-measured value of 0.360 at a 2.22×10^{-4} s^{-1} strain-rate in this work agrees well with the data from the literature. The Poisson's ratio gradually decreases with increasing crosslinking density. The MD predictions at $\phi = 0.95$ agree well with the experimental values despite the difference in strain rates, which demonstrates a smaller influence of the strain rate on Poisson's ratio relative to Young's modulus and shear modulus. It can also be seen from **Figure 4.9** that the MD predicted Poisson's ratio for the fully crosslinked system agrees well with the experimental data from this work and the literature. The better agreement of the literature values suggests that there is a substantial amount of variability in the Poisson's ratio given different specimen preparation and testing techniques, and more measurement sampling could improve the agreement with the predictions. The MD data in **Figure 4.9** was fitted with a quadratic curve fit with $R^2 = 0.985$ showing a non-linear dependence between ν and crosslinking density as defined by

$$\nu = (-0.012 \times \phi^2) - (0.063 \times \phi) + 0.480 \tag{4.8}$$

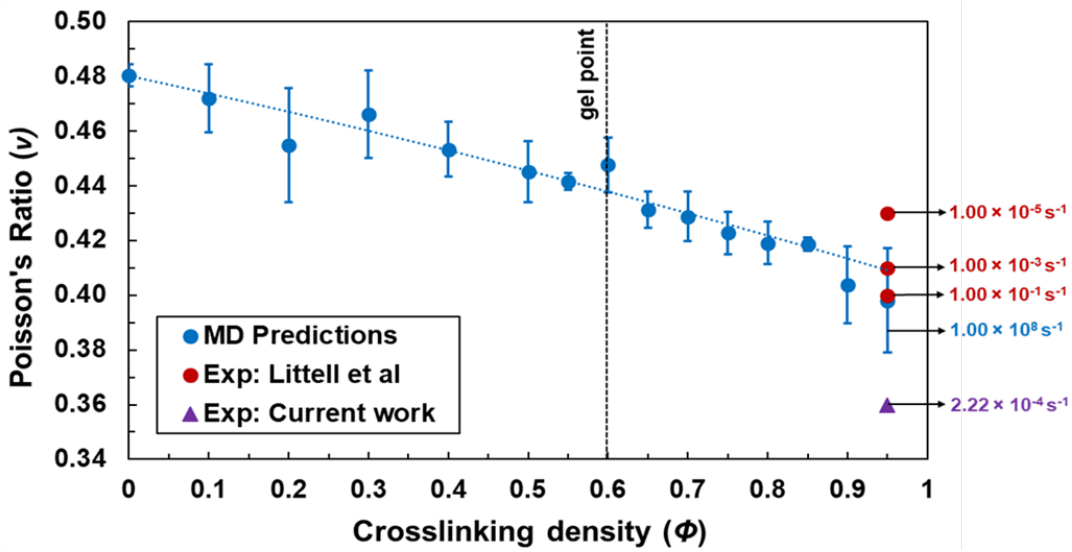

Figure 4.9: Predicted Poisson's ratio as a function of crosslinking density at room temperature. Callouts refer to the corresponding strain rate.

4.4.7 Yield strength

Figure 4.10 shows the predicted yield strength as a function of crosslinking density. A yield strength of 107.67 ± 16.67 MPa was predicted for $\phi = 0.95$. In the figure, this value is compared with experimentally-measured values at different strain rates [147, 151]. The experimentally-measured value of 36.54 MPa at a 2.22×10^{-4} s^{-1} strain rate in this work agrees well with the experimental data from the literature. It can also be seen in **Figure 4.10** that at $\phi = 0.95$ the yield strength increases

with increasing strain rate and the experimental value at the highest strain rate from Gilat et al. [151] (as analyzed by Odegard et al. [175]) matches well with the MD prediction. The yield strength increases with increasing crosslinking density due to increased network connectivity. In the pre-gelation regime ($\phi = 0$ to $\phi = 0.60$) the yield strength is low, as the material is a viscous liquid and cannot sustain large mechanical loads. The yield strength value increases quickly as the material reaches gelation ($\phi = 0.60$) and continues to increase in the post-gelation regime ($\phi = 0.60$ to $\phi = 0.95$) as the material attains a tighter network and can sustain significant loads. The MD data is fitted with a sigmoidal (Boltzmann equation) curve fit with $R^2 = 0.885$ which correctly represents the evolution of the yield strength of the epoxy from the un-crosslinked liquid phase to the fully crosslinked solid phase as defined by

$$\sigma\,(MPa) = \ 123.839 + (0.983 - 123.839) \times \left\{ \left[1 + e^{\left(\frac{\phi - 0.76}{0.1}\right)} \right]^{-1} \right\} \tag{4.9}$$

4.4.8 Coefficient of Thermal Expansion

Figure 4.11 shows the predicted coefficient of thermal expansion (CTE) below and above T_{g} as a function of crosslinking density at room temperature. The CTE agrees well with the experimental data [149] at full crosslinking density ($\phi = 0.95$) for both above and below T_{g}. Both the CTE predictions decreases linearly with increasing

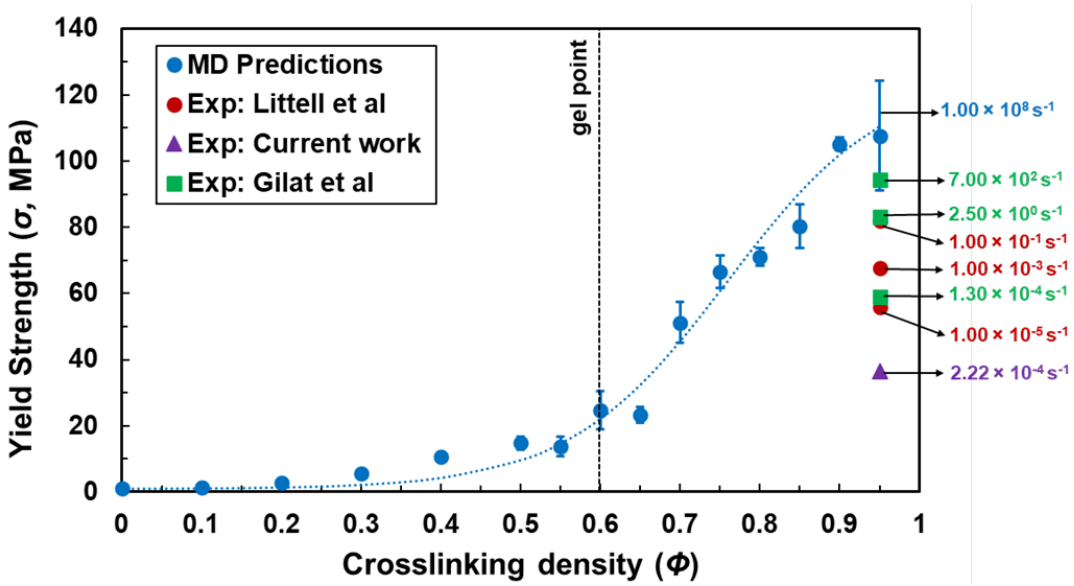

Figure 4.10: Predicted yield strength as a function of crosslinking density at room temperature. Callouts refer to the corresponding strain rate.

crosslinking density. This is likely because of the stiff network formation with increased number of covalent bonds as the crosslinking density increases. The fitting equations are shown as insets in the **Figure 4.11**.

4.4.9 Thermal Conductivity

Figure 4.12 shows the predicted thermal conductivity (λ) as a function of crosslinking density at room temperature. λ is predicted using two methods equilibrium molecular dynamics (EMD) [82] and non-equilibrium molecular dynamics methods (NEMD) [193]. The predictions at full crosslinking density ($\phi = 0.95$) using both

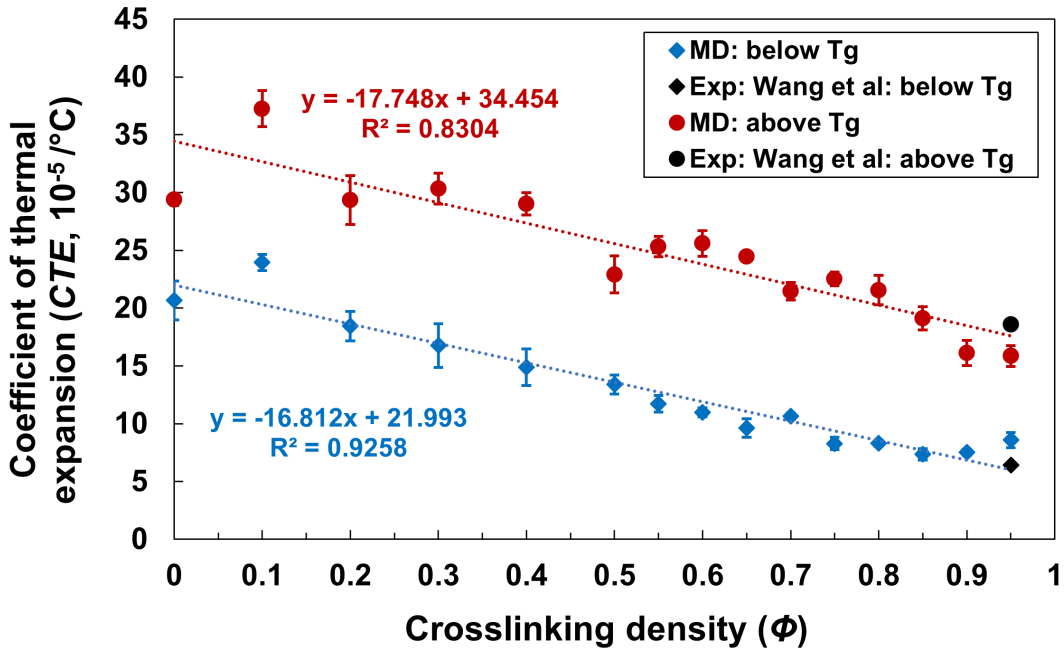

Figure 4.11: Predicted coefficient of thermal expansion (CTE) as a function of crosslinking density at room temperature.

methods falls within the experimental range [194]. λ decreases for EMD and increases for NEMD method as the crosslinking density increases. The standard error associated with the NEMD method is smaller than the EMD method. Both EMD and NEMD methods predicts same λ for higher crosslinking densities beyond gel point ($\phi = 0.6$) using IFF-R. But the trends in λ predicted using both methods differs for lower crosslinking densities. Varshney et al. [195] showed that λ was same for EMD and NEMD methods using CVFF force field at fully crosslinked state for same epoxy system.

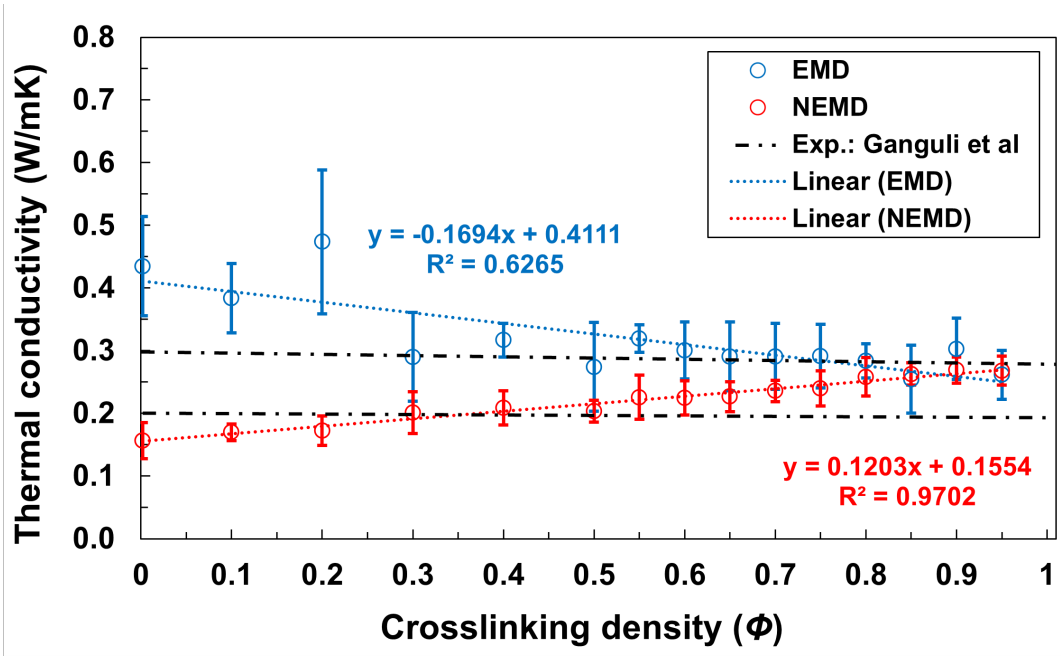

Figure 4.12: Predicted thermal conductivity (λ) as a function of crosslinking density at room temperature.

4.4.10 High temperature properties of DGEBF/DETDA epoxy

This sections describes the high temperature mechanical properties of the epoxy system. The properties are predicted at 177 $^{\circ}C$ as it is the prescribed processing temperature [191, 196]. **Figures 4.13** to **4.20** shows the room temperature and high temperature properties as a function of crosslinking density. Similar to earlier, the high temperature data sets are fitted with appropriate curve fits and the equations are shown in the figures.

4.4.10.1 Mass density and Volumetric shrinkage

Figures 4.13 and **4.14** shows the mass density and total chemical shrinkage as a function of crosslinking density. The increase in temperature causes the system to expand due to increased molecular motion. This causes the molecules to move apart from each other thus decreasing the mass density and increasing the volume of the simulation box. Both mass density and volume at high temperatures shows non-linear trends similar to room temperature data. Similar trend was observed in post-gelation volumetric shrinkage showing a linear trend in **Figure 4.15** The post-gelation volumetric shrinkage increases with increase in temperature due to the thermal expansion.

4.4.10.2 Bulk Modulus

Figure 4.16 shows the bulk modulus as a function of crosslinking density. The bulk modulus decreases with increase in temperature and shows a sigmoidal trend.

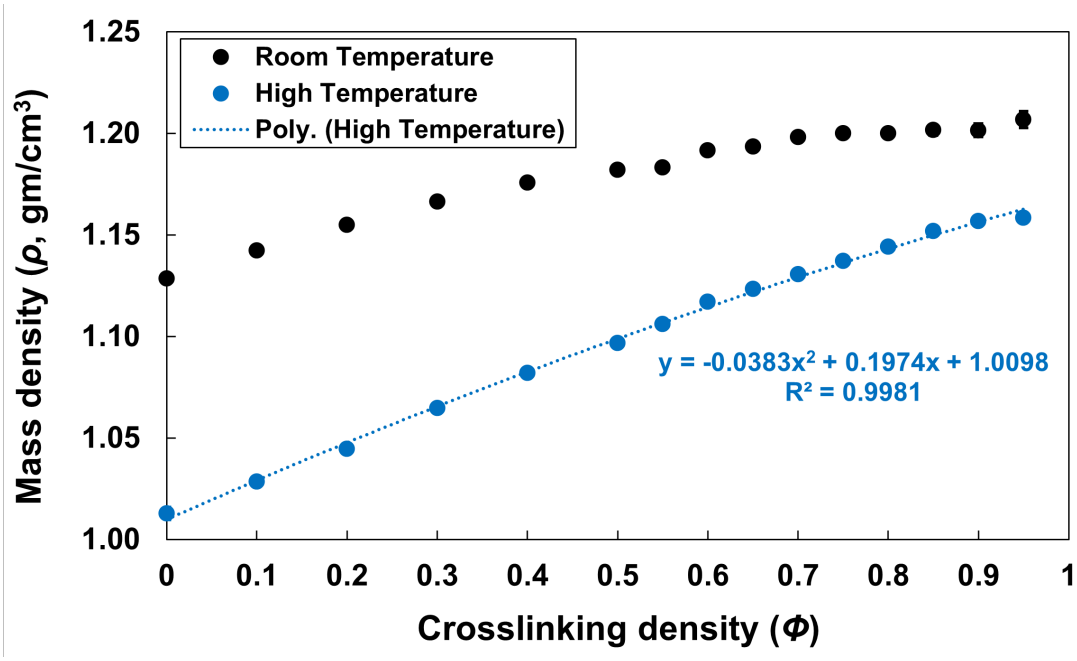

Figure 4.13: Predicted mass density as a function of crosslinking density at room and high temperature. The error bars for both data set are smaller than their respective symbols (black and blue solid circles)

4.4.10.3 Shear Modulus, Young's Modulus and Poisson's ratio

Figures 4.17, **4.18** and **4.19** shows the shear modulus, Young's modulus and Poisson's ratio respectively as a function of crosslinking density. The figures include the data only for post-gelation regime as the material is liquid in the pre-gelation regime and unable to sustain any load specially at 177 $^{\circ}C$ which is higher than the T_g of the epoxy system. Both the moduli decreases with increase in temperature and shows a linear trend, similar to the room temperature data. This is because, with increase in temperature the interatomic distance between the atoms and molecules increases due to thermal motion that reduces the intermolecular forces between them causing the

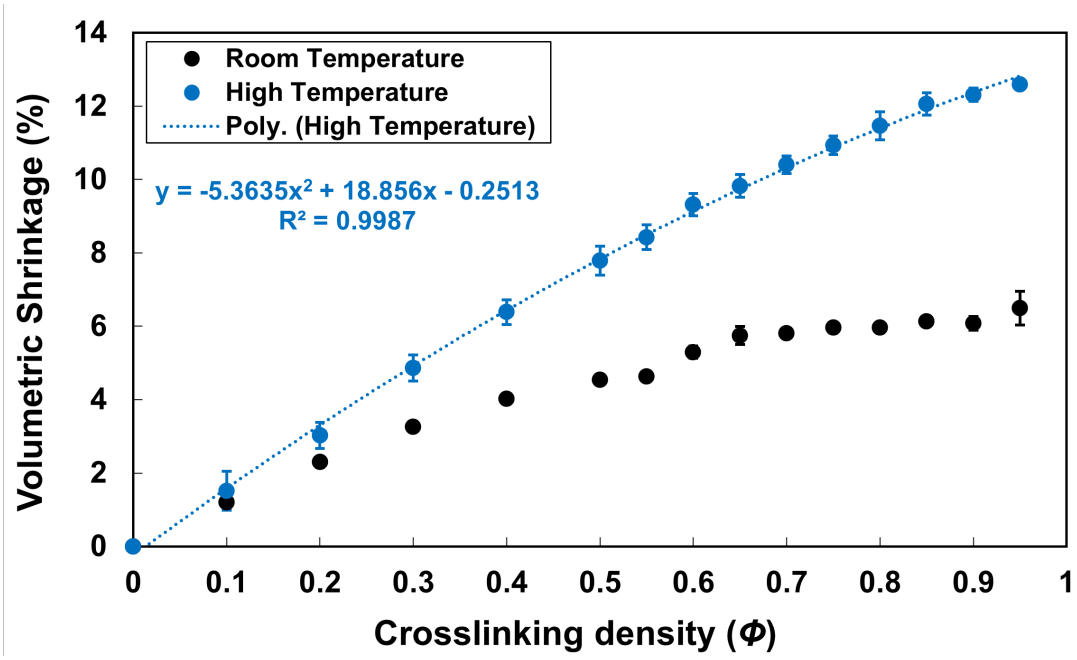

Figure 4.14: Predicted volumetric shrinkage as a function of crosslinking density at room and high temperature.

moduli to decrease. Also, the MD predictions of the moduli shows significant moduli values for in post-gelation regime as a result of the strain-rate effect. The moduli increases with increasing crosslinking because of the reasons explained above. The Poisson's ratio increases with increase in temperature and show the linear trend. The increase with temperature is again because of the thermal expansion.

4.4.10.4 Yield Strength

Figure 4.20 shows the yield strength as a function of crosslinking density. Again the figure include the data only for post-gelation regime. At high temperature the yield

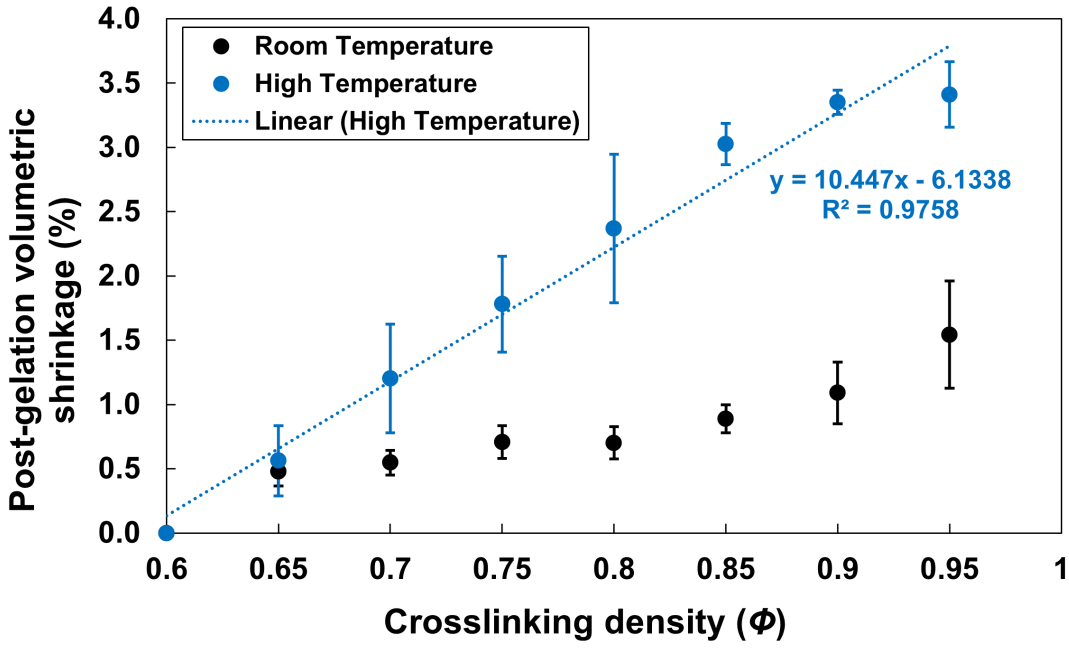

Figure 4.15: Predicted post-gelation volumetric shrinkage as a function of crosslinking density at room and high temperature.

strength decreases because of increased thermal motion and decreased intermolecular forces between the atoms and molecules. The high temperature data was fitted with a power law. The finite yield strength values in the post-gelation regime at high temperature is because of the strain-rate effect associated with the MD predictions [80].

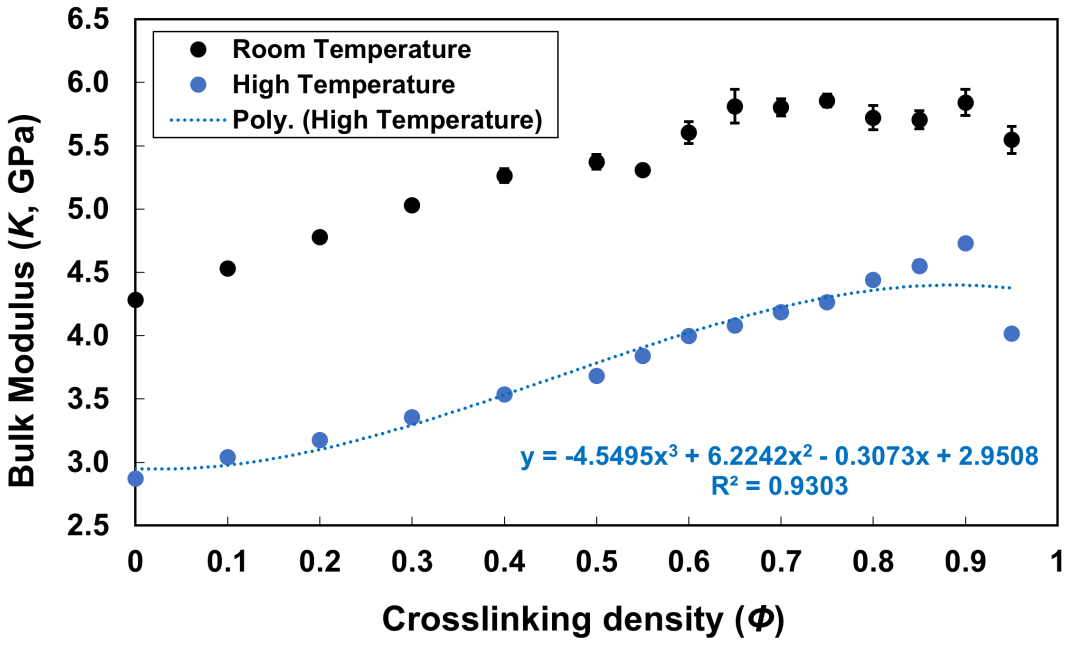

Figure 4.16: Predicted bulk modulus as a function of crosslinking density at room and high temperature. The error bars for high temperature data are smaller than the symbol (blue solid circles).

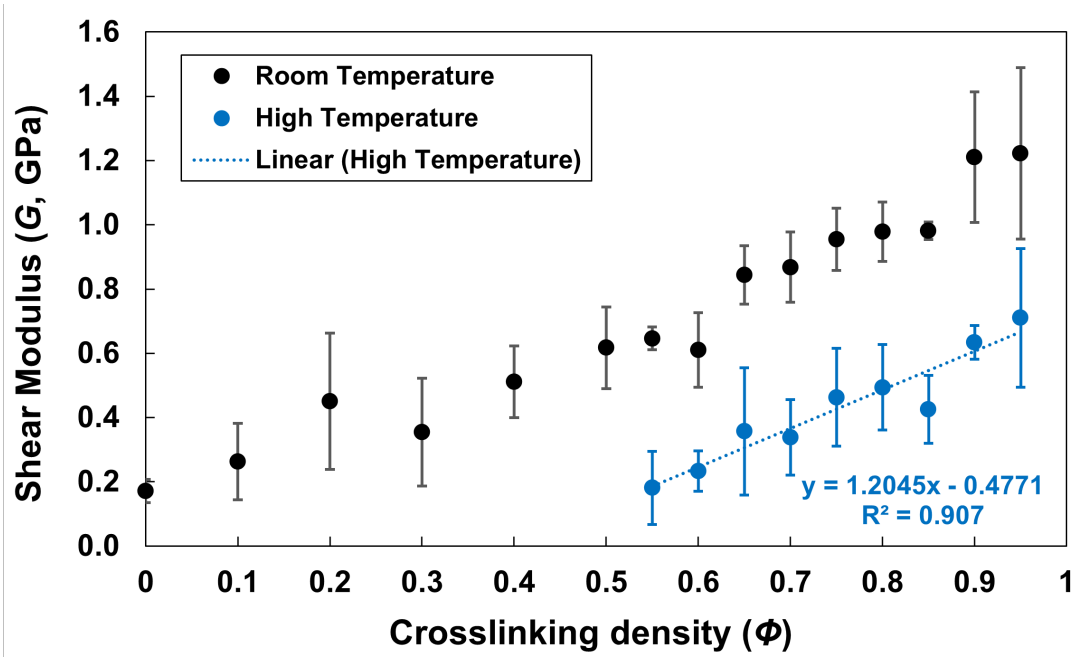

Figure 4.17: Predicted shear modulus as a function of crosslinking density at room and high temperature.

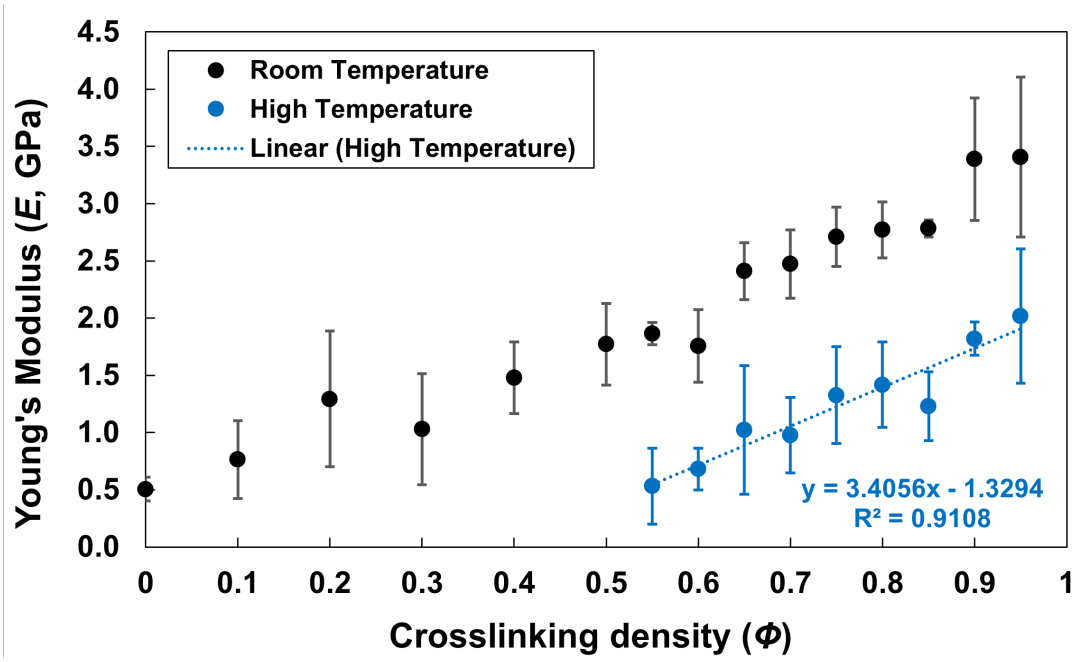

Figure 4.18: Predicted Young's modulus as a function of crosslinking density at room and high temperature.

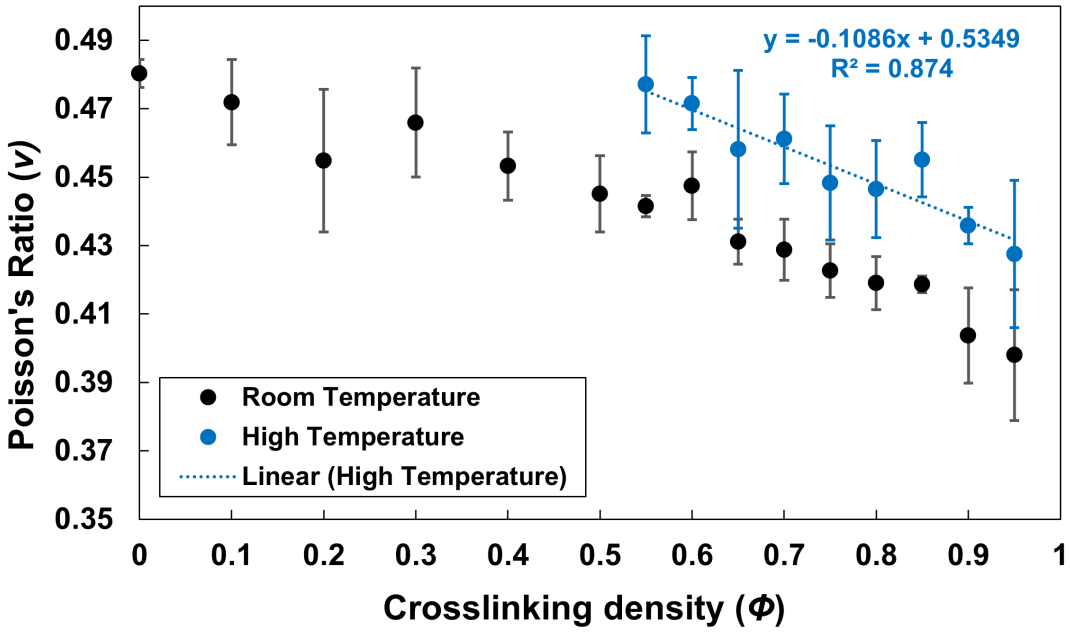

Figure 4.19: Predicted Poisson's ratio as a function of crosslinking density at room and high temperature.

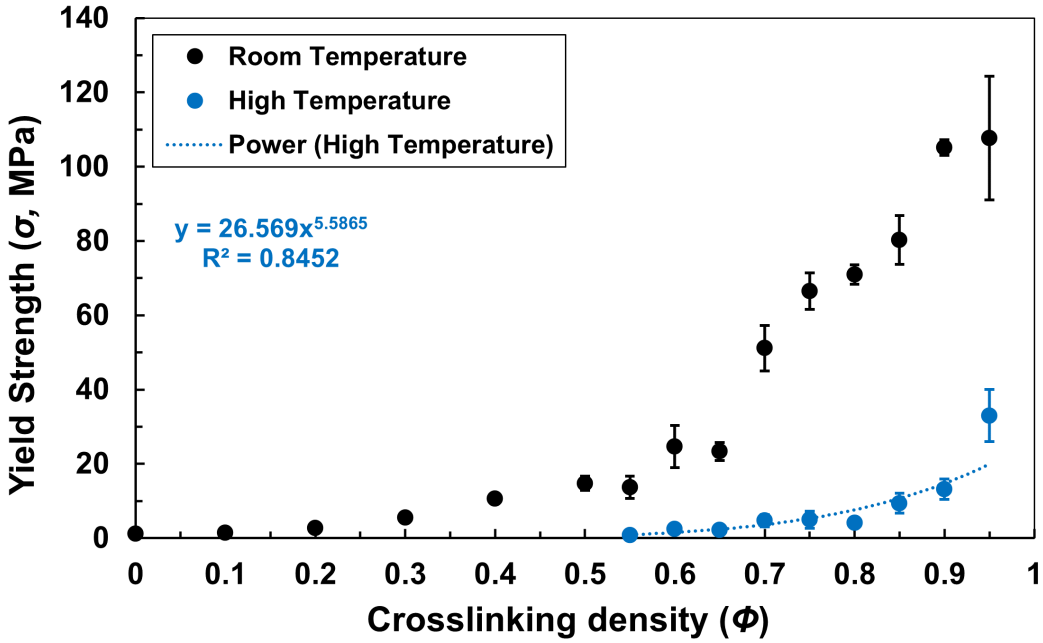

Figure 4.20: Predicted yield strength as a function of crosslinking density at room and high temperature.

4.5 Conclusions

The computational predictions from this study show that the epoxy mass density, volumetric shrinkage, stiffness, strength, and Poisson's ratio are strongly affected by the crosslink density. The predictions generally agree with the experimental measurements performed herein as well as those from the literature. Therefore, the computational simulation protocols are effective, and IFF-R is reliably predicting accurate physical and mechanical properties. The predicted properties at varying crosslinking densities provide insight into the evolution of properties of the epoxy system during the processing of composite materials. This data can be used as input into higher length-scale computational tools to predict the residual stresses that are developed during the processing of these complex networked epoxies in the presence of various composite reinforcements. Such modeling can be used to optimize processing parameters and improve composite laminate strength and reduce post-manufacturing residual deformations.

Chapter 5

Viscous Response Correction of Molecular Dynamics Mechanical Property Predictions

5.1 Introduction

Thermosetting polymer composites are extensively used in the aerospace industry because of their relatively low mass density and unique combination of mechanical, thermal, and electrical properties. Computationally-driven design of new generations of thermoset composites for improved performance requires multiscale modeling

techniques that are powerful and reliable. Such multiscale modeling must be able to incorporate molecular-scale structure for the prediction of bulk-level properties. In particular, molecular dynamics (MD) methods need to be developed that can efficiently predict accurate properties of thermoset neat resins as input into higher-length scale modeling techniques.

Thermoset neat resins consist of a complex network of covalently-linked molecular segments. Generally, for a given state of external conditions (e.g. temperature, mechanical deformation) these segments change their conformation to reach a state of lower energy (relaxation), which ultimately manifests itself as the phenomena known as physical aging and viscoelasticity [144]. These relaxation processes can occur over a wide range of time periods spanning nanoseconds to years, but a significant portion of them occur over timescales associated with composite laminate processing and laboratory mechanical testing. Although all-atom MD simulations have been used over the last several decades to predict molecular structure and nano-scale properties of thermoset resins [80, 81, 139–141, 153, 154, 162, 175, 182, 185, 197, 198], these simulations can only capture the thermoset network response over a nanosecond time scale, creating a significant discrepancy between simulated and laboratory timescales. Although coarse-grain simulation techniques [87–90, 199] can be used to somewhat avert the time scale limitation, some of the fine (and perhaps critically important) details of atomic interactions are lost during coarse-grain simulations.

Because of the timescale discrepancy between the conformational response on laboratory and MD-based timescales, all-atom MD predictions cannot precisely capture the relaxation processes that occur over time increments above nanoseconds. This shortcoming manifests itself in three major ways. First, MD predictions of fully crosslinked thermosets slightly overestimate the room-temperature elastic properties and yield strength [81, 175, 182]. This is commonly referred to as the "strain rate effect". Second, MD predictions of mechanical properties above the glass transition temperature (T_{g}) significantly overestimate experimental observations. This is evident when comparing experimentally-measured and MD-predicted properties of typical epoxies above the glass transition temperature. Whereas the measurements indicate a multiple order-of-magnitude drop in elastic modulus relative to room temperature [200], simulations predict only about a 50 % drop [200]. Third, MD predictions of partially-crosslinked epoxies indicate a steady increase in elastic modulus with respect to degree of cure [182], whereas experiments show a negligible modulus for all levels of crosslinking below the nearly fully-crosslinked state [182, 200]. These three manifestations of the viscous response have the same origin. During simulated mechanical deformations, conformational relaxation processes are not given sufficient time to occur, and thus the associated energy relaxation does not occur, resulting in a stiffer apparent structural response of the network. That is, quantities such as shear modulus and Young's modulus are overpredicted relative to their experimentally-measured values. Decreases in the degree of cure and increases in temperature exaggerate this effect,

as they increase the viscous response of the material.

Multiple methods have been proposed to account for the predicted modulus discrepancy in fully crosslinked systems at room temperature [166, 201–204]. However, a convenient and comprehensive approach that accounts for the viscous response of thermosets in MD predictions of mechanical properties for various levels of temperature and degree of cure has not been established. Such a method should have three minimum requirements. First, the method should involve minimal MD simulations. One approach to capturing the viscoelastic effect of polymers in MD predictions is to use a time-temperature superposition principle [197, 202–206]. Approaches like this require significant computational resources to fully characterize each polymer system considered. In a materials engineering environment where computational material design and process optimization need to be performed as efficiently as possible, a full characterization of the time-temperature superposition is not feasible and does not directly address the dependency of degree of cure on the viscous response. Second, the method should require minimal experimental input. Complete characterization of the material response as a function of strain rate, temperature, and degree of cure can be performed completely by experiment. However, such an approach is prohibitively time-consuming and expensive for most composite material development applications. Third, the method should directly address all three of the above-mentioned manifestations of the viscous response of thermosets.

In this work, a comprehensive approach satisfying all the above-mentioned criteria to establish a phenomenological viscous response correction factor is proposed for elastic and strength properties predicted with all-atom MD simulations. In addition, experimental characterization of thermal and mechanical properties of epoxy for different mixing ratios to efficiently emulate a range of degrees of cure [188] is performed to inform the correction. It is important to emphasize that this correction is phenomenological, and is designed to be parameterized by a convenient set of experiments to quickly correct MD predictions for rapid computationally-driven thermoset material design. It is not intended to be a comprehensive viscoelastic characterization of a resin via classical viscoelastic constitutive modeling [207, 208]. This article is organized as follows: First the methodology to establish the viscous response correction is introduced, followed by a description of the experimental methods used to characterize the correction. The parameterization and optimization of the correction is then described, and results of the modeling with the correction technique follow. The results show that the proposed approach effectively provides an accurate correction for MD predicted elastic properties of thermosets to capture the effects of strain rate, temperature, and degree of cure.

5.2 Viscous Correction

Using an approach inspired by the Buckingham π theorem [209], the viscous response can be expressed in terms of a minimal set of dimensionless parameters. It is first assumed that a laboratory-scale mechanical property (specifically, the Young's modulus for this description) can be related to its MD predicted value by

$$\frac{E}{E_{\mathrm{MD}}} = f\left(\dot{\varepsilon},\, \rho,\, T\right) \tag{5.1}$$

where $\dot{\varepsilon}$ is the strain rate, ϕ is the degree of cure, T is the temperature, E is the laboratory-scale Young's modulus, and E_{MD} is the all-atom MD-predicted Young's modulus in the fully crosslinked system at room temperature. The function f is thus limited to the range of $0 \leq f \leq 1$. The degree of cure is a dimensionless parameter valued between 0 (completely uncured) and 1 (fully cured).

Dimensionless parameters can now be introduced such that this formulation is independent of units and contains functions with direct proportionality with the dependent variable (modulus ratio). Specifically, the following dimensionless variables are defined:

$$\alpha \;=\; \frac{\dot{\varepsilon}}{\dot{\varepsilon}_{\mathrm{MD}}} \qquad\qquad \tau \;=\; 1 - \frac{T}{T_r} \tag{5.2}$$

where $\dot{\varepsilon}_{\mathrm{MD}}$ is the strain rate associated with MD time scales (for example, $1{\times}10^{8}$ s^{-1}); T_r is the reference temperature, which should be the highest temperature for which data is available, and herein will be assigned as the processing temperature of the thermoset resin; and T and T_r are expressed in degrees Kelvin. Thus, α and τ are dimensionless scalars that are valued between 0 and 1. **Equation 5.1** can be re-written in terms of the dimensionless parameters

$$\frac{E}{E_{\mathrm{MD}}} \;=\; f(\alpha, \phi, \tau) \tag{5.3}$$

For simplicity, **Equation 5.3** can be further specified using a separation-of-variables approach, where $f(\alpha,\phi,\tau)$ is re-written as a product of lower-dimension functions of the independent variables. If we choose the lower-dimension functions to represent the viscous response to strain rate (f_α), degree of cure (f_ϕ), and temperature (f_τ) then such a function could be represented as

$$\frac{E}{E_{\mathrm{MD}}} \;=\; f_\alpha(\alpha)\;\; f_\phi(\phi)\;\; f_\tau(\tau, \phi) \tag{5.4}$$

where each of the functions f_α, f_ϕ, and f_τ are directly proportional to their corresponding independent variables, and are valued between 0 and 1. Note that the function associated with temperature, f_τ is a function of both ϕ and τ because the temperature response of a thermoset is dependent both on temperature and degree of cure. The functional forms and parameters associated with functions in **Equation 5.4** are determined using data from the literature and experiments, as described below.

5.3 Material

The chosen material for the parameterization of **Equation 5.4** is an epoxy system consisting of a diglycidyl ether bisphenol F (DGEBF) epoxide monomer with a diethyltoluenediamine (DETDA) curing agent, as shown in **Figure 5.1**. These materials are commonly marketed as EPON 862 and EPIKURE W, respectively. This system was chosen because it is highly benchmarked and represents a baseline high-performance thermoset.

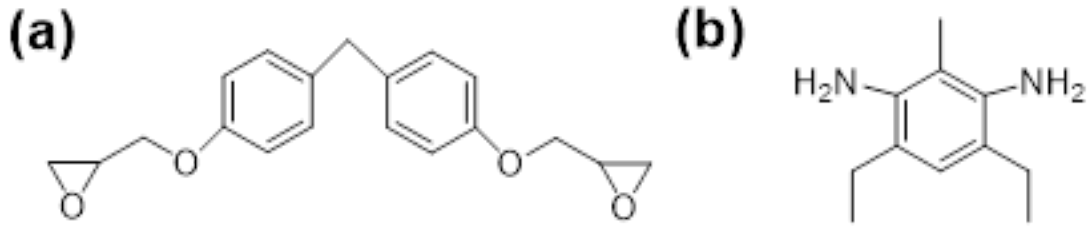

Figure 5.1: DGEBF/DETDA epoxy system molecular structure.

5.4 Experimental details

This section describes the details of the experiments performed to parameterize **Equation 5.4**. The experiments were performed on the DGEBF/DETDA epoxy system with a range of mixing ratios as proxies to various degrees of cure [188]. The use of these proxies was necessary because of the high level of difficulty of testing thermal properties of thermoset systems as a function of degree of cure. Although it is acknowledged that the use of off-stoichiometry systems is not a direct substitute for fully stoichiometric systems with intermediate degrees of cure, the proxies provide a reasonable substitute that is relatively easy to fabricate and test.

Epoxy samples were manufactured using a compression molding method. A total of two speedmixer cups were each charged with 50 g of DGEBF epoxy resin and an appropriate amount of DETDA curing agent to achieve systems with seven different mixing ratios of resin and hardener (**Table 5.1**). The mixing ratio is defined as the ratio of the mass of the actual DETDA hardener with respect to the mass of the DETDA hardener in the fully stoichiometric mixture. Speedmixer cups were mixed in a FlackTek Speedmixer (DAC 150.1 FVZ) at 2000 rpm for 5 $minutes$ at 25 $^{\circ}C$ and then heated to 90 $^{\circ}C$ in a vacuum oven. The speedmixer cups were degassed in the vacuum oven at 90 $^{\circ}C$ for 30 $minutes$ at 0.101 MPa vacuum pressure. The resin system was cast into a tooling assembly and compression molded at 121 $^{\circ}C$ for 2 $hours$

and then ramped to 177 $^{\circ}C$ and held for 2 $hours$. The compression molder was cooled using air and water until the system was cooled to 150 $^{\circ}C$ and then was switched to water cooling only to continue cooling the system to 25 $^{\circ}C$ before removing the plate. The tooling assembly produced 152.4 $\times$ 152.4 mm plates with 3.2 mm thickness.

Table 5.1
Mixing ratios for DGEBF/DETDA systems.

Mixing ratio (%)	**DGEBF** (g)	**DETDA** (g)
100	100	26.4
95	100	25.1
85	100	22.4
75	100	19.8
65	100	17.2
55	100	14.5
45	100	11.9

Dynamic mechanical analysis (DMA) was used to determine the thermo-mechanical response of the epoxy as a function of temperature and degree of cure. The testing was performed for all mixing ratios shown in **Table 5.1** to approximate the corresponding degrees of cure. The DMA specimens were cut from fabricated plates using a vertical bandsaw. Three specimens were tested for each mixing ratio. The specimens were 38.1 mm long, 12.7 mm wide, and 3.2 mm thick and the tests were performed using a TA Instruments Q800 DMA in single cantilever test mode with a constant frequency of 1 Hz, an amplitude of 25 μm, and a ramp rate of 3 $^{\circ}C/min$. The storage modulus, loss modulus, and tan delta values were continuously monitored during the temperature sweep. The storage modulus for all of the mixing ratios is shown in **Figure 5.2**a for

the whole range of temperatures. From this data, it is evident that the transition from glassy to rubbery states occurs at decreasing temperatures with decreasing levels of DETDA (thus degree of cure).

Figure 5.2b shows the storage modulus as a function of mixing ratio. It can be seen from the plot that the storage modulus gradually increases from the fully stoichiometric level with decreasing mixing ratios until 65 %. This is likely because of increasing levels of mass density of the proxy systems as DETDA monomers are removed. Fully stoichiometric systems with intermediate degrees of cure are not expected to exhibit this behavior, and this is the primary disadvantage of using proxy systems. However, as described below, this behavior did not affect the viscous response parameterization, and the advantages of using proxy systems for the purposes of this study far outweigh this disadvantage. In **Figure 5.2**b, it is also observed that as the mixing ratio decreases below 65 %, the storage modulus drastically decreases as the sparse network can no longer sustain significant mechanical loads.

The glass transition temperature (T_g) was determined using three different metrics: storage modulus, loss modulus and tan delta. To determine the T_g using storage modulus, the onset of the decline in storage modulus was located by finding the intersection between the baseline and the tangent at the point of the highest slope. The T_g values using the loss modulus and tan delta metrics were determined from the peak of the loss modulus/tan delta curve. **Figure 5.2**c shows the T_g values as a

function of mixing ratio using all three metrics. It is clear that the T_g trends are very similar with mixing ratio, with only a difference in the magnitude.

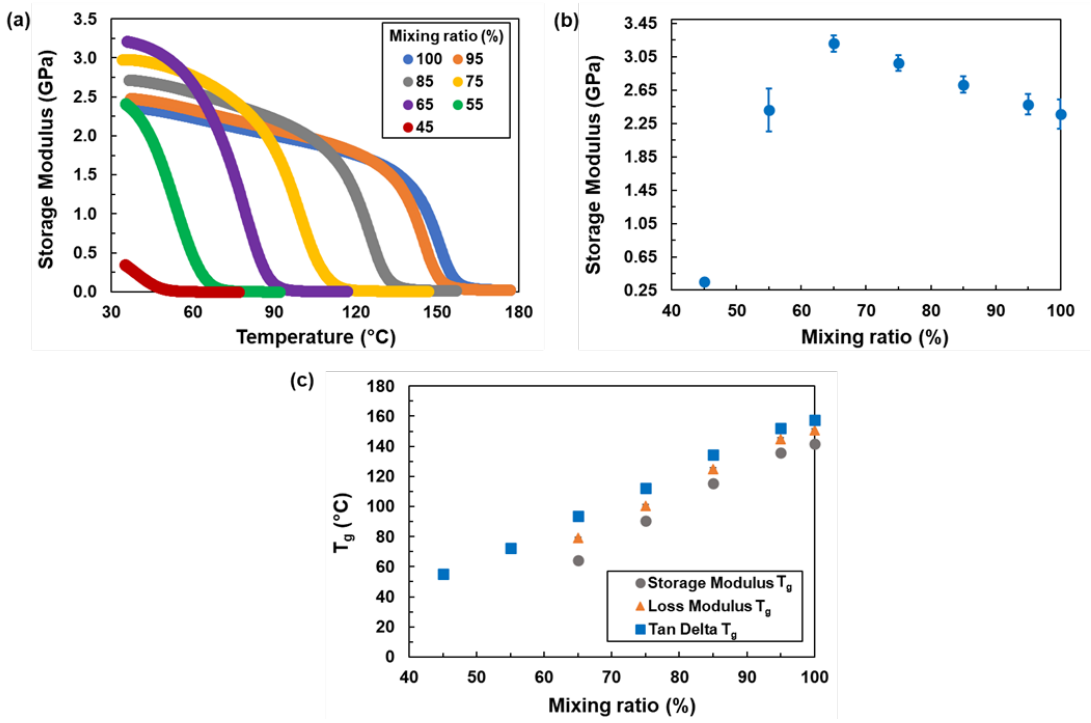

Figure 5.2: (a) Representative curves of storage modulus vs temperature, (b) Storage Modulus vs mixing ratio (n=3), (c) Tg vs mixing ratio (n=3, standard deviations are smaller than the symbols.

5.5 Viscous correction parameterization

The specific forms of functions in **Equation 5.4** and the corresponding phenomenological parameters for the DGEBF/DETDA system were determined as described in this section. First, the specific forms of the functions and the initial guesses of the parameters are outlined, followed by a description of the parameter optimization using

the Newton-Raphson [210] numeric technique.

5.5.1 Functional forms, parameters, and initial guesses

The functional form and parameters of $f_\alpha\,(\alpha)$ are described first. It has been demonstrated [80, 81, 175] that the DGEBF/DETDA system shows a logarithmic dependance of elastic modulus and yield strength on strain rate over a range of strain rates spanning experimental timescales ($10^{-5}\ s^{-1}$) to those associated with MD simulations ($10^{9}\ s^{-1}$) for fully crosslinked systems at room temperature. Therefore, $f_\alpha\,(\alpha)$ can be expressed as

$$f_\alpha\,(\alpha)\ =\ \alpha_a \ln(\alpha) + \alpha_b \tag{5.5}$$

where α_a and α_b are phenomenological parameters. These parameters can be determined by fitting experimental data of the Young's modulus normalized by the modulus predicted by MD (such that $0 \leq f_\alpha \leq 1$) as a function of α. **Figure 5.3** shows such a fit using several experimental data points from the literature [147, 151, 182, 191] with least-square fitting parameters $\alpha_a = 0.0147$ and $\alpha_b = 1.0849$.

As shown in **Figure 5.2**b the storage modulus exhibits a sigmoid-type response as a function of degree of cure. Thus, a logical choice for the $f_\phi\,(\phi)$ functional form

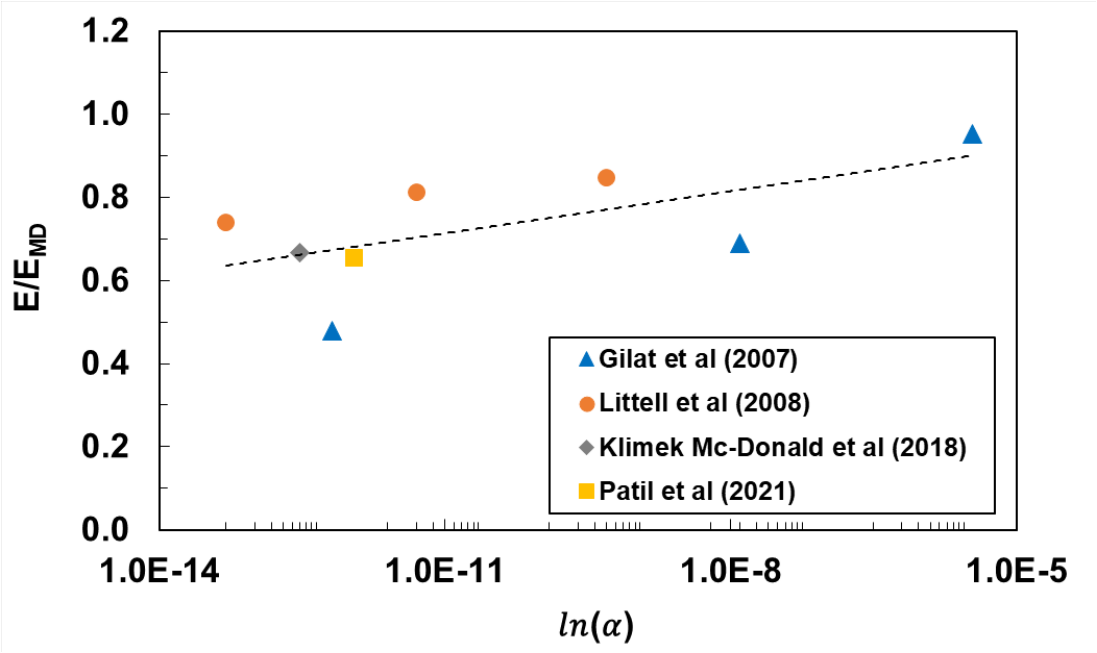

Figure 5.3: Normalized Young's modulus of DGEBF/DETDA epoxy as a function of applied normalized strain rate determined experimentally.

is a Fermi-Dirac function [211], whose value ranges between 0 and 1 and describes a continuous, yet step-like change from 0 to 1 centered at ϕ_0 with a step change intensity described by ϕ_σ:

$$f_\sigma(\sigma) = 1 - \left[1 + e^{\left(\frac{\phi-\phi_0}{\phi_\sigma}\right)}\right]^{-1} \tag{5.6}$$

Using the data shown in **Figure 5.2**b, values of ϕ_0 and ϕ_σ were determined by focusing the center of the sigmoid on the drop in modulus between degrees of cure of 45 % and 55 %. The corresponding values are $\phi_0 = 0.45$, $\phi_\sigma = 0.02$.

From the data shown in **Figure 5.2**a, it is clear that the modulus exhibits a sigmoid-type response with respect to temperature. Furthermore, it is evident that this temperature response is dependent on the degree of cure of the thermoset. Therefore, a functional form of $f_\tau\ (\tau, \phi)$ that captures this dependance is

$$f_\tau\,(\tau,\phi)\ =\ \left[1-\left[1+e^{(\frac{\tau-\tau_0(\phi)}{\tau_\sigma})}\right]^{-1}\right]\tau_*\,(\tau) \tag{5.7}$$

where $\tau_0(\phi)$ corresponds to the center of the sigmoidal-type response associated with the glass transition, which is dependent on ϕ; τ_σ describes the step change intensity of the transition; and $\tau_*(\tau)$ describes the change in the mechanical properties with temperature under the T_g. The value of τ_0 can be described with

$$\tau_0\,(\phi)\ =\ {\tau_0}^a\ \phi+{\tau_0}^b \tag{5.8}$$

where τ_0^a and ${\tau_0}^b$ are phenomenological parameters. The value of τ_* is described by

$$\tau_*\,(\tau)\ =\ {\tau_*}^a\ \tau^{\left({\tau_*}^b\right)} \tag{5.9}$$

where τ_*^a and τ_*^b are phenomenological parameters. The parameters in **Equations**

5.6, **5.7**, and **5.8** were determined using the DMA data shown in **Figure 5.2**a. The same data is plotted in **Figure 5.4** versus τ for all mixing ratios. The parameters τ_0^a and τ_0^b were determined by locating the sigmoid centers of the data in **Figure 5.4** for the different degrees of cure and fitting those values to the linear function shown in **Equation 5.7**. The best-fit values were τ_0^a = -0.4712 and τ_0^b = 0.5268.

Close examination of **Figure 5.4** shows that the curves do not exactly exhibit a sigmoidal shape, that is, for higher values of τ beyond the center of the sigmoid, the storage modulus continues to increase by a steady amount (modulus is a function of temperature in the glassy regime). Therefore, the τ^* multiplier in **Equation 5.6** is used to correct the sigmoid for this discrepancy. From **Figure 5.4** it is also evident that the maximum value of the modulus for each degree of cure proxy follows the same trend observed in **Figure 5.2**b, that is, the maximum value is the greatest for $\phi = 65$ %. Once again, the maximum value of the modulus would be expected to occur at ϕ = 100 % if these curves were from epoxies with intermediate degrees of cure, instead of proxies. However, as explained above, the proxy systems were used to characterize **Equations 5.5-5.9** because of the convenience of obtaining modulus data for a range of degrees of cure and temperature using proxy systems. The values for τ_*^a and τ_*^b were determined by quantifying the discrepancy between the modulus values from the DMA data just above the sigmoidal jump and the modulus of the full stoichiometry system at room temperature. The relationship between these discrepancy values and their corresponding τ values were fit with the power law relationship of **Equation**

5.9. The corresponding phenomenological parameters are $\tau_*^a = 1.4$ and $\tau_*^b = 0.3$.

Finally, with the initial guess values of eight out of nine phenomenological parameters determined, the final parameter, τ_σ, which describes the relative steepness of the sigmoid jumps shown in **Figure 5.4**, was determined using a least-squares fit of **Equations 5.4-5.9** to the DMA data shown in **Figure 5.4**, with a value of $\tau_\sigma = 0.009$.

5.5.2 Optimization of parameters

After the initial guesses of all the parameters were determined, they were used in the Newton-Raphson optimization technique to determine the final optimized values of the full set of nine parameters. The optimized values are provided in **Table 5.2**. **Figure 5.4** shows the storage modulus calculated with **Equations 5.4-5.9** and the optimized values plotted against the τ parameter. It is important to note that the model predicts the room temperature modulus of each system to be equal to that of the full stoichiometry system. The model parameters were fit this way to offset the effect of using a series of proxy systems instead of fully stoichiometric systems at partial degrees of cure.

Table 5.2
Material parameters for the viscous correction

Phenomenological material parameter	**Optimized values (all values are dimensionless)**
α_a	0.0147
α_b	1.0849
ϕ_0	0.4737
ϕ_σ	0.0263
τ_0^a	-0.4739
τ_0^b	0.5290
τ_*^a	1.3129
τ_*^b	0.2375
τ_σ	0.0100

5.6 Application of correction to MD predictions

It is uncommon for all the crosslinking reactions that can occur in a thermoset network to actually occur because of steric hindrance constrains on the motion of the reactive groups [141, 212]. The degree of cure is defined as the relative amount of conversion that has occurred in a thermosetting polymer system, ranging from 0 (no crosslinking reactions have occurred) to 1.0 (100 % of all crosslinking reactions have occurred that can possibly occur given steric hindrance constraints). Conversely, the crosslink density, as defined above, indicates the relative number of crosslinking reactions that have occurred with respect to the total number of reactive groups that exist in the material. Therefore, it is typical for a crosslink density to never reach 100 %, but a degree of cure can always reach 100 % given a sufficiently long cure time. Because

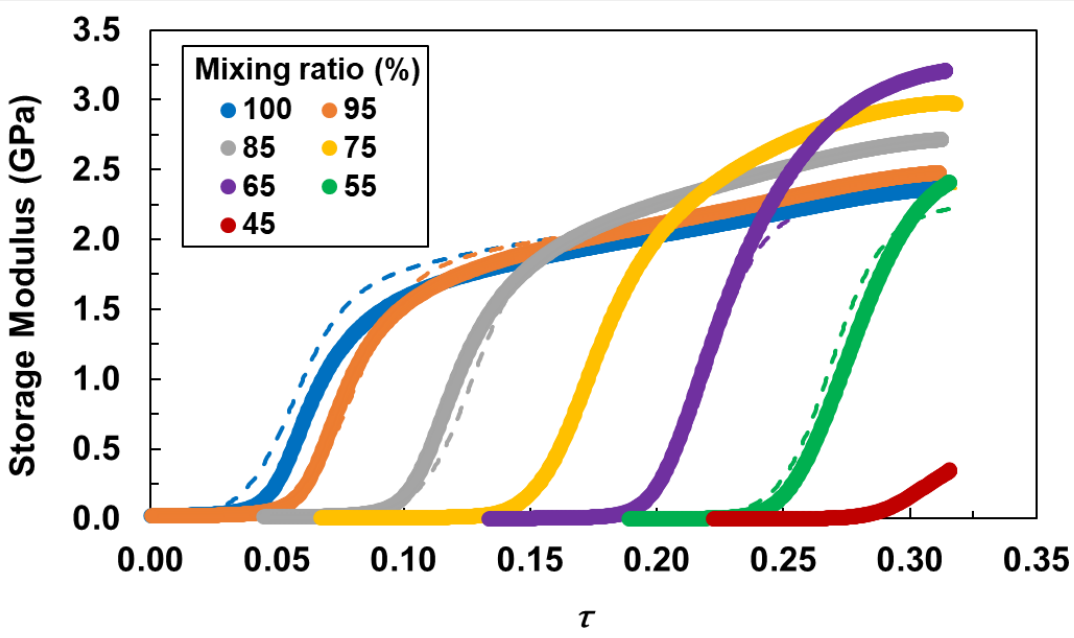

Figure 5.4: Plot of Storage Modulus vs τ. Solid lines are data from the DMA experiments, and dashed lines are from **Equations 5.4-5.9** with the optimized parameters from **Table 5.2**.

crosslink density is a convenient metric to track with MD, but degree of cure is more convenient from a processing perspective, it is necessary to convert the crosslink densities simulated with MD to degree of cure quantified experimentally. With these definitions, the degree of cure can be determined from the crosslink density as follows:

1. The degree of cure is 0 when the crosslink density is 0
2. The degree of cure is 1 when the crosslink density has reached its maximum value for a given material
3. Intermediate values of the degree of cure are calculated using a linear scaling such that the degree of cure is the ratio of the crosslink density to the maximum crosslink density

MD simulations were reported by Patil et al. [182] to predict the Young's modulus of the same DGEBF/DETDA epoxy system studied herein as a function of crosslinking density. In this study, after converting the data of Patil et al. [182] to be a function of degree of cure, the correction factor from **Equations 5.3-5.8** was applied using the optimized parameters shown in **Table 5.2**.

The viscous response of thermoset materials is only apparent in deformations with a finite deviatoric (shape changing) component of deformation. For hydrostatic (volume changing) deformations, the response is purely elastic [183]. Therefore, it is possible to predict the viscous response of the Poisson's ratio (ν) for the isotropic epoxy system as a function of degree of cure, temperature, and strain rate through the standard elasticity equation

$$\nu = \frac{3K - E}{6K} \tag{5.10}$$

Where K is the bulk modulus, which was predicted by Patil et al. [182] for this epoxy system as a function of crosslink density. Thus, the Poisson's ratio was determined for a range of degrees of cure at room temperature.

5.7 Results

Figure 5.5 shows the corrected and uncorrected predicted Young's modulus as a function of the degree of cure. Comparison of the corrected and uncorrected data shows that above the gel point of the DGEBF/DETDA system ($\phi = 0.63$) [182], the corrected and uncorrected modulus are relatively close, whereas below the gel point the corrected modulus drops quickly to zero, as expected [200]. Comparison of the corrected modulus to the experimental data shows excellent agreement for the fully crosslinked state and at $\phi = 0.45$. For the intermediate values of degree of cure, the predictions (both corrected and uncorrected) are substantially below the experimental data. This discrepancy, as explained above, is due to the use of proxy materials systems as a substitute for the full stoichiometry epoxy system with intermediate degrees of cure.

Figure 5.6 shows the corrected and uncorrected Poisson's ratio values as a function of degree of cure. From the figure it is evident that the two sets of values are very close over the entire range of the degree of cure. The MD predicted uncorrected and corrected Poisson's ratio values agree well with experimental data from literature [147, 182].

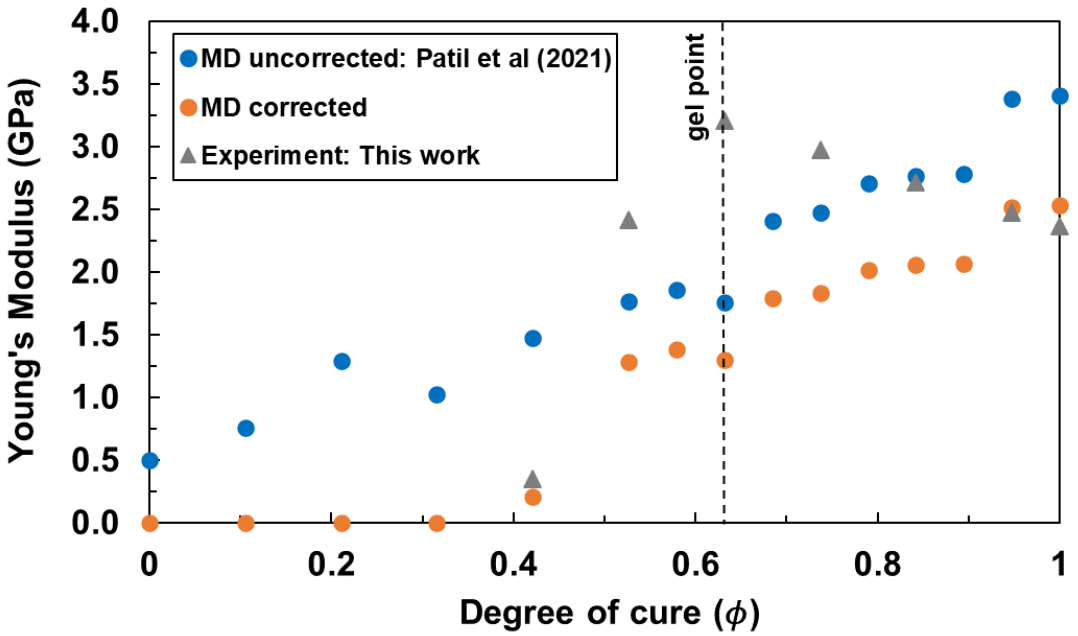

Figure 5.5: Plot of Young's modulus vs degree of cure including experimental data.

Figure 5.7 shows the corrected MD-predicted Young's modulus for varying temperatures compared with the room temperature MD uncorrected Young's modulus predictions. The Young's modulus decreases as the temperature increases. This is likely due to the increase in the intermolecular distance between atoms with increasing temperature which causes decrease in intermolecular forces and reduces the stiffness of the epoxy. Also, as the temperature approaches 177 $^{\circ}C$, which is the manufacturer-suggested cure temperature for the DGEBF/DETDA epoxy [191], the modulus reduces to nearly zero as the material is in the rubbery state and unable to carry any substantial load, even when fully crosslinked. The most striking feature of **Figure 5.7** is the significance of the viscous correction on the MD predicted modulus values. Not only does the corrected predictions agree with the experimental

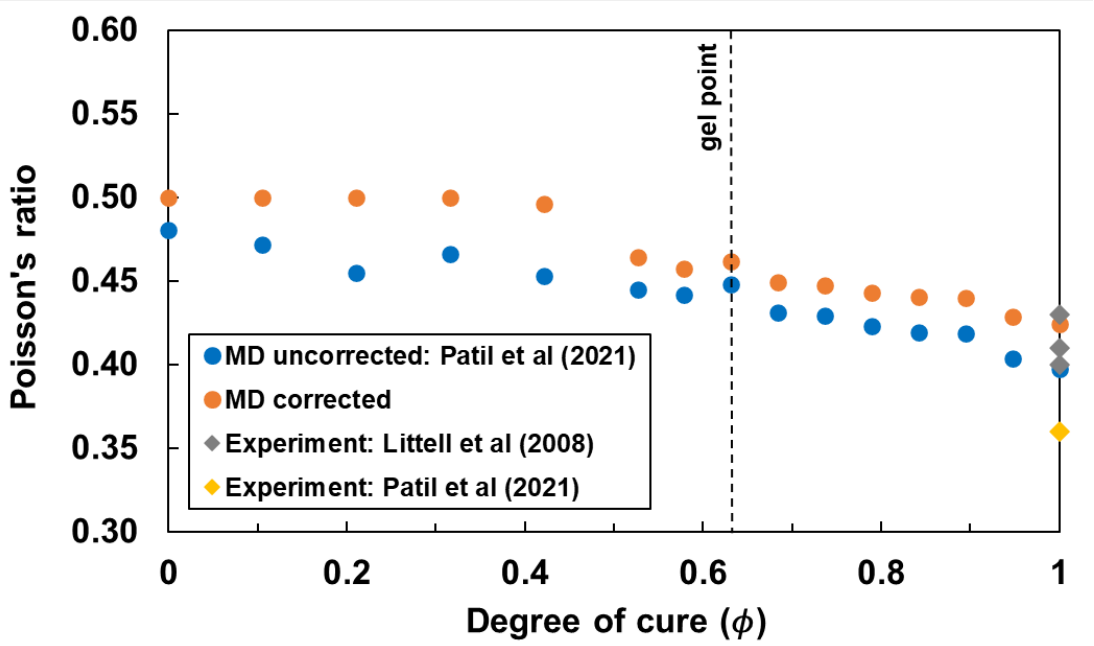

Figure 5.6: Plot of Poisson's ratio vs degree of cure including experimental data.

results (from herein as well as Littell et al. [147]), but the dramatic sigmoidal drop in the modulus for specific combinations of temperature and degree of cure is precisely captured with the correction.

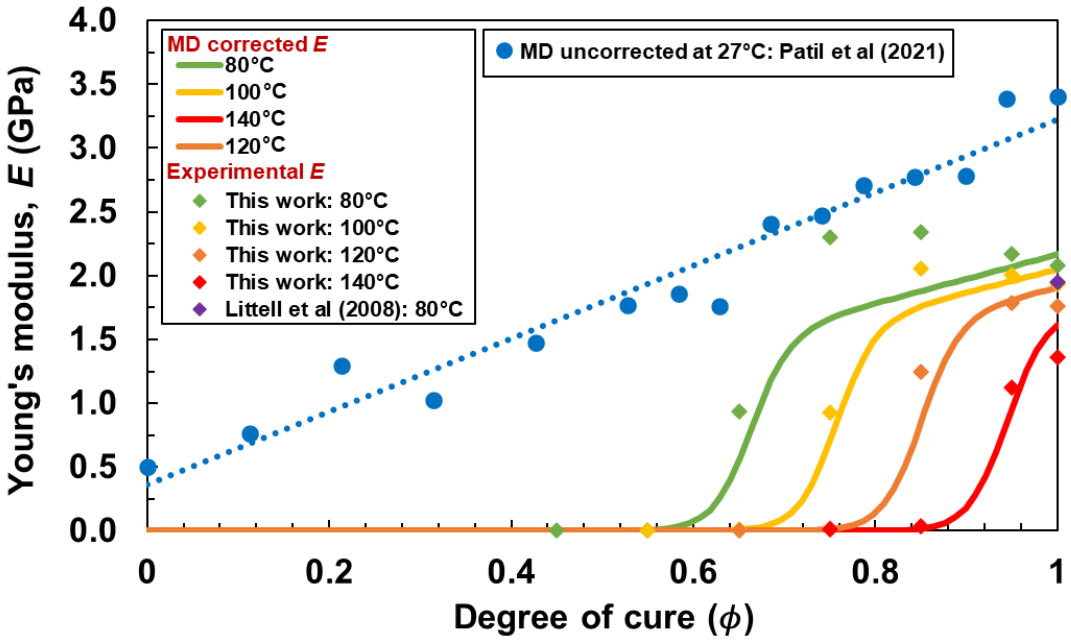

Figure 5.7: Plot of MD uncorrected (solid circles) and corrected (solid lines) Young's modulus vs degree of cure for varying temperature along with experimental data.

5.8 Conclusions

An efficient phenomenological-based correction factor has been developed for correcting MD-predicted elastic properties of thermosets that exhibit significant visco-elastic effects, such as the DGEBF/DETDA epoxy system studied herein. This approach satisfies the four requirements articulated at the beginning of this study. First, the method requires only minimal MD simulations. Only MD predictions of the mechanical properties of the polymer at multiple degrees of cure are needed, as opposed to an ambitious program of simulations to establish the time-temperature superposition relationship. Second, the method requires minimal experimental input. Only the storage modulus from DMA temperature sweep tests on off-stoichiometry specimens are required, and not the rigorous experimental characterization of the full viscoelastic constitutive response. Third, this approach directly addresses the well-known major issues associated with the inability of all-atom MD to fully simulate conformational relaxation processes at nanosecond timescales. Specifically, the over-estimation of mechanical properties at MD-scale strain rates, at temperatures above T_{g}, and at intermediate degrees of cure.

It is important to note that this approach is intended for efficient correction of MD-predicted properties of visco-elastic thermosets. This level of efficiency is particularly

beneficial for materials engineering environments where computational material design and process optimization need to be performed in a timely manner. This approach is not a direct substitute for comprehensive characterization of visco-elastic constitutive models or complete quantification of properties at intermediate degrees of cure. However, it does offer a simple approach to correct MD simulation data for the strain-rate effect and the overestimation of properties at elevated temperatures and intermediate degrees of cure.

Chapter 6

Conclusions

This chapter lists the overall conclusions from this work:

1. **Chapter 2** demonstrates that the flCNT based composites can be used to fabricate next-generation materials to construct space vehicles for deep space exploratory missions. The results show that the non-fluorinated polyimide has better interaction with the flCNT surface because of their alignment at the interface because of better π-π interaction. The fluorinated polyimide has better shear resistance or friction force because of the steric hindrance offered by the $-CF_3$ group. Transverse strength was nearly the same for both polyimides.
2. The results from **Chapter 2** along with interaction energy, friction force and transverse strength plots with polyimides, cyanate esters, PEEK, BMI, PBZ and

epoxy [79, 113, 114] are meant to serve as design charts to guide the selection of appropriate high-performance polymers to achieve desired properties in flCNT based polymer nanocomposites.

3. In **Chapter 3**, IFF-R force field was successfully validated with experimental data to predict thermo-mechanical properties of fully cured amorphous polymers. IFF-R was shown to be consistent, efficient and effective to model and predict properties of epoxies with different hardeners.
4. In **Chapter 4**, IFF-R force field was successfully utilized to predict the thermo-mechanical properties of DGEBF/DETDA epoxy as a function of crosslinking at room and high temperature. The properties at fully crosslinked state agrees well with the experimental measurements. These properties can be used as inputs in to the microscale analysis to predict the evolution of cure-induced residual stresses in composite laminates. This is an important step for process modeling of composites to determine optimum processing parameters to manufacture resins with improved properties and that can be tailored for specific applications.
5. In **Chapter 5**, a phenomenological viscous-response correction factor was developed to correct MD-predicted elastic properties of DGEBF/DETDA epoxy system. The method requires minimal MD simulation and experimental measurements to find all the parameters. In addition, this method can be easily adopted for any polymer. This method offer a simple approach to correct MD

simulation data for the strain-rate effect and the overestimation of properties at elevated temperatures and intermediate degrees of cure. This is necessary to integrate nanoscale and microscale for process modeling of composites to predict laminate strength.

This work demonstrates the effective use of molecular modeling to study the material behavior of high-performance polymers and their composites for deep space exploratory missions. In addition, the process modeling of fiber-reinforced epoxy composites to optimize processing parameters to reduce the overall time in designing and deploying these materials. This is critical for materials engineering environments where computational material design and process optimization need to be performed in a timely manner.

References

[1] Nakamura, J.; Wakunami, S.; Natori, A. *Physical Review B* **2005**, *72*(23).

[2] Downes, R. D.; Hao, A.; Park, J. G.; Su, Y.-F.; Liang, R.; Jensen, B. D.; Siochi, E. J.; Wise, K. E. *Carbon* **2015**, *93*, 953–966.

[3] Plimpton, S. *J. Comput. Phys.* **1995**, *117*, 1.

[4] Hinchliffe, A. *Molecular Modelling for Beginners;* Wiley, 2011.

[5] Odegard, G. M. *Comprehensive Composite Materials II* **2017**, page 28.

[6] Hospital, A.; Goñi, J. R.; Orozco, M.; Gelpí, J. L. *Adv Appl Bioinform Chem* **2015**, *8*, 37–47.

[7] Hollingsworth, S. A.; Dror, R. O. *Neuron* **2018**, *99*(6), 1129–1143.

[8] PhD thesis.

[9] PhD thesis.

[10] PhD thesis.

[11] PhD thesis.

[12] Heinz, H.; Lin, T.-J.; Kishore Mishra, R.; Emami, F. S. *Langmuir* **2013**, *29*, 1754.

[13] Winetrout, J. J.; Kanhaiya, K.; Sachdeva, G.; Pandey, R.; Damirchi, B.; van Duin, A.; Odegard, G. M.; Heinz, H. *arXiv/cond-mat.mtrl-sci* **2021**.

[14] National Aeronautics and Space Administration, 2015.

[15] Zhang, X.; Li, Q.; Holesinger, T. Arendt, P. Huang, J.; Kirven, P. Clapp, T. DePaula, R. Liao, X.; Zhao, Y.; Zheng, L.; Peterson, D. Zhu, Y. *Advanced Materials* **2007**, *19*(23), 4198–4201.

[16] Wang, Y.; Xu, H.; Drozdov, G.; Dumitrică, T. *Carbon* **2018**, *139*, 94–104.

[17] Ostanin, I.; Ballarini, R.; Potyondy, D.; Dumitrică, T. *Journal of the Mechanics and Physics of Solids* **2013**, *61*(3), 762–782.

[18] Chen, J.; Yan, L.; Song, W.; Xu, D. *Composites Part A: Applied Science and Manufacturing* **2018**, *114*, 149–169.

[19] Chandra, Y.; Scarpa, F.; Adhikari, S.; Zhang, J.; Flores, E. S.; Peng, H.-X. *Composites Part B: Engineering* **2016**, *102*, 1–8.

[20] Haghighatpanah, S.; Bolton, K. *Computational materials science* **2013**, *69*, 443–454.

[21] Xiong, Q. L.; Meguid, S. A. *European Polymer Journal* **2015**, *69*, 1–15.

[22] Yang, S.; Choi, J.; Cho, M. *Composite Structures* **2015**, *127*, 108–119.

[23] Alian, A. R.; Meguid, S. A. *Phys Chem Chem Phys* **2017**, *19*(6), 4426–4434.

[24] Sharifian, A.; Moshfegh, A.; Javadzadegan, A.; Hassanzadeh Afrouzi, H.; Baghani, M.; Baniassadi, M. *Phys Chem Chem Phys* **2019**, *21*(23), 12423–12433.

[25] Sharifian, A.; Baghani, M.; Wu, J.; Odegard, G. M.; Baniassadi, M. *The Journal of Physical Chemistry C* **2019**, *123*(5), 3226–3238.

[26] Frankland, S. J. V.; Caglar, A.; Brenner, D. W.; Griebel, M. *The Journal of Physical Chemistry B* **2002**, *106*(12), 3046–3048.

[27] Frankland, S. J. V.; Harik, V. M. *Surface Science* **2003**, *525*(1), L103–L108.

[28] Zheng, Q.; Xue, Q.; Yan, K.; Gao, X.; Li, Q.; Hao, L. *Polymer* **2008**, *49*(3), 800–808.

[29] Li, Y.; Liu, Y.; Peng, X.; Yan, C.; Liu, S.; Hu, N. *Computational Materials Science* **2011**, *50*(6), 1854–1860.

[30] Yang, L.; Tong, L.; He, X. *Computational Materials Science* **2012**, *55*, 356–364.

[31] Coto, B.; Antia, I.; Barriga, J.; Blanco, M.; Sarasua, J.-R. *Computational Materials Science* **2013**, *79*, 99–104.

[32] Sharma, K.; Sen Kaushalyayan, K.; Shukla, M. *Computational Materials Science* **2015**, *99*, 232–241.

[33] Peng, X.; Meguid, S. A. *Computational Materials Science* **2017**, *126*, 204–216.

[34] Chawla, R.; Sharma, S. *Composites Science and Technology* **2017**, *144*, 169–177.

[35] Qi-lin, X.; Xin, T. *Journal of Polymer Research* **2016**, *24*(1).

[36] Rahimian-Koloor, S. M.; Hashemianzadeh, S. M.; Shokrieh, M. M. *Physica B: Condensed Matter* **2018**, *540*, 16–25.

[37] Barber, A. H.; Cohen, S. R.; Wagner, H. D. *Applied Physics Letters* **2003**, *82*(23), 4140–4142.

[38] Tsuda, T.; Ogasawara, T.; Deng, F.; Takeda, N. *Composites Science and Technology* **2011**, *71*(10), 1295–1300.

[39] Cooper, C. A.; Cohen, S. R.; Barber, A. H.; Wagner, H. D. *Applied Physics Letters* **2002**, *81*(20), 3873–3875.

[40] Kolmogorov, A. N.; Crespi, V. H. *Physical Review Letters* **2000**, *85*(22), 4727–4730.

[41] Tangney, P.; Louie, S. G.; Cohen, M. L. *Phys Rev Lett* **2004**, *93*(6), 065503.

[42] Servantie, J.; Gaspard, P. *Physical Review B* **2006**, *73*(12).

[43] Filleter, T.; Yockel, S.; Naraghi, M.; Paci, J. T.; Compton, O. C.; Mayes, M. L.; Nguyen, S. T.; Schatz, G. C.; Espinosa, H. D. *Nano Lett* **2012**, *12*(2), 732–42.

[44] Xu, H.; Al-Ghalith, J.; Dumitrică, T. *Carbon* **2018**, *134*, 531–535.

[45] Xu, H.; Dumitrică, T. *Extreme Mechanics Letters* **2019**, *30*, 100508.

[46] Harrison, J. A.; White, C. T.; Colton, R. J.; Brenner, D. W. *Thin Solid Films* **1995**, *260*(2), 205–211.

[47] Perry, M. D.; Harrison, J. A. *Thin Solid Films* **1996**, *290-291*, 211–215.

[48] Harrison, J. A.; Stuart, S. J.; Perry, M. D. In *Tribology Issues and Opportunities in MEMS*, pages 285–299. Springer, 1998.

[49] Tutein, A. B.; Stuart, S. J.; Harrison, J. A. *Langmuir* **2000**, *16*(2), 291–296.

[50] Mikulski, P. T.; Harrison, J. A. *Journal of the American Chemical Society* **2001**, *123*(28), 6873–6881.

[51] Gao, G. T.; Mikulski, P. T.; Harrison, J. A. *Journal of the American Chemical Society* **2002**, *124*(24), 7202–7209.

[52] He, G.; Müser, M. H.; Robbins, M. O. *Science* **1999**, *284*(5420), 1650–1652.

[53] Barber, A. H.; Cohen, S. R.; Kenig, S.; Wagner, H. D. *Composites Science and Technology* **2004**, *64*(15), 2283–2289.

[54] Barber, A. H.; Cohen, S. R.; Eitan, A.; Schadler, L. S.; Wagner, H. D. *Advanced Materials* **2006**, *18*(1), 83–87.

[55] Manoharan, M. P.; Sharma, A.; Desai, A. V.; Haque, M. A.; Bakis, C. E.; Wang, K. W. *Nanotechnology* **2009**, *20*(29), 295701.

[56] Ganesan, Y.; Peng, C.; Lu, Y.; Loya, P. E.; Moloney, P.; Barrera, E.; Yakobson, B. I.; Tour, J. M.; Ballarini, R.; Lou, J. *ACS Appl Mater Interfaces* **2011**, *3*(2), 129–34.

[57] Chen, X.; Zheng, M.; Park, C.; Ke, C. *Small* **2013**, *9*(19), 3345–51.

[58] Chen, X.; Zhang, L.; Zheng, M.; Park, C.; Wang, X.; Ke, C. *Carbon* **2015**, *82*, 214–228.

[59] Awasthi, A. P.; Lagoudas, D. C.; Hammerand, D. C. *Modelling and Simulation in Materials Science and Engineering* **2009**, *17*(1).

[60] Li, Y.; Seidel, G. D. *Modelling and Simulation in Materials Science and Engineering* **2014**, *22*(2).

[61] Li, Y.; Seidel, G. D. *Computational Materials Science* **2018**, *153*, 363–381.

[62] Zhang, Y.; Zhuang, X.; Muthu, J.; Mabrouki, T.; Fontaine, M.; Gong, Y.; Rabczuk, T. *Composites Part B: Engineering* **2014**, *63*, 27–33.

[63] Li, M.; Zhou, H.; Zhang, Y.; Liao, Y.; Zhou, H. *RSC Adv.* **2017**, *7*(73), 46101–46108.

[64] Dharmawardhana, C. C.; Kanhaiya, K.; Lin, T.-J.; Garley, A.; Knecht, M. R.; Zhou, J.; Miao, J.; Heinz, H. *Molecular Simulation* **2017**, *43*(13-16), 1394–1405.

[65] Pramanik, C.; Gissinger, J. R.; Kumar, S.; Heinz, H. *ACS Nano* **2017**, *11*(12), 12805–12816.

[66] Damirchi, B.; Radue, M.; Kanhaiya, K.; Heinz, H.; Odegard, G. M.; van Duin, A. C. T. *J. Phys. Chem. C* **2020**, *124*, 20488.

[67] Pater, R. H.; Curto, P. A. *Acta Astronautica* **2007**, *61*(11-12), 1121–1129.

[68] Yokota, R. *Journal of Photopolymer Science and Technology* **1999**, *12*(2), 209–216.

[69] Ni, H.-j.; Liu, J.-g.; Wang, Z.-h.; Yang, S.-y. *Journal of Industrial and Engineering Chemistry* **2015**, *28*, 16–27.

[70] Pandiyan, S.; Brown, D.; van der Vegt, N. F. A.; Neyertz, S. *Journal of Polymer Science Part B: Polymer Physics* **2009**, *47*(12), 1166–1180.

[71] Odegard, G. M.; Clancy, T. C.; Gates, T. S. *Polymer* **2005**, *46*(2), 553–562.

[72] Clancy, T. C. *Polymer* **2004**, *45*(20), 7001–7010.

[73] Chakrabarty, A.; Cagin, T. *Polymer* **2010**, *51*(12), 2786–2794.

[74] Pinel, E.; Brown, D.; Bas, C.; Mercier, R.; Albérola, N. D.; Neyertz, S. *Macromolecules* **2002**, *35*(27), 10198–10209.

[75] Brillhart, M. V.; Cheng, Y.-Y.; Nagarkar, P.; Cebe, P. *Polymer* **1997**, *38*(12), 3059–3068.

[76] Heinz, H.; Suter, U. W. *The Journal of Physical Chemistry B* **2004**, *108*(47), 18341–18352.

[77] Sun, H. *The Journal of Physical Chemistry B* **1998**, *102*(38), 7338–7364.

[78] Stukowski, A. *Modelling and Simulation in Materials Science and Engineering* **2009**, *18*(1), 015012.

[79] Patil, S. U.; Radue, M. S.; Pisani, W. A.; Deshpande, P.; Xu, H.; Al Mahmud, H.; Dumitrică, T.; Odegard, G. M. *Computational Materials Science* **2020**, *185*, 109970.

[80] Odegard, G. M.; Jensen, B. D.; Gowtham, S.; Wu, J.; He, J.; Zhang, Z. *Chem. Phys. Lett.* **2014**, *591*, 175.

[81] Radue, M. S.; Jensen, B. D.; Gowtham, S.; Klimek-McDonald, D. R.; King, J. A.; Odegard, G. M. *J. Polym. Sci., Part B: Polym. Phys.* **2018**, *56*, 255.

[82] Chinkanjanarot, S.; Radue, M. S.; Gowtham, S.; Tomasi, J. M.; Klimek-McDonald, D. R.; King, J. A.; Odegard, G. M. *Journal of Applied Polymer Science* **2018**, *135*(25).

[83] Al Mahmud, H.; Radue, M. S.; Chinkanjanarot, S.; Pisani, W. A.; Gowtham, S.; Odegard, G. M. *Composites Part B: Engineering* **2019**, *172*, 628–635.

[84] Nosé, S. *Mol. Phys.* **1984**, *52*, 255.

[85] Nosé, S. *J. Chem. Phys.* **1984**, *81*, 511.

[86] Hoover, W. G. *Phys. Rev. A: At., Mol., Opt. Phys.* **1985**, *31*, 1695.

[87] Aramoon, A.; Breitzman, T. D.; Woodward, C.; El-Awady, J. A. *The Journal of Physical Chemistry B* **2016**, *120*(35), 9495–9505.

[88] Yang, S.; Cui, Z.; Qu, J. *The Journal of Physical Chemistry B* **2014**, *118*(6), 1660–1669.

[89] Langeloth, M.; Sugii, T.; Böhm, M. C.; Müller-Plathe, F. *The Journal of Chemical Physics* **2015**, *143*(24), 243158.

[90] Li, C.; Strachan, A. *Polymer* **2018**, *149*, 30–38.

[91] Gissinger, J. R.; Jensen, B. D.; Wise, K. E. *Polymer* **2017**, *128*, 211.

[92] Nexolve.

[93] SpecialChem.

[94] Kolmogorov, A. N.; Crespi, V. H. *Physical Review B* **2005**, *71*(23).

[95] Kohn, W.; Sham, L. J. *Physical Review* **1965**, *140*(4A), A1133–A1138.

[96] Perdew, J. P.; Zunger, A. *Physical Review B* **1981**, *23*(10), 5048–5079.

[97] Perdew, J. P.; Burke, K.; Ernzerhof, M. *Physical Review Letters* **1996**, *77*(18), 3865–3868.

[98] Cox, H. L. *British Journal of Applied Physics* **1952**, *3*, 72.

[99] Chen, Y.; Chia, J. Y. H.; Su, Z. C.; Tay, T. E.; Tan, V. B. C. *Polymer* **2013**, *54*(2), 766–773.

[100] Song, S.; Chen, Y.; Su, Z.; Quan, C.; Tan, V. B. C. *Composites Science and Technology* **2013**, *85*, 50–57.

[101] Pisani, W. A.; Radue, M. S.; Chinkanjanarot, S.; Bednarcyk, B. A.; Pineda, E. J.; Waters, K.; Pandey, R.; King, J. A.; Odegard, G. M. *Polymer* **2019**, *163*, 96.

[102] Yang, M.; Koutsos, V.; Zaiser, M. *The Journal of Physical Chemistry B* **2005**, *109*(20), 10009–10014.

[103] Lv, C.; Xue, Q.; Xia, D.; Ma, M.; Xie, J.; Chen, H. *The Journal of Physical Chemistry C* **2010**, *114*(14), 6588–6594.

[104] Liang, Y.-Y.; Xu, J.-Z.; Liu, X.-Y.; Zhong, G.-J.; Li, Z.-M. *Polymer* **2013**, *54*(23), 6479–6488.

[105] Castner, D. G.; Grainger, D. W. *Fluorinated surfaces, coatings, and films*, Vol. 787; ACS Publications, 2001.

[106] Gnecco, E.; Bennewitz, R.; Gyalog, T.; Loppacher, C.; Bammerlin, M.; Meyer, E.; Güntherodt, H. J. *Physical Review Letters* **2000**, *84*(6), 1172–1175.

[107] Popov, V. L.; others. *Contact mechanics and friction;* Springer, 2010.

[108] Fusco, C.; Fasolino, A. *Physical Review B* **2005**, *71*(4).

[109] Sang, Y.; Dube, M.; Grant, M. *Phys Rev Lett* **2001**, *87*(17), 174301.

[110] He, M.; Dong, J.; Zhang, K.; Ding, F.; Jiang, H.; Loiseau, A.; Lehtonen, J.; Kauppinen, E. I. *ACS Nano* **2014**, *8*(9), 9657–9663.

[111] Cumings, J.; Zettl, A. *Science* **2000**, *289*(5479), 602–604.

[112] Zhang, R.; Ning, Z.; Xu, Z.; Zhang, Y.; Xie, H.; Ding, F.; Chen, Q.; Zhang, Q.; Qian, W.; Cui, Y.; Wei, F. *Nano Lett* **2016**, *16*(2), 1367–74.

[113] Pisani, W. A.; Radue, M. S.; Patil, S. U.; Odegard, G. M. *Composites, Part B* **2021**, *211*, 108672.

[114] Deshpande, P. P.; Radue, M. S.; Gaikwad, P.; Bamane, S.; Patil, S. U.; Pisani, W. A.; Odegard, G. M. *Langmuir* **2021**, *37*(39), 11526–11534.

[115] MacKerell, A. D.; Brooks, B. R.; Brooks, C. L.; Nilsson, L.; Roux, B.; Won, Y.; Karplus, M.; Schleyer, P. V. R.; Allinger, N. L.; Clark, T.; Gasteiger, J.; Kollman, P. A.; Schaefer, H. F.; Schreiner, P. R. *Encyclopedia of Computational Chemistry*, Vol. 1; 1998.

[116] Cornell, W. D.; Cieplak, P.; Bayly, C. I.; Gould, I. R.; Merz, K. M.; Ferguson, D. M.; Spellmeyer, D. C.; Fox, T.; Caldwell, J. W.; Kollman, P. A. *J. Am. Chem. Soc.* **1995**, *117*, 5179.

[117] Mayo, S. L.; Olafson, B. D.; Goddard, W. A. *J. Phys. Chem. A* **1990**, *94*, 8897.

[118] Jorgensen, W. L.; Maxwell, D. S.; Tirado-Rives, J. *Journal of the American Chemical Society* **1996**, *118*(45), 11225–11236.

[119] Allinger, N. L. *J. Am. Chem. Soc.* **1977**, *99*, 8127.

[120] Maple, J. R.; Hwang, M. J.; Stockfisch, T. P.; Dinur, U.; Waldman, M.; Ewig, C. S.; Hagler, A. T. *J. Comput. Chem.* **1994**, *15*, 162.

[121] Halgren, T. A. *J. Comput. Chem.* **1996**, *17*, 490.

[122] van Duin, A. C. T.; Dasgupta, S.; Lorant, F.; Goddard, W. A. *The Journal of Physical Chemistry A* **2001**, *105*(41), 9396–9409.

[123] Liu, L. C.; Liu, Y.; Zybin, S. V.; Sun, H.; Goddard, W. A. *J. Phys. Chem. A* **2011**, *115*, 11016.

[124] Radue, M. S.; Odegard, G. M. *Composites Science and Technology* **2018**, *166*, 20–26.

[125] Sun, H.; Mumby, S. J.; Maple, J. R.; Hagler, A. T. *J. Am. Chem. Soc.* **1994**, *116*, 2978.

[126] Heinz, H.; Farmer, B. L.; Pandey, R. B.; Slocik, J. M.; Patnaik, S. S.; Pachter, R.; Naik, R. R. *J. Am. Chem. Soc.* **2009**, *131*, 9704.

[127] Patwardhan, S. V.; Emami, F. S.; Berry, R. J.; Jones, S. E.; Naik, R. R.; Deschaume, O.; Heinz, H.; Perry, C. C. *J. Am. Chem. Soc.* **2012**, *134*, 6244.

[128] Ramezani-Dakhel, H.; Ruan, L. Y.; Huang, Y.; Heinz, H. *Adv. Funct. Mater.* **2015**, *25*, 1374.

[129] Mishra, R. K.; Flatt, R. J.; Heinz, H. *J. Phys. Chem. C* **2013**, *117*, 10417.

[130] Heinz, H. *Clay Miner.* **2012**, *47*, 205.

[131] Muggeo, V. M. R. *Stat. Med.* **2003**, *22*, 3055.

[132] Tack, J. L.; Ford, D. M. *J. Mol. Graphics Modell.* **2008**, *26*, 1269.

[133] Malvern, L. E. *Introduction to the Mechanics of a Continuous Medium*, number Monograph; 1969.

[134] Park, H.; Kim, B.; Choi, J.; Cho, M. *Polymer* **2018**, *136*, 128.

[135] Jatin, n.; Sudarkodi, V.; Basu, S. *Int. J. Plast.* **2014**, *56*, 139.

[136] Hossain, D.; Tschopp, M. A.; Ward, D. K.; Bouvard, J. L.; Wang, P.; Horstemeyer, M. F. *Polymer* **2010**, *51*, 6071.

[137] Argon, A. S. *J. Macromol. Sci., Part B: Phys.* **1973**, *8*, 573.

[138] Argon, A. S. *Philos. Mag.* **1973**, *28*, 839.

[139] Li, C.; Strachan, A. *Polymer* **2011**, *52*, 2920.

[140] Li, C.; Strachan, A. *J. Polym. Sci., Part B: Polym. Phys.* **2015**, *53*, 103.

[141] Radue, M. S.; Varshney, V.; Baur, J. W.; Roy, A. K.; Odegard, G. M. *Macromolecules* **2018**, *51*(5), 1830–1840.

[142] Buchholz, J.; Paul, W.; Varnik, F.; Binder, K. *J. Chem. Phys.* **2002**, *117*, 7364.

[143] Vollmayr, K.; Kob, W.; Binder, K. *J. Chem. Phys.* **1996**, *105*, 4714.

[144] Odegard, G. M.; Bandyopadhyay, A. *Journal of Polymer Science Part B: Polymer Physics* **2011**, *49*(24), 1695–1716.

[145] Clarke, J. H. R.; Haward, R. N.; Young, R. J. *The Physics of Glassy Polymers;* 1997.

[146] Hutchinson, J. M.; Haward, R. N.; Young, R. J. *Physics of Glassy Polymers;* 1997.

[147] Littell, J. D.; Ruggeri, C. R.; Goldberg, R. K.; Roberts, G. D.; Arnold, W. A.; Binienda, W. K. *Journal of Aerospace Engineering* **2008**, *21*, 162.

[148] Tucker, S. J. *Study of 3, 3'vs. 4, 4'DDS isomer curatives on physical properties and phenyl ring motions of DGEBA epoxy via molecular dynamics, deuterium NMR, and dielectric spectroscopy;* The University of Southern Mississippi, 2010.

[149] Wang, S. R.; Liang, Z. Y.; Gonnet, P.; Liao, Y. H.; Wang, B.; Zhang, C. *Adv. Funct. Mater.* **2007**, *17*, 87.

[150] Li, C. Y.; Medvedev, G. A.; Lee, E. W.; Kim, J.; Caruthers, J. M.; Strachan, A. *Polymer* **2012**, *53*, 4222.

[151] Gilat, A.; Goldberg, R. K.; Roberts, G. D. *Journal of Aerospace Engineering* **2007**, *20*, 75.

[152] Bandyopadhyay, A.; Valavala, P. K.; Clancy, T. C.; Wise, K. E.; Odegard, G. M. *Polymer* **2011**, *52*, 2445.

[153] Kallivokas, S. V.; Sgouros, A. P.; Theodorou, D. N. *Soft Matter* **2019**, *15*, 721.

[154] Vashisth, A.; Ashraf, C.; Zhang, W.; Bakis, C. E.; van Duin, A. C. T. *J. Phys. Chem. A* **2018**, *122*, 6633.

[155] Zhang, W.; van Duin, A. C. T. *J. Phys. Chem. B* **2018**, *122*, 4083.

[156] Ferry, J. D. *Viscoelastic properties of polymers;* John Wiley & Sons, 1980.

[157] Jin, F.-L.; Li, X.; Park, S.-J. *J. Ind. Eng. Chem.* **2015**, *29*, 1.

[158] Brostow, W.; Goodman, S. H.; Wahrmund, J. In *Handbook of Thermoset Plastics (Third Edition)*; Dodiuk, H., Goodman, S. H., Eds.; William Andrew Publishing: Boston, third edition ed., 2014; pages 191–252.

[159] Gartner, T. E.; Jayaraman, A. *Macromolecules* **2019**, *52*, 755.

[160] Patil, S. U.; Radue, M. S.; Pisani, W. A.; Deshpande, P.; Xu, H.; Al Mahmud, H.; Dumitrica, T.; Odegard, G. M. *Comput. Mater. Sci.* **2020**, *185*, 109970.

[161] Hadden, C. M.; Jensen, B. D.; Bandyopadhyay, A.; Odegard, G. M.; Koo, A.; Liang, R. *Compos. Sci. Technol.* **2013**, *76*, 92.

[162] Varshney, V.; Patnaik, S. S.; Roy, A. K.; Farmer, B. L. *Macromolecules* **2008**, *41*, 6837.

[163] Sundararaghavan, V.; Kumar, A. *Int. J. Plast.* **2013**, *47*, 111.

[164] Li, C.; Strachan, A. *Polymer* **2010**, *51*, 6058.

[165] Li, C.; Strachan, A. *Polymer* **2015**, *75*, 151.

[166] Kravchenko, O. G.; Li, C.; Strachan, A.; Kravchenko, S. G.; Pipes, R. B. *Composites, Part A* **2014**, *66*, 35.

[167] Sun, Y.; Chen, L.; Cui, L.; Zhang, Y.; Du, X. *Comput. Mater. Sci.* **2018**, *143*, 240.

[168] Gou, J.; Fan, B.; Song, G.; Khan, A. *Int. J. Nanosci.* **2006**, *05*, 131.

[169] Shenogina, N. B.; Tsige, M.; Patnaik, S. S.; Mukhopadhyay, S. M. *Polymer* **2013**, *54*, 3370.

[170] Shenogina, N. B.; Tsige, M.; Patnaik, S. S.; Mukhopadhyay, S. M. *Macromolecules* **2012**, *45*, 5307.

[171] Jeyranpour, F.; Alahyarizadeh, G.; Arab, B. *J. Mol. Graphics Modell.* **2015**, *62*, 157.

[172] Lin, P.-H.; Khare, R. *Macromolecules* **2009**, *42*, 4319.

[173] Schichtel, J. J.; Chattopadhyay, A. *Comput. Mater. Sci.* **2020**, *174*, 109469.

[174] Pisani, W. A.; Wedgeworth, D. N.; Roth, M. R.; Newman, J. K.; Shukla, M. K. *J. Phys. Chem. C* **2021**, *125*, 15569.

[175] Odegard, G. M.; Patil, S. U.; Deshpande, P. P.; Kanhaiya, K.; Winetrout, J. J.; Heinz, H.; Shah, S. P.; Maiaru, M. *Macromolecules* **2021**, *54*(21), 9815–9824.

[176] Shah, S.; Patil, S.; Deshpande, P.; Kashmari, K.; Odegard, G.; Maiaru, M. In *In: ICCM22 2019. Melbourne, VIC: Engineers Australia, 2019: 2732-2740.;* Engineers Australia, 2019.

[177] Shah, S.; Patil, S.; Deshpande, P.; Krieg, A.; Kashmari, K.; Mahmud, H. A.; King, J.; Odegard, G. M.; Maiaru, M. *AIAA Scitech 2020 Forum* **2020**, page 1.

[178] Shah, S. P.; Maiarù, M. *Polymers* **2021**, *13*, 2491.

[179] Patil, S.; Shah, S.; DESHPANDE, P.; Kashmari, K.; ODEGARD, G.; Maiaru, M. In *Proceedings of the American Society for Composites—Thirty-fourth Technical Conference*, 2019.

[180] PATIL, S.; SHAH, S.; DESHPANDE, P.; KASHMARI, K.; OLAYA, M.; ODEGARD, G.; MAIARÙ, M. In *Proceedings of the American Society for Composites—Thirty-fifth Technical Conference*, 2020.

[181] Deshpande, P.; Shah, S.; Patil, S.; Kashmari, K.; OLAYA, M.; Odegard, G.; Maiaru, M. In *Proceedings of the American Society for Composites—Thirty-fifth Technical Conference*, 2020.

[182] Patil, S. U.; Shah, S. P.; Olaya, M.; Deshpande, P. P.; Maiaru, M.; Odegard, G. M. *ACS Applied Polymer Materials* **2021**, *3*(11), 5788–5797.

[183] Flory, P. J. *Principles of polymer chemistry;* Cornell university press, 1953.

[184] Yang, S.; Qu, J. *Polymer* **2012**, *53*, 4806.

[185] Estridge, C. E. *Polymer* **2018**, *141*, 12.

[186] Blaber, J.; Adair, B.; Antoniou, A. *Exp. Mech.* **2015**, *55*, 1105.

[187] Harilal, R.; others. **2014**.

[188] Olaya, M. N.; Odegard, G. M.; Maiaru, M. *AIAA Scitech 2021 Forum* **2021**, page 1.

[189] O'Brien, D. J.; White, S. R. *Polym. Eng. Sci.* **2003**, *43*, 863.

[190] Originpro. Corporation, O. **2021**.

[191] Klimek-McDonald, D. R.; King, J. A.; Miskioglu, I.; Pineda, E. J.; Odegard, G. M. *Polym. Compos.* **2018**, *39*, 1845.

[192] King, J. A.; Klimek, D. R.; Miskioglu, I.; Odegard, G. M. *J. Compos. Mater.* **2015**, *49*, 659.

[193] Wan, X.; Demir, B.; An, M.; Walsh, T. R.; Yang, N. *International Journal of Heat and Mass Transfer* **2021**, *180*, 121821.

[194] Ganguli, S.; Roy, A. K.; Anderson, D. P. *Carbon* **2008**, *46*(5), 806–817.

[195] Varshney, V.; Patnaik, S. S.; Roy, A. K.; Farmer, B. L. *Polymer* **2009**, *50*(14), 3378–3385.

[196] Klimek-McDonald, D. R. *MECHANICAL PROPERTIES OF GRAPHENE NANOPLATELET/EPOXY COMPOSITES* Dissertation, **2015**.

[197] Sirk, T. W.; Khare, K. S.; Karim, M.; Lenhart, J. L.; Andzelm, J. W.; McKenna, G. B.; Khare, R. *Polymer* **2013**, *54*(26), 7048–7057.

[198] Tsige, M.; Lorenz, C. D.; Stevens, M. J. *Macromolecules* **2004**, *37*(22), 8466–8472.

[199] Yang, S.; Qu, J. *Physical Review E* **2014**, *90*(1), 012601.

[200] Shah, S. P.; Patil, S. U.; Hansen, C. J.; Odegard, G. M.; Maiarù, M. *Mechanics of Advanced Materials and Structures* **2021**, pages 1–12.

[201] Park, H.; Choi, J.; Kim, B.; Yang, S.; Shin, H.; Cho, M. *Composites Part B: Engineering* **2018**, *142*, 131–141.

[202] Park, H.; Cho, M. *Journal of the Mechanics and Physics of Solids* **2020**, *142*, 103962.

[203] Park, C.; Jung, J.; Yun, G. J. *International Journal of Plasticity* **2020**, *129*, 102680.

[204] Park, C.; Jung, J.; Park, T.; Yun, G. In *AIAA Scitech 2020 Forum;* American Institute of Aeronautics and Astronautics, 2020; AIAA SciTech Forum.

[205] Khare, K. S.; Phelan Jr., F. R. *Macromolecular Theory and Simulations* **2020**, *29*(2), 1900032.

[206] Khare, K. S.; Phelan, F. R. *Macromolecules* **2018**, *51*(2), 564–575.

[207] Christensen, R. M., Ed. In *Theory of Viscoelasticity (Second Edition)*; Christensen, R. M., Ed.; Academic Press, 1982; pages 353–357.

[208] Findley, W. N., Lai, J. S., Onaran, K., Eds. In *North-Holland Series in Applied Mathematics and Mechanics*; Findley, W. N., Lai, J. S., Onaran, K., Eds.; North-Holland, 1976; Vol. 18; pages 268–288.

[209] Buckingham, E. Oct **1914**, *4*, 345–376.

[210] Galántai, A. *Journal of Computational and Applied Mathematics* **2000**, *124*(1), 25–44.

[211] In *Density Functional Theory;* 2009; pages 1–33.

[212] Hadden, C. M.; Klimek-McDonald, D. R.; Pineda, E. J.; King, J. A.; Reichanadter, A. M.; Miskioglu, I.; Gowtham, S.; Odegard, G. M. *Carbon* **2015**, *95*, 100–112.

[213] In *Density Functional Theory;* 2009; pages 193–208.

[214] In *Density Functional Theory;* 2009; pages 209–233.

[215] In *Density Functional Theory;* 2009; pages 131–161.

[216] In *Density Functional Theory;* 2009; pages 35–48.

[217] In *Density Functional Theory;* 2009; pages 83–112.

[218] In *Density Functional Theory;* 2009; pages 113–130.

[219] In *Density Functional Theory;* 2009; pages 179–192.

[220] In *Density Functional Theory;* 2009; pages 163–177.

[221] In *Density Functional Theory;* 2009; pages i–xii.

[222] In *Density Functional Theory;* 2009; pages 49–81.

[223] Abraham, A. C.; Edwards, C. R.; Odegard, G. M.; Donahue, T. L. *J Mech Behav Biomed Mater* **2011**, *4*(8), 2024–30.

[224] Abraham, A. C.; Moyer, J. T.; Villegas, D. F.; Odegard, G. M.; Haut Donahue, T. L. *J Biomech* **2011**, *44*(3), 413–8.

[225] Aifantis, K. E.; Shrivastava, S.; Odegard, G. M. *J Mater Sci Mater Med* **2011**, *22*(6), 1375–81.

[226] Alhabill, F. N.; Ayoob, R.; Andritsch, T.; Vaughan, A. S. *Journal of Materials Science* **2018**, *53*(6), 4144–4158.

[227] Asayesh-Ardakani, H.; Nie, A.; Marley, P. M.; Zhu, Y.; Phillips, P. J.; Singh, S.; Mashayek, F.; Sambandamurthy, G.; Low, K. B.; Klie, R. F.; Banerjee, S.; Odegard, G. M.; Shahbazian-Yassar, R. *Nano Lett* **2015**, *15*(11), 7179–88.

[228] Bandyopadhyay, A.; Odegard, G. M. *Modelling and Simulation in Materials Science and Engineering* **2012**, *20*(4).

[229] Bandyopadhyay, A.; Valavala, P. K.; Clancy, T. C.; Wise, K. E.; Odegard, G. M. *Polymer* **2011**, *52*(11), 2445–2452.

[230] Blaber, J.; Adair, B.; Antoniou, A. *Experimental Mechanics* **2015**, *55*(6), 1105–1122.

[231] Blanco, I.; Cicala, G.; Faro, C. L.; Motta, O.; Recca, G. *Polymer Engineering Science* **2006**, *46*(11), 1502–1511.

[232] Brostow, W.; Goodman, S. H.; Wahrmund, J. In *Handbook of Thermoset Plastics (Third Edition)*; Dodiuk, H., Goodman, S. H., Eds.; William Andrew Publishing: Boston, 2014; pages 191–252.

[233] Burton, B.; Alexander, D.; Klein, H.; Garibay-Vasquez, A.; Pekarik, A.; Henkee, C. *Epoxy Formulations Using Jeffamine Polyetheramines;* 2005.

[234] Calventus, Y.; Montserrat, S.; Hutchinson, J. M. *Polymer* **2001**, *42*(16), 7081–7093.

[235] Chen, C.; Justice, R. S.; Schaefer, D. W.; Baur, J. W. *Polymer* **2008**, *49*(17), 3805–3815.

[236] Chen, X.; Zheng, M.; Park, C.; Ke, C. *Small* **2013**, *9*(19), 3345–3351.

[237] Cheng, X.; Wu, Q.; Morgan, S. E.; Wiggins, J. S. *Journal of Applied Polymer Science* **2017**, *134*(18).

[238] Chenoweth, K.; van Duin, A. C. T.; Goddard, W. A. *The Journal of Physical Chemistry A* **2008**, *112*(5), 1040–1053.

[239] Coleman, J. N.; Khan, U.; Blau, W. J.; Gun'ko, Y. K. *Carbon* **2006**, *44*(9), 1624–1652.

[240] Deshpande, P. P.; Shah, S. P. P. S. K. K. O. G. M. M. M. In *Proceedings of the American Society for Composites—Thirty-fourth Technical Conference*.

[241] Dixon, S.; Jaques, D.; Edwards, C.; Palmer, S. B. *AIP Conference Proceedings* **2003**, *657*(1), 1049–1055.

[242] Du, J.; Bu, Y.; Shen, Z. *Construction and Building Materials* **2018**, *164*, 103–112.

[243] Elangovan, S.; Odegard, G. M.; Morrow, D. A.; Wang, H.; Hebert-Blouin, M. N.; Spinner, R. J. *Neurosurg Focus* **2009**, *26*(2), E11.

[244] Emami, F. S.; Puddu, V.; Berry, R. J.; Varshney, V.; Patwardhan, S. V.; Perry, C. C.; Heinz, H. *Chemistry of Materials* **2014**, *26*(8), 2647–2658.

[245] Estridge, C. E. *Polymer* **2018**, *141*, 12–20.

[246] Fan, H. B.; Yuen, M. M. F. *Polymer* **2007**, *48*(7), 2174–2178.

[247] Fernandez-Nograro, F.; Valea, A.; Llano-Ponte, R.; Mondragon, I. *European Polymer Journal* **1996**, *32*(2), 257–266.

[248] Ferry, J. D. *Viscoelastic Properties of Polymers;* 1980.

[249] Flory, P. J. *Principles of polymer chemistry;* Ithaca : Cornell University Press, 1953., 1953.

[250] Fu, Y.; Michopoulos, J.; Song, J.-H. *Computational Materials Science* **2015**, *107*, 24–32.

[251] Fu, Y.; Michopoulos, J. G.; Song, J.-H. *Nanoscale and Microscale Thermophysical Engineering* **2017**, *21*(1), 8–25.

[252] Gaikwad, P. S.; Krieg, A. S.; Deshpande, P. P.; Patil, S. U.; King, J. A.; Maiaru, M.; Odegard, G. M. *ACS Applied Polymer Materials* **2021**, *3*(12), 6407–6415.

[253] Gartner, T. E.; Jayaraman, A. *Macromolecules* **2019**, *52*(3), 755–786.

[254] Gartner, T. E.; Jayaraman, A. *Macromolecules* **2019**, *52*(3), 755–786.

[255] Gavrilov, A. A.; Komarov, P. V.; Khalatur, P. G. *Macromolecules* **2014**, *48*(1), 206–212.

[256] Gilat, A.; Goldberg, R. K.; Roberts, G. D. *Journal of Aerospace Engineering* **2007**, *20*(2), 75–89.

[257] Gilat, A.; Goldberg Robert, K.; Roberts Gary, D. *J. Aerosp. Eng.* **2007**, *20*, 75.

[258] Gissinger, J. R.; Jensen, B. D.; Wise, K. E. *Macromolecules* **2020**, *53*(22), 9953–9961.

[259] GOU, J.; FAN, B.; SONG, G.; KHAN, A. *International Journal of Nanoscience* **2006**, *05*(01), 131–144.

[260] Gou, J.; Minaie, B.; Wang, B.; Liang, Z.; Zhang, C. *Computational Materials Science* **2004**, *31*(3), 225–236.

[261] Gude, M. R.; Prolongo, S. G.; Ureña, A. *Journal of Thermal Analysis and Calorimetry* **2012**, *108*(2), 717–723.

[262] Gupta, V. B.; Brahatheeswaran, C. *Polymer* **1991**, *32*(10), 1875–1884.

[263] **2014**.

[264] Hasegawa, M.; Nishidate, K.; Yoshimoto, N. *Physical Review B* **2015**, *92*(24).

[265] Hauch, K. N.; Oyen, M. L.; Odegard, G. M.; Haut Donahue, T. L. *J Mech Behav Biomed Mater* **2009**, *2*(4), 339–47.

[266] Heinz, H.; Lin, T. J.; Mishra, R. K.; Emami, F. S. *Langmuir* **2013**, *29*(6), 1754–65.

[267] Jang, C. W.; Kang, J. H.; Palmieri, F. L.; Hudson, T. B.; Brandenburg, C. J.; Lawson, J. W. *ACS Applied Polymer Materials* **2021**.

[268] Jensen, B. D.; Bandyopadhyay, A.; Wise, K. E.; Odegard, G. M. *J Chem Theory Comput* **2012**, *8*(9), 3003–8.

[269] Jensen, B. D.; Odegard, G. M.; Kim, J. W.; Sauti, G.; Siochi, E. J.; Wise, K. E. *Compos Sci Technol* **2018**, *166*, 10–19.

[270] Jensen, B. D.; Wise, K. E.; Odegard, G. M. *J Comput Chem* **2015**, *36*(21), 1587–96.

[271] Jensen, B. D.; Wise, K. E.; Odegard, G. M. *J Phys Chem A* **2015**, *119*(37), 9710–21.

[272] Jensen, E. R.; Morrow, D. A.; Felmlee, J. P.; Odegard, G. M.; Kaufman, K. R. *J Biomech* **2015**, *48*(1), 95–103.

[273] Jeyranpour, F.; Alahyarizadeh, G.; Arab, B. *J Mol Graph Model* **2015**, *62*, 157–164.

[274] Jin, F.-L.; Li, X.; Park, S.-J. *Journal of Industrial and Engineering Chemistry* **2015**, *29*, 1–11.

[275] Jin, Y.; Duan, F.; Mu, X. *Applied Surface Science* **2016**, *387*, 1100–1109.

[276] Khairul Anuar, S.; Mariatti, M.; Azizan, A.; Chee Mang, N.; Tham, W. T. *J. Mater. Sci.: Mater. Electron.* **2011**, *22*, 757.

[277] Khoun, L.; Hubert, P. *Polymer Composites* **2010**, *31*(9), 1603–1610.

[278] King, J. A.; Klimek, D. R.; Miskioglu, I.; Odegard, G. M. *Journal of Composite Materials* **2015**, *49*(6), 659–668.

[279] Knorr, D. B.; Masser, K. A.; Elder, R. M.; Sirk, T. W.; Hindenlang, M. D.; Yu, J. H.; Richardson, A. D.; Boyd, S. E.; Spurgeon, W. A.; Lenhart, J. L. *Compos. Sci. Technol.* **2015**, *114*, 17.

[280] Kumar, A.; Li, S.; Roy, S.; King, J. A.; Odegard, G. M. *Composites Science and Technology* **2015**, *114*, 87–93.

[281] Lau, D.; Jian, W.; Yu, Z.; Hui, D. *Composites Part B: Engineering* **2018**, *143*, 282–291.

[282] Lee, A.; McKenna, G. B. *Polymer* **1988**, *29*, 1812.

[283] Levita, G.; De Petris, S.; Marchetti, A.; Lazzeri, A. *Journal of Materials Science* **1991**, *26*(9), 2348–2352.

[284] Li, C.; Strachan, A. *Polymer* **2010**, *51*(25), 6058–6070.

[285] Li, C.; Strachan, A. *Polymer* **2011**, *52*(13), 2920–2928.

[286] Li, C.; Strachan, A. *Polymer* **2015**, *75*, 151–160.

[287] Li, C.; Strachan, A. *Journal of Polymer Science Part B: Polymer Physics* **2015**, *53*(2), 103–122.

[288] Li, C.; Strachan, A. *Polymer* **2016**, *97*, 456–464.

[289] Liang, Z.; Gou, J.; Zhang, C.; Wang, B.; Kramer, L. *Materials Science and Engineering: A* **2004**, *365*(1), 228–234.

[290] Lin, P.-H.; Khare, R. *Macromolecules* **2009**, *42*(12), 4319–4327.

[291] Liu, A.; Wang, K. W.; Bakis, C. E. *Composites Part A: Applied Science and Manufacturing* **2011**, *42*(11), 1748–1755.

[292] Liu, Y. *Journal of Applied Polymer Science* **2013**, *127*(5), 3279–3292.

[293] Malvern, L. E. *Introduction to the Mechanics of a Continuous Medium;* 1969.

[294] Masoumi, S.; Arab, B.; Valipour, H. *Polymer* **2015**, *70*, 351–360.

[295] McAninch, I. M. *Molecular Toughening of Epoxy Networks;* 2014.

[296] McGrath, L. M.; Parnas, R. S.; King, S. H.; Schroeder, J. L.; Fischer, D. A.; Lenhart, J. L. *Polymer* **2008**, *49*, 999.

[297] Meyer, F.; Sanz, G.; Eceiza, A.; Mondragon, I.; Mijović, J. *Polymer* **1995**, *36*(7), 1407–1414.

[298] Miller, Sandi G. Roberts, G. D. C. C. C. B. J. L. K. L. W. B. W. K. Effects of hygrothermal cycling on the chemical, thermal, and mechanical properties of 862/w epoxy resin April 01, 2011 , **2011**.

[299] Miller-Stephenson.com. Product bulletin.

[300] Minty, R. F.; Yang, L.; Thomason, J. L. *Composites Part A: Applied Science and Manufacturing* **2018**, *112*, 64–70.

[301] Momma, K.; Izumi, F. *Journal of Applied Crystallography* **2011**, *44*(6), 1272–1276.

[302] Morgan, R. J.; Kong, F.-M.; Walkup, C. M. *Polymer* **1984**, *25*(3), 375–386.

[303] Morrow, D. A.; Donahue, T. H.; Odegard, G. M.; Kaufman, K. R. *Comput Methods Biomech Biomed Engin* **2010**, *13*(2), 247–56.

[304] Morrow, D. A.; Haut Donahue, T. L.; Odegard, G. M.; Kaufman, K. R. *J Mech Behav Biomed Mater* **2010**, *3*(1), 124–9.

[305] Morrow, D. A.; Odegard, G. M.; Kaufman, K. R. *Poromechanics V (2013)* **2013**, *2013*, 2174–2183.

[306] Mueller, J. E.; van Duin, A. C. T.; Goddard, W. A. *The Journal of Physical Chemistry C* **2010**, *114*(11), 4939–4949.

[307] Nawab, Y.; Casari, P.; Boyard, N.; Jacquemin, F. *Journal of Materials Science* **2013**, *48*(6), 2394–2403.

[308] Nouri, N.; Ziaei-Rad, S. *Macromolecules* **2011**, *44*(13), 5481–5489.

[309] Odagiri, N.; Shirasu, K.; Kawagoe, Y.; Kikugawa, G.; Oya, Y.; Kishimoto, N.; Ohuchi, F. S.; Okabe, T. *Journal of Applied Polymer Science* **2021**, *138*(23), 50542.

[310] Odegard, G. M.; Donahue, T. L.; Morrow, D. A.; Kaufman, K. R. *J Biomech Eng* **2008**, *130*(6), 061017.

[311] Okabe, T.; Oya, Y.; Tanabe, K.; Kikugawa, G.; Yoshioka, K. *European Polymer Journal* **2016**, *80*, 78–88.

[312] Okabe, T.; Takehara, T.; Inose, K.; Hirano, N.; Nishikawa, M.; Uehara, T. *Polymer* **2013**, *54*(17), 4660–4668.

[313] Okoro, C. U.; Hossain, M. K.; Hosur, M. V.; Jeelani, S. *Journal of Engineering Materials and Technology* **2011**, *133*(4).

[314] Olaya, M. N.; Odegard, G. M.; Maiaru, M. In *AIAA Scitech 2021 Forum*.

[315] OriginLab Corporation, Northampton, M. U.

[316] Park, H.; Kim, B.; Choi, J.; Cho, M. *Polymer* **2018**, *136*, 128–142.

[317] Park, J.; Jana, S. C. *Macromolecules* **2003**, *36*, 8391.

[318] Patil S. U., Shah, S. P. D. P. P. K. K. O. G. M. M. M. In *Proceedings of the American Society for Composites—Thirty-fourth Technical Conference*.

[319] Patil S. U., Shah, S. P. D. P. P. K. K. O. M. N. O. G. M. M. M. In *Proceedings of the American Society for Composites—Thirty-fifth Technical Conference*, 2020.

[320] Patil, S. U.; Radue, M. S.; Pisani, W. A.; Deshpande, P.; Xu, H.; Al Mahmud, H.; Dumitrică, T.; Odegard, G. M. *Computational Materials Science* **2020**, *185*, 109970.

[321] Pisani, W. A.; Radue, M. S.; Patil, S. U.; Odegard, G. M. *Composites Part B: Engineering* **2021**, *211*, 108672.

[322] Pisani, W. A.; Wedgeworth, D. N.; Roth, M. R.; Newman, J. K.; Shukla, M. K. *The Journal of Physical Chemistry C* **2021**, *125*(28), 15569–15578.

[323] Qi, B.; Zhang, Q. X.; Bannister, M.; Mai, Y. W. *Composite Structures* **2006**, *75*(1-4), 514–519.

[324] Radue, M. S.; Odegard, G. M. *Composites Science and Technology* **2018**, *166*, 20–26.

[325] Rahmat, M.; Hubert, P. *Composites Science and Technology* **2011**, *72*(1), 72–84.

[326] Ratna, D.; Manoj, N. R.; Varley, R.; Singh Raman, R. K.; Simon, G. P. *Polymer International* **2003**, *52*(9), 1403–1407.

[327] Rottler, J. *J Phys Condens Matter* **2009**, *21*(46), 463101.

[328] Schichtel, J. J.; Chattopadhyay, A. *Computational Materials Science* **2020**, *174*, 109469.

[329] Schroeder, J. A.; Madsen, P. A.; Foister, R. T. *Polymer* **1987**, *28*(6), 929–940.

[330] Shah, S.; Patil, S.; Deshpande, P.; Kashmari, K.; Odegard, G.; Maiaru, M. In *In: ICCM22 2019. Melbourne, VIC: Engineers Australia, 2019: 2732-2740.;* Engineers Australia, 2019.

[331] Shah, S.; Patil, S.; Deshpande, P.; Krieg, A.; Kashmari, K.; Mahmud, H. A.; King, J.; Odegard, G. M.; Maiaru, M. In *AIAA Scitech 2020 Forum*.

[332] Shah, S.; Patil, S.; Deshpande, P.; Krieg, A.; Kashmari, K.; Mahmud, H. A.; King, J.; Odegard, G. M.; Maiaru, M. In *AIAA Scitech 2020 Forum*.

[333] Shah, S. P.; Maiarù, M. *Polymers* **2021**, *13*(15), 2491.

[334] Shan, L.; Verghese, K. N. E.; Robertson, C. G.; Reifsnider, K. L. *J. Polym. Sci., Part B: Polym. Phys.* **1999**, *37*, 2815.

[335] Sharifian, A.; Baghani, M.; Odegard, G. M.; Wu, J.; van Duin, A. C. T.; Baniassadi, M. *Phys Chem Chem Phys* **2019**, *21*(43), 23880–23892.

[336] Shinde, D.; Emmanwori, L.; Kelkar, A. *Comparison of mechanical properties of EPON 862/W with and without TEOS electrospun nanofibers in nanocomposite;* 2014.

[337] Shokrieh, M. M.; Shokrieh, Z.; Hashemianzadeh, S. M. *Materials Design* **2014**, *64*, 96–101.

[338] Skourlis, T. P.; McCullough, R. L. *Journal of Applied Polymer Science* **1996**, *62*(3), 481–490.

[339] Soni, N. J.; Lin, P.-H.; Khare, R. *Polymer* **2012**, *53*(4), 1015–1019.

[340] Srinivasan, S. G.; van Duin, A. C. T.; Ganesh, P. *The Journal of Physical Chemistry A* **2015**, *119*(4), 571–580.

[341] Sun, L.; Warren, G. L.; O'Reilly, J. Y.; Everett, W. N.; Lee, S. M.; Davis, D.; Lagoudas, D.; Sue, H. J. *Carbon* **2008**, *46*(2), 320–328.

[342] Sun, Y.; Chen, L.; Cui, L.; Zhang, Y.; Du, X. *Computational Materials Science* **2018**, *143*, 240–247.

[343] Sundararaghavan, V.; Kumar, A. *International Journal of Plasticity* **2013**, *47*, 111–125.

[344] Tack, J. L.; Ford, D. M. *Journal of Molecular Graphics and Modelling* **2008**, *26*(8), 1269–1275.

[345] Tang, T.; Jagota, A.; Hui, C.-Y.; Glassmaker, N. J. *Journal of Applied Physics* **2005**, *97*(7), 074310.

[346] Tao, K.; Yang, S.; Grunlan, J. C.; Kim, Y.-S.; Dang, B.; Deng, Y.; Thomas, R. L.; Wilson, B. L.; Wei, X. *Journal of Applied Polymer Science* **2006**, *102*(6), 5248–5254.

[347] Teh, P. L.; Jaafar, M.; Akil, H. M.; Seetharamu, K. N.; Wagiman, A. N. R.; Beh, K. S. *Polym. Adv. Technol.* **2008**, *19*, 308.

[348] Wang, L.; Wang, K.; Chen, L.; He, C.; Zhang, Y. *Polymer Engineering Science* **2006**, *46*(2), 215–221.

[349] Wang, S.; Liang, Z.; Liu, T.; Wang, B.; Zhang, C. *Nanotechnology* **2006**, *17*(6), 1551–1557.

[350] Wheatley, B. B.; Odegard, G. M.; Kaufman, K. R.; Haut Donahue, T. L. *Comput Methods Biomech Biomed Engin* **2017**, *20*(6), 598–601.

[351] Wu, J.; He, J.; Odegard, G. M.; Nagao, S.; Zheng, Q.; Zhang, Z. *J Am Chem Soc* **2013**, *135*(37), 13775–85.

[352] Wu, J.; He, J.; Odegard, G. M.; Zhang, Z. *Nanoscale Res Lett* **2013**, *8*(1), 322.

[353] Wu, T. H.; Foyet, A.; Kodentsov, A.; van der Ven, L. G. J.; van Benthem, R. A. T. M.; de With, G. *Mater. Chem. Phys.* **2014**, *145*, 342.

[354] Yang, S.; Qu, J. *Polymer* **2012**, *53*(21), 4806–4817.

[355] Yu, M.-F.; Yakobson, B. I.; Ruoff, R. S. *The Journal of Physical Chemistry B* **2000**, *104*(37), 8764–8767.

[356] Yuan, Y.; Nie, A.; Odegard, G. M.; Xu, R.; Zhou, D.; Santhanagopalan, S.; He, K.; Asayesh-Ardakani, H.; Meng, D. D.; Klie, R. F.; Johnson, C.; Lu, J.; Shahbazian-Yassar, R. *Nano Lett* **2015**, *15*(5), 2998–3007.

[357] Zhang, R.; Ning, Z.; Xu, Z.; Zhang, Y.; Xie, H.; Ding, F.; Chen, Q.; Zhang, Q.; Qian, W.; Cui, Y.; Wei, F. *Nano Letters* **2016**, *16*(2), 1367–1374.

[358] Zhao, J.; Nagao, S.; Odegard, G. M.; Zhang, Z.; Kristiansen, H.; He, J. *Nanoscale Res Lett* **2013**, *8*(1), 541.

[359] Zhou, G.; Movva, S.; Lee, L. J. *J. Appl. Polym. Sci.* **2008**, *108*, 3720.

[360] Zhou, Y.; Pervin, F.; Lewis, L.; Jeelani, S. *Materials Science and Engineering: A* **2007**, *452-453*, 657–664.

Appendix A

Supporting Information for

Chapter 2

A.1 Partial Charges assigned through PCFF-IFF

This section details the partial charges on all the atoms of the fluorinated and non-fluorinated polyimides. **Figures A.1** and **A.2** shows the molecular structure and corresponding atom numbers for both systems. **Table A.1** lists the atom numbers, corresponding atom type, and partial charges on both polyimide systems modeled in this work.

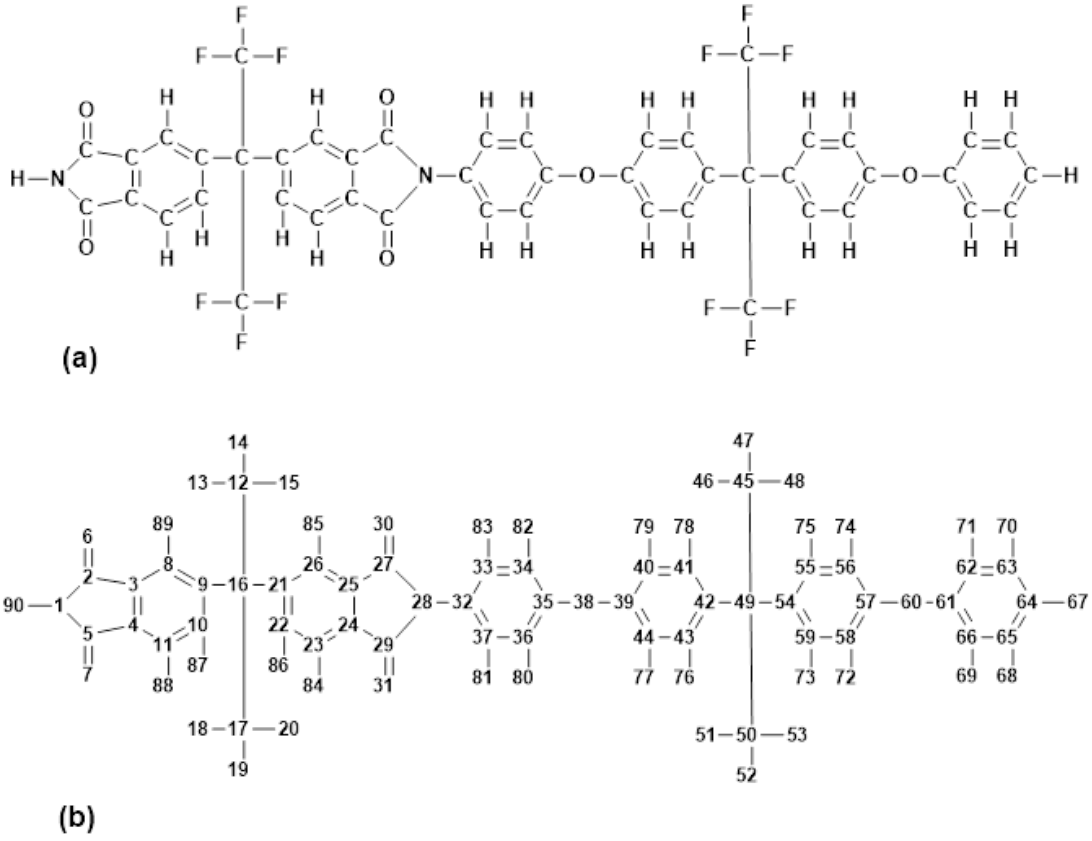

Figure A.1: Fluorinated polyimide (a) Molecular structure, (b) Corresponding atom number

A.2 Densification simulation

This section includes a representative snapshot of the densification simulation for the non-fluorinated polyimide model of 46 % mass fraction. **Figures A.3** shows the top view snapshots at 0^{th}, 5^{th} and 45^{th} timestep rendered using OVITO software package. The video clip of the simulation is also included. The clip shows that, the molecules displace and start dynamic motion as soon as the simulations starts.

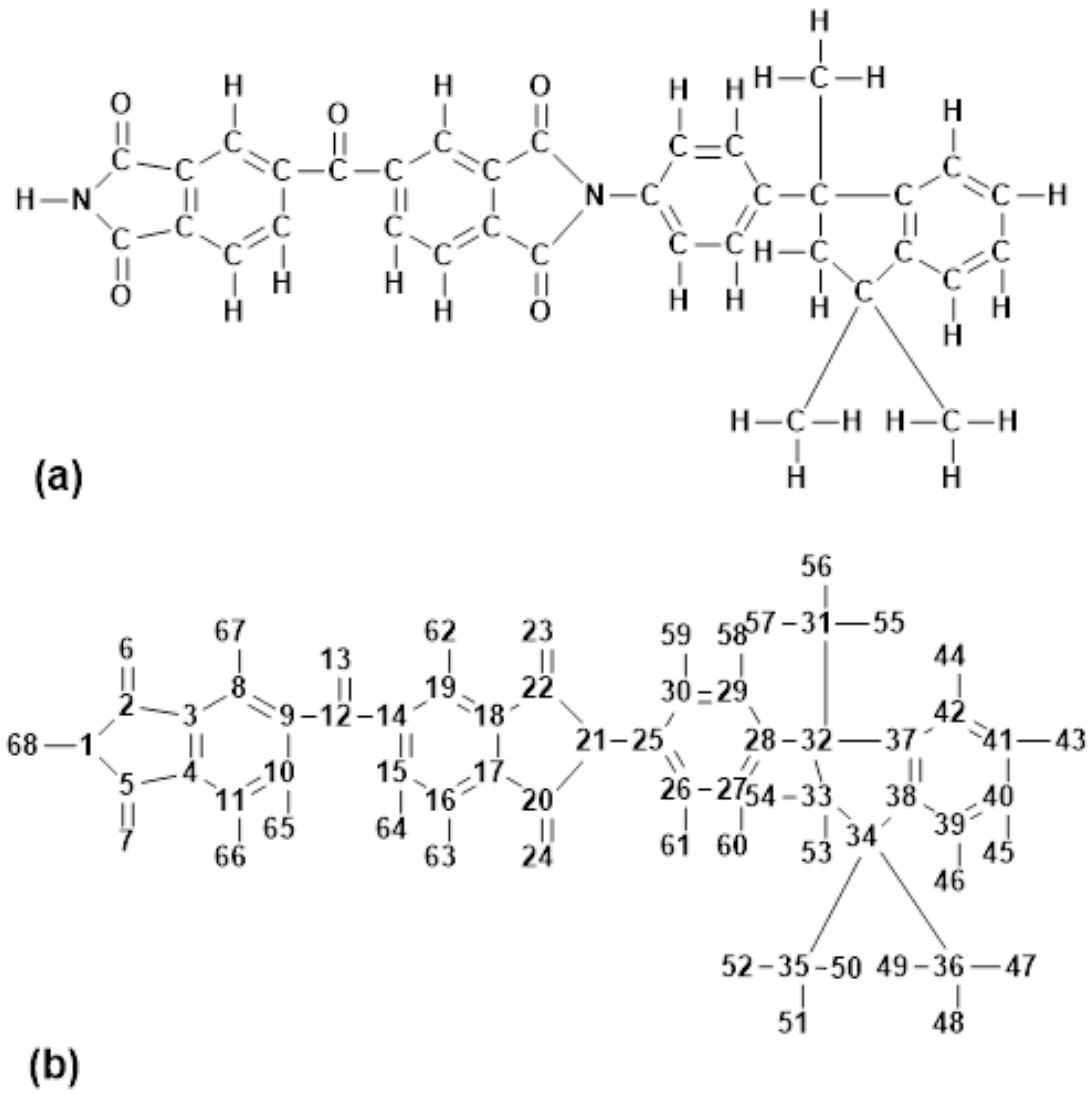

Figure A.2: Non-fluorinated polyimide (a) Molecular structure, (b) Corresponding atom number

A.3 Polymerization

Table A.2 details the polymerization parameters tested to polymerize the fluorinated polyimide. All the simulations listed helped guide the selection of parameters

Table A.1
Partial Charges assigned by PCFF-IFF for fluorinated and non-fluorinated polyimides.

Fluorinated polyimide			**Non-fluorinated polyimide**		
Atom number	**Atom type**	**Partial charges (Coulomb)**	**Atom number**	**Atom type**	**Partial charges (Coulomb)**
1	n	-0.4395	1	n	-0.4395
2	c_1	0.531	2	c_1	0.531
3	cp	0	3	cp	0
6	o_1	-0.531	6	o_1	-0.531
8	cp	-0.1268	8	cp	-0.1268
12	c	0.75	12	c_1	0.531
13	f	-0.25	13	o_1	-0.531
67	hc	0.1268	67	hc	0.1268
90	h*	0.4395			

described in the main document to achieve maximum polymerization. It can be seen from the table that the temperature of 650 K and cut-off distance of 6 gave maximum polymerization of 74 %. A similar set of parameters was used to polymerize the non-fluorinated polyimide to ensure consistency in predicting results.

Table A.2
Polymerization simulation details for fluorinated polyimide.

Temperature (K)	**Cutoff distance ($\AA$)**	**Probability**	**Simulation time (ns)**	**Percent Polymerization**
650	6	0.99	4	74
650	7	0.99	4	70
800	6	0.99	4	72

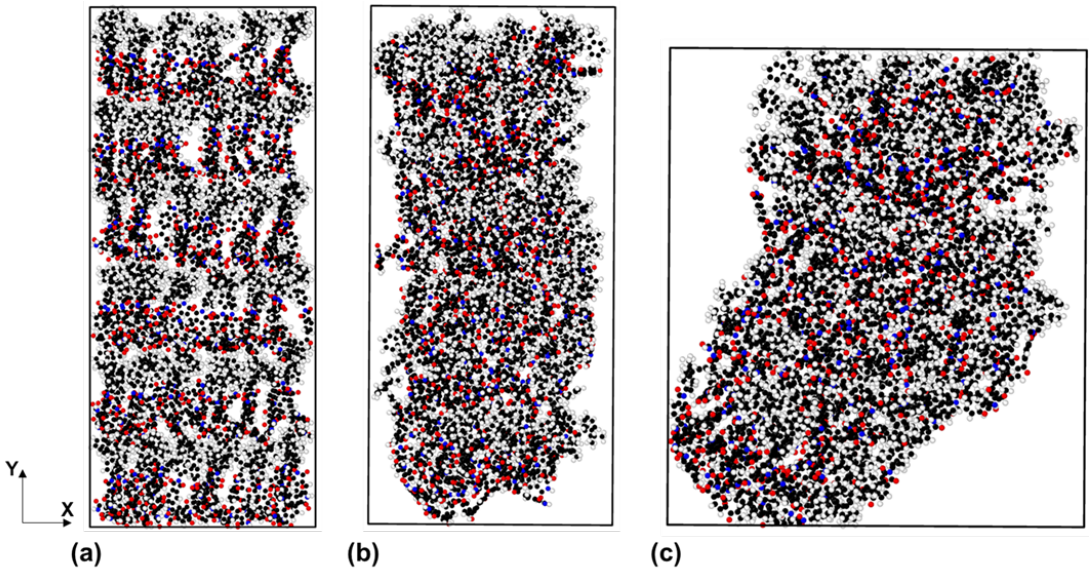

Figure A.3: Top view snapshots of densification of non-fluorinated polyimide (46 % mass fraction) at (a) 0^{th}, (b) 5^{th} and (c) 45^{th} timesteps.

A.4 Friction simulations results

This section shows the friction simulation results in terms of shear stress. The shear stress is calculated as the ratio of friction force by the contact area between the flCNT and polyimides.

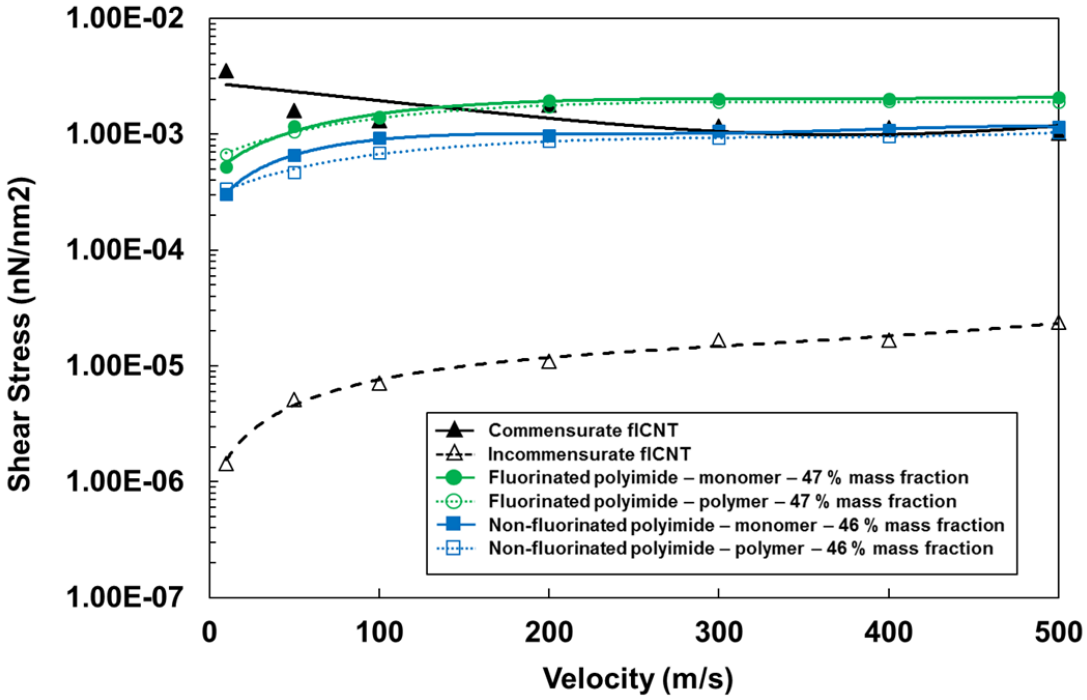

Figure A.4: Comparison of bare flCNT and flCNT-polyimide shear stress for both fluorinated and Non-fluorinated polyimides. All stresses are plotted for a range of sliding velocities. Two cases of flCNT-flCNT sliding are shown, namely, commensurate and incommensurate.

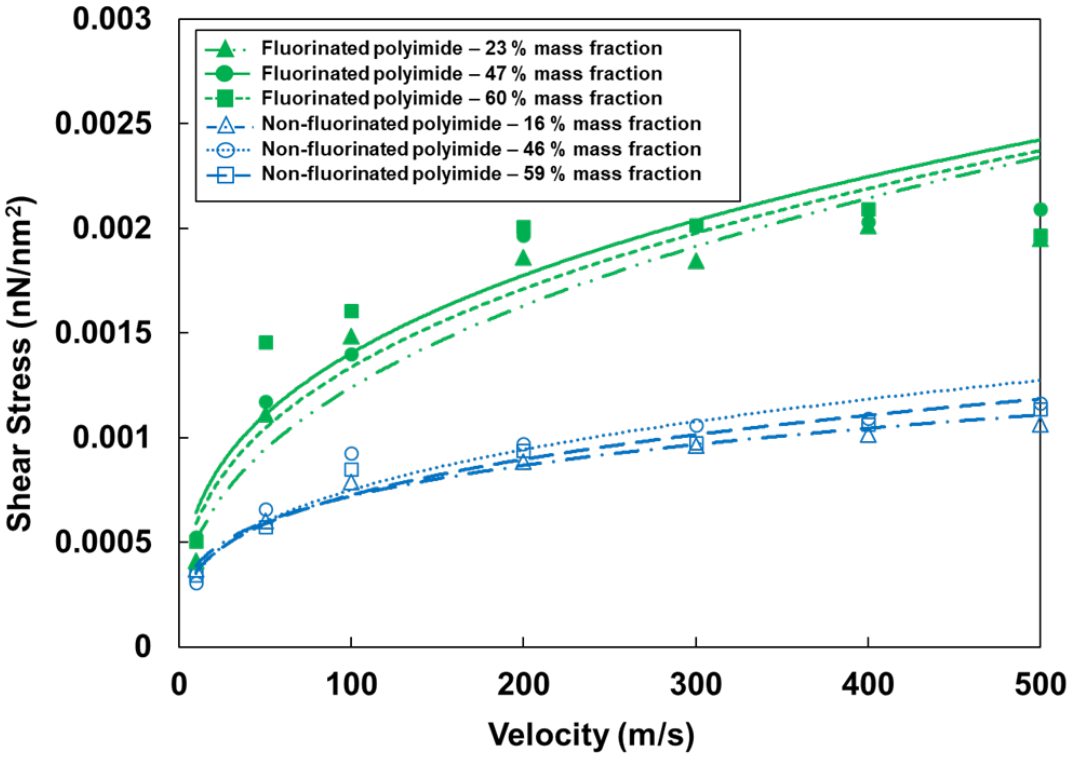

Figure A.5: Comparison of shear stress versus velocity between polymerized fluorinated and non-fluorinated polyimides for varying mass fractions.

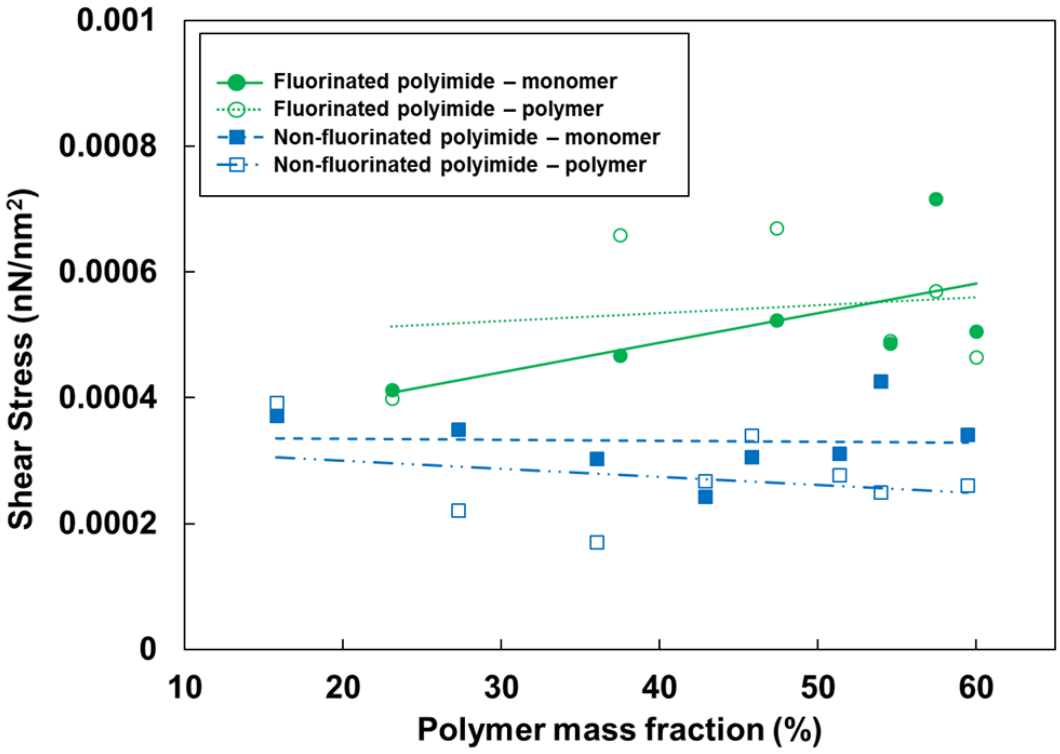

Figure A.6: Effect of varying mass fraction on flCNT-polyimide shear stress for both fluorinated and non-fluorinated polyimides. Friction simulations were performed with a sliding velocity of 10 m/s.

Appendix B

Supporting Information for

Chapter 4

B.1 Total energy terms in IFF-R and ReaxFF

This section details the key difference between the total energy terms in IFF-R [12, 13] and ReaxFF [306] force fields.

The total energy of the system for IFF-R [13] is calculated using:

$$
\begin{aligned}
E_{total\ energy} &= E_{morse\ bond\ energy} + E_{angle\ bending\ energy} \\
&= E_{1-3\ term\ torsional\ energy} + E_{cross\ or\ improper\ terms\ energy} \\
&= E_{colombic\ energy} + E_{vdW\ energy}
\end{aligned}
\tag{B.1}
$$

The total energy of the system for ReaxFF [306] is calculated using:

$$
\begin{aligned}
E_{total\ energy} &= E_{bond\ order\ and\ bond\ energy} \\
&= E_{lone\ pair\ energy} \\
&= E_{overcoordination} + E_{undercoordination} \\
&= E_{angle\ energy} + E_{penalty\ energy} \\
&= E_{three-body\ conjugate\ term\ energy} + E_{torsion\ rotation\ barriers\ energy} \\
&= E_{four-body\ conjugate\ term\ energy} + E_{hydrogen\ bond\ interaction\ energy} \\
&= E_{correction\ for\ C_2} + E_{triple\ bond\ energy\ correction} \\
&= E_{taper\ correction} + E_{colombic\ energy} + E_{vdW\ energy}
\end{aligned}
\tag{B.2}
$$

The key difference between the energy terms for both reactive force fields is that the inclusion of correction terms in ReaxFF greatly reduces the computational efficiency of the force field and thus imposes size-restrictions on the MD models as compared to IFF-R.

B.2 Sequential v/s Non-sequential crosslinking

This section details the comparison between the sequential and non-sequential crosslinking strategies as described in **Section 4.2.3** and shown in **Figure 4.2** in the main manuscript. Both the strategies are compared based on mass density, post-gelation volumetric shrinkage, and bulk modulus.

Figure B.1 shows the mass density comparison where the error bars represent the standard deviation associated with the MD predictions represented by the filled circles. The non-sequential crosslinking predicted slightly higher mass densities between $\phi = 0$ to 0.5 and then it slightly decreases as compared to sequential strategies. Also, the non-sequential strategy shows higher standard deviations and the maximum crosslinking density achieved was limited to 0.9. For the sequential crosslinking, a highest crosslinking density of 0.95 was achieved and the mass density gradually increases with crosslinking density.

Figure B.2 shows the post-gelation volumetric shrinkage comparison where the error bars represent the standard deviation associated with the MD predictions represented by the filled circles. The non-sequential crosslinking predicted negative shrinkage and shows higher standard deviations with no clear trend between shrinkage and crosslinking density. For the sequential crosslinking, post-gelation shrinkage linearly increases

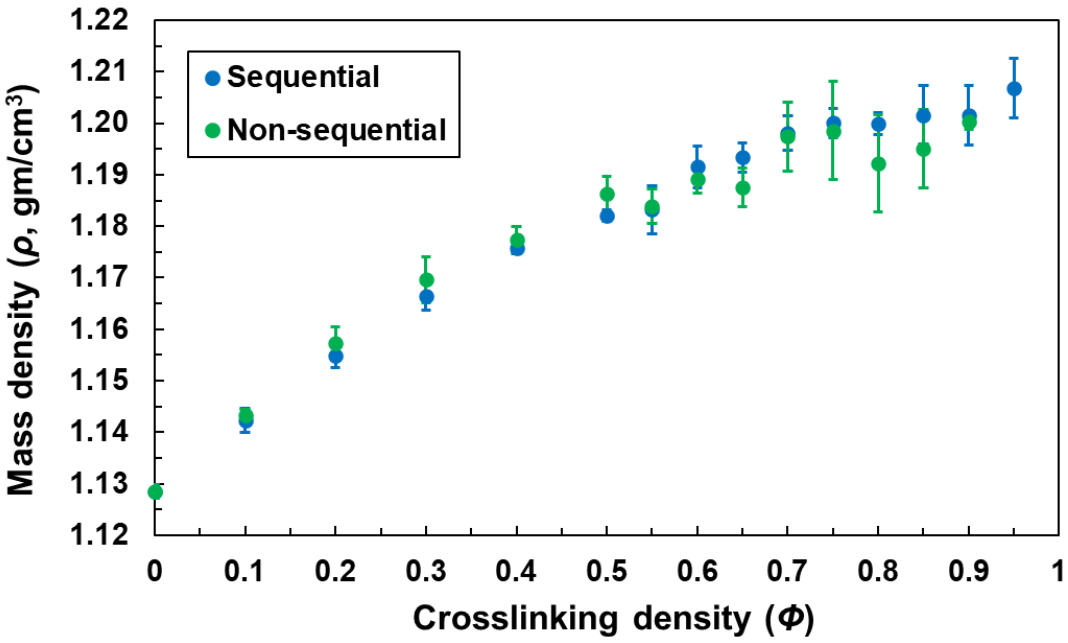

Figure B.1: Predicted mass density as a function of crosslinking density at room temperature for sequential and non-sequential crosslinking strategies.

with crosslinking density with good agreement with experimental measurement.

Figure B.3 shows the bulk modulus comparison where the error bars represent standard deviation associated with the MD predictions represented by the filled circles. The non-sequential crosslinking predicted slightly higher moduli between $\phi = 0$ to 0.55 with a slight decrease thereafter as compared to sequential strategies. Also, the non-sequential strategy shows higher standard deviations as compared to sequential crosslinking. Both strategies show a gradual increase in bulk modulus with increases in crosslinking density.

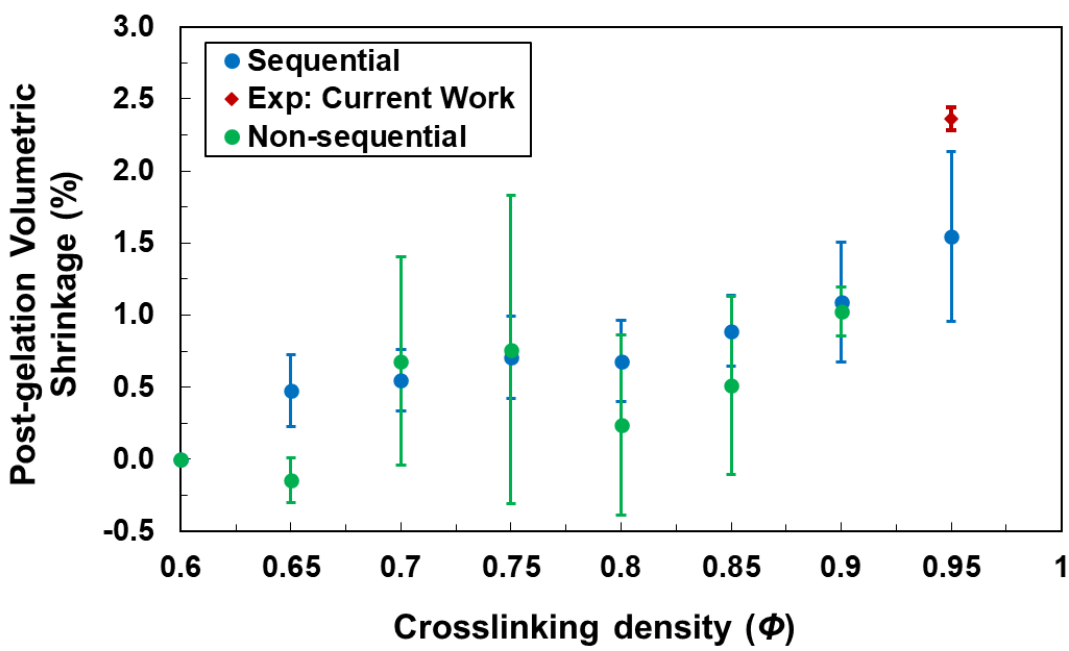

Figure B.2: Predicted post-gelation volumetric shrinkage as a function of crosslinking density at room temperature for sequential and non-sequential crosslinking strategies.

The differences in the properties between the two strategies is because in non-sequential crosslinking, the network is newly formed and different for each crosslinking density. Whereas in sequential crosslinking the network gradually evolves with increasing crosslinking density thus mimicking the experimental curing of polymers.

B.3 Experimental Shrinkage Measurements

This section includes the plots of experimentally measured post-gelation volumetric shrinkage as a function of time as shown in **Figure B.4** and as a function of degree of

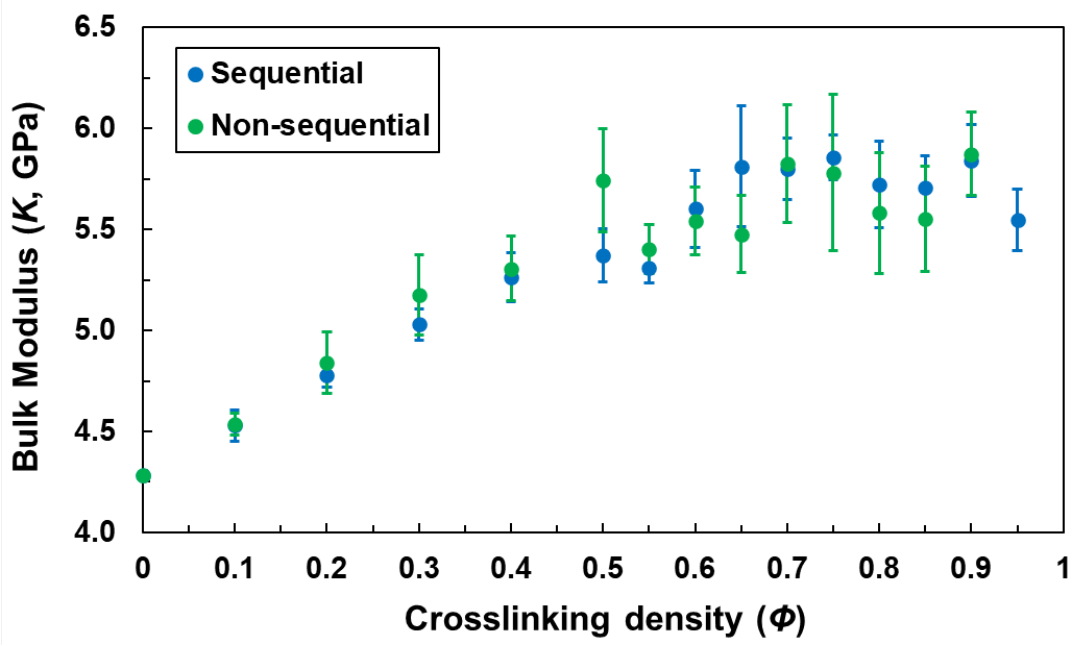

Figure B.3: Predicted bulk modulus as a function of crosslinking density at room temperature for sequential and non-sequential crosslinking strategies.

cure as shown in **Figure B.5**. The test is performed at two isothermal temperatures of 150 $^{\circ}C$ and 170 $^{\circ}C$. Each curve is an average of 2 samples tested.

B.4 Mechanical Property Predictions

This section details the procedure implemented to predict mechanical properties using the MD simulations for each crosslinking density.

The bulk modulus (K) was predicted by subjecting all the MD models at specific crosslinking density to an NPT simulation at 300 K, 5000 atm for 1 ns and another

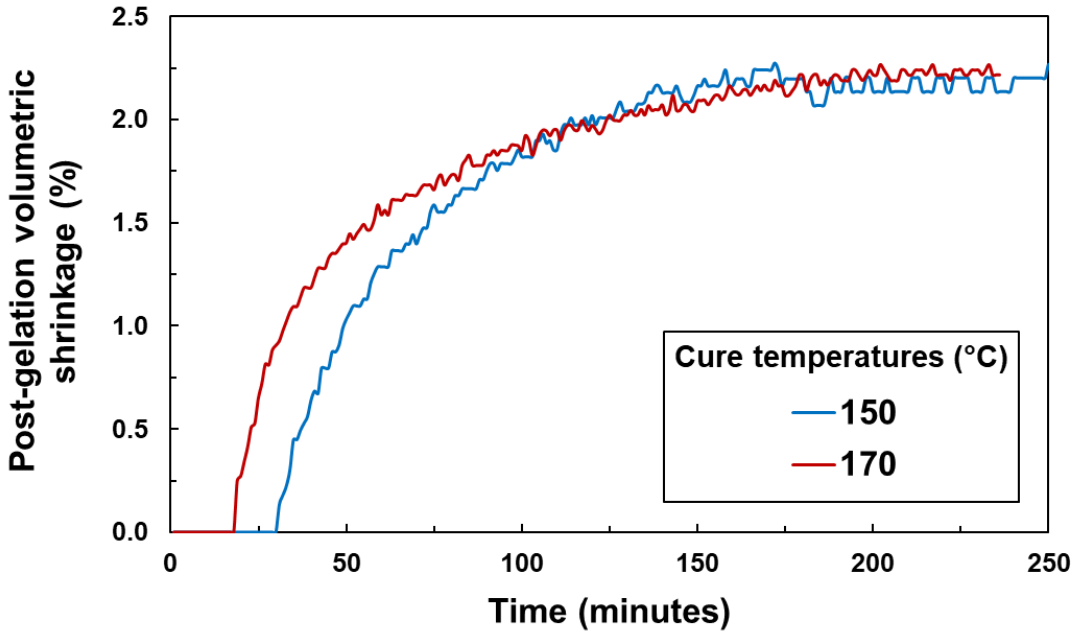

Figure B.4: Post-gelation volumetric shrinkage as a function of cure time.

NPT simulation at 300 K, 1 atm for 1 ns. The volume (V) was recorded during these simulations and then K was calculated as described elsewhere [132] using **Equation B.3**. The shear modulus (G) was predicted from shear deformations where all the MD models were sheared in the yz, xy, xz planes [83] at 300 K and strain rate of $2{\times}10^{8}$ s^{-1}. Using the results from these simulations, a shear stress-strain curve was plotted for each shearing plane and a bilinear breakpoint6 was determined by observing the strain at which the slope changed significantly. The shear modulus was calculated as the slope of the linear line before the breakpoint. The Young's modulus (E) and Poisson's ratios (ν) for each MD model were determined from the corresponding values of bulk modulus and the average shear modulus using standard isotopic elasticity equations [133] as shown in **Equation B.4** and **B.5**.

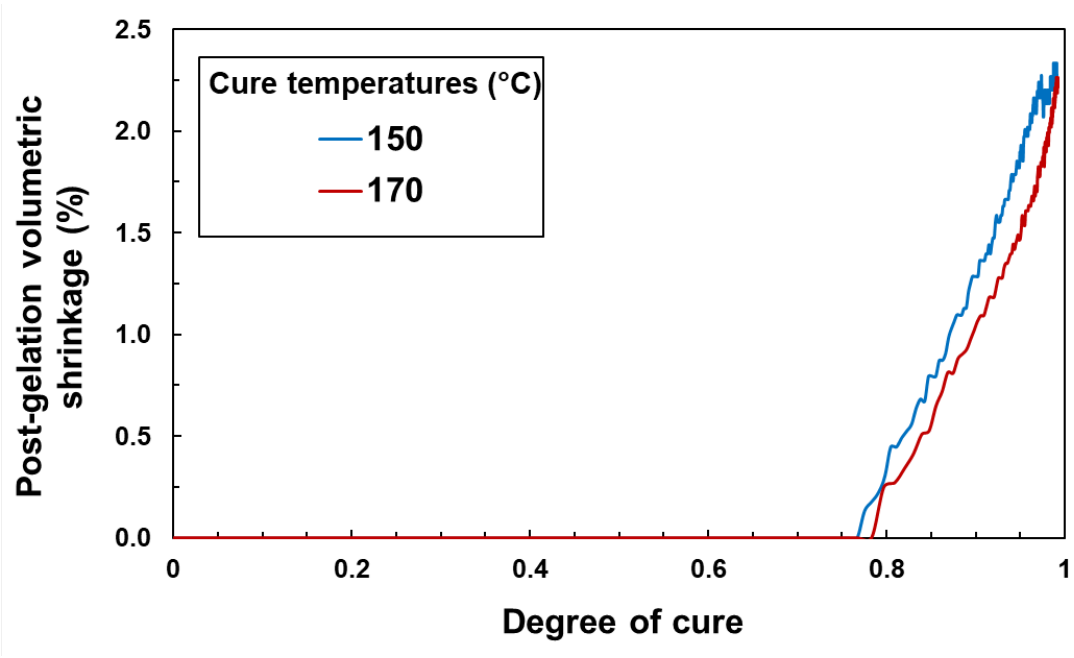

Figure B.5: Post-gelation volumetric shrinkage as a function of degree of cure.

$$K = -V_o \left(\frac{dP}{dV} \right) \tag{B.3}$$

$$E = \frac{9KG}{3K + G} \tag{B.4}$$

$$\nu = \frac{3K - E}{6K} \tag{B.5}$$

The yield strength was predicted from the von Mises stress (σ_{vM}) from the individual stress components obtained from the shear deformation simulations using **Equation**

B.6:

$$\sigma_{\mathrm{vM}} = \frac{1}{2}\sqrt{\left[(\sigma_x-\sigma_y)^2+(\sigma_y-\sigma_z)^2+(\sigma_z-\sigma_x)^2+6\left(\tau_{xy}^2+\tau_{xz}^2+\tau_{yz}^2\right)\right]} \qquad \text{(B.6)}$$

The von Mises stress-shear strain curve was plotted, and the yield strength was the corresponding strength at the same breakpoints as described above for the shear modulus. The yield strength was determined for each replicate and shearing plane.

Appendix C

Computational Resource Information

Superior (generation 1.0 and generation 2.0) and *Portage* high-performance computing clusters at Michigan Technological University were used to perform all MD simulations to predict properties of neat polymers and their composites presented in this work. Following boilerplate description regarding the clusters and their availability for usage in research was taken form the Michigan Tech website.

C.1 Boilerplate Description

Michigan Tech's shared high-performance computing infrastructure, *Superior*, is available to all researchers. It has the following computing and storage components:

1. Generation 1.0 (acquired between 2013/06 - 2015/10)
   (a) 92 CPU compute nodes - each having 16 CPU cores (Intel Xeon E5-2670 2.60 GHz) and 64 GB RAM - providing 30 TFLOPS
   (b) 4 CPU compute nodes - each having 24 CPU cores (Intel Xeon E4-2680 2.50 GHz) and 256 GB RAM - providing 2 TFLOPS
   (c) 5 GPU compute nodes - each having 16 CPU cores (Intel Xeon E5-2670 2.60 GHz), 64 GB RAM and 4 NVIDIA Tesla M2090 GPUs - providing 13 TFLOPS
   (d) 3 storage nodes each with 32 TB usable space
2. Generation 2.0 (acquired between 2017/06 - 2018/08)
   (a) 85 CPU compute nodes - each having 32 CPU cores (Intel Xeon E5-2683 2.10 GHz) and 256 GB RAM - providing 91 TFLOPS

Portage is another shared high-performance computing infrastructure and a miniature version of *Superior*. Intended primarily for testing, educational (course work and/or senior design projects) and gateway/preliminary research projects involving

non-confidential/non-sponsored data, *Portage* has 3 TFLOPS of CPU and 2 TFLOPS of GPU computing capacity with hardware identical to *Superior*'s generation 1.0.

Superior and *Portage* have a Gigabit ethernet back-end network that serves the administrative needs, and a 56 Gb/s InfiniBand network that serves the computing needs. They are available for all researchers at Michigan Tech via a brief proposal, very much similar to that of NSF XSEDE.

Researchers can get help with hardware specification and acquisition, software acquisition and licensing, compilation, installation, integration with the queuing system, running benchmarks, developing computational workflows, and necessary end-user training.

Appendix D

Letters of Permission

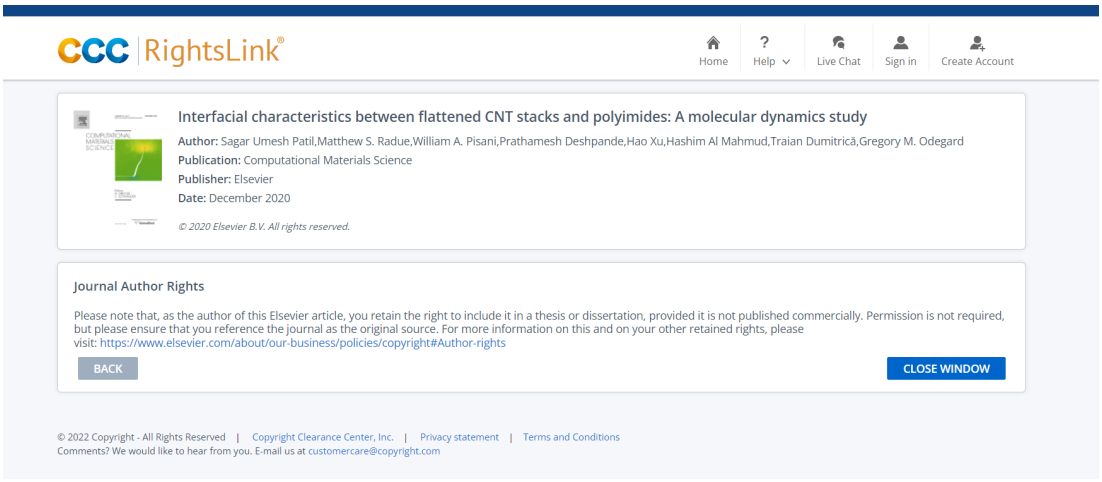

Figure D.1: Letter of permission from Computational Material Science

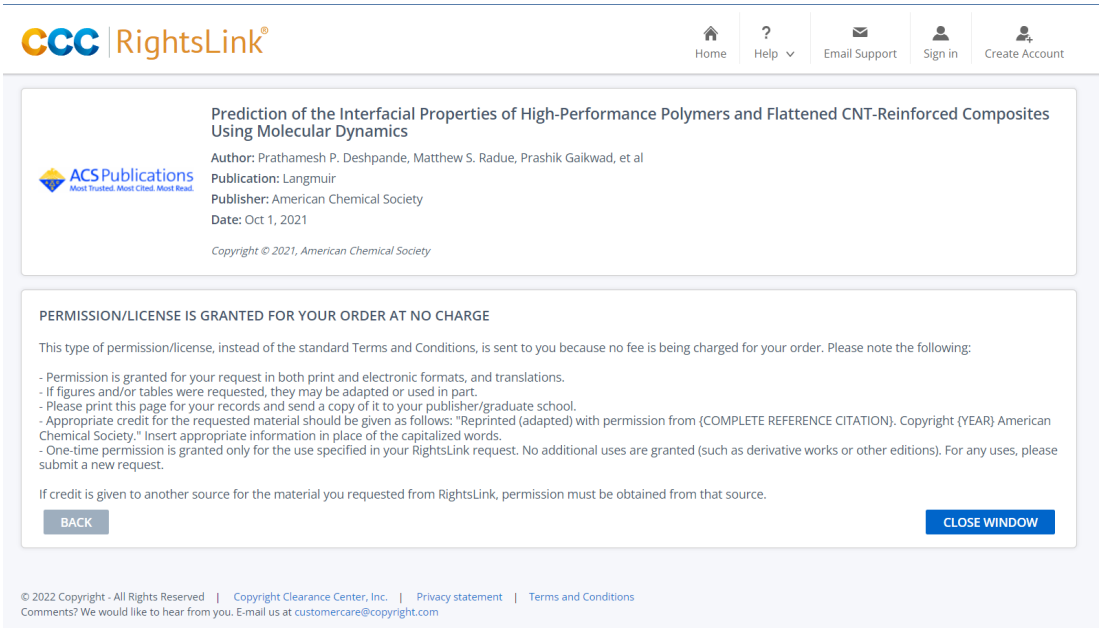

Figure D.2: Letter of permission from Langmuir

Figure D.3: Letter of permission from Composites Part B: Engineering

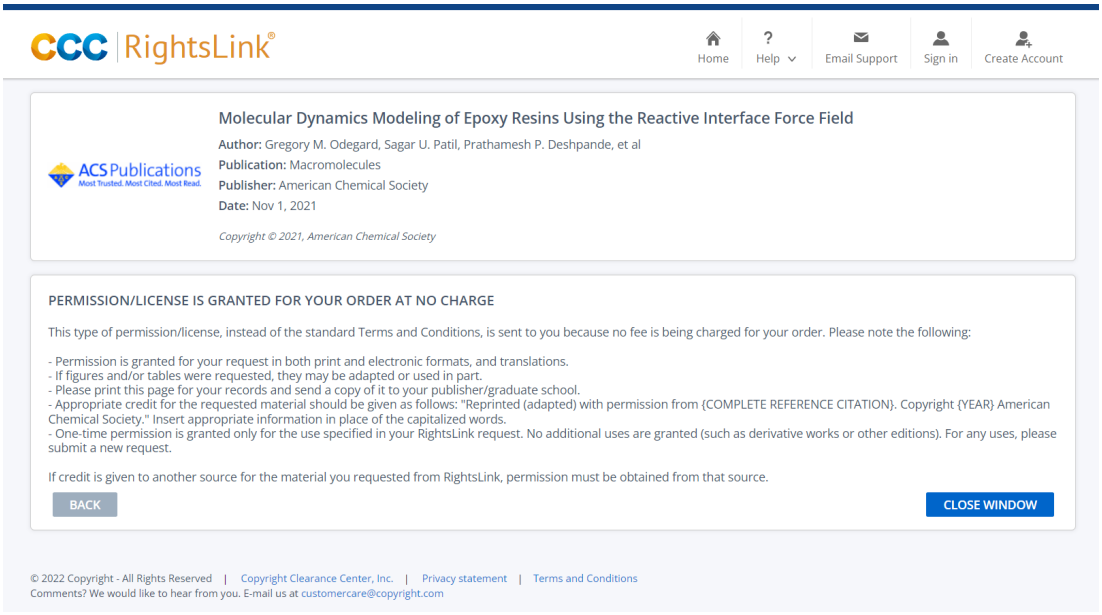

Figure D.4: Letter of permission from Macromolecules

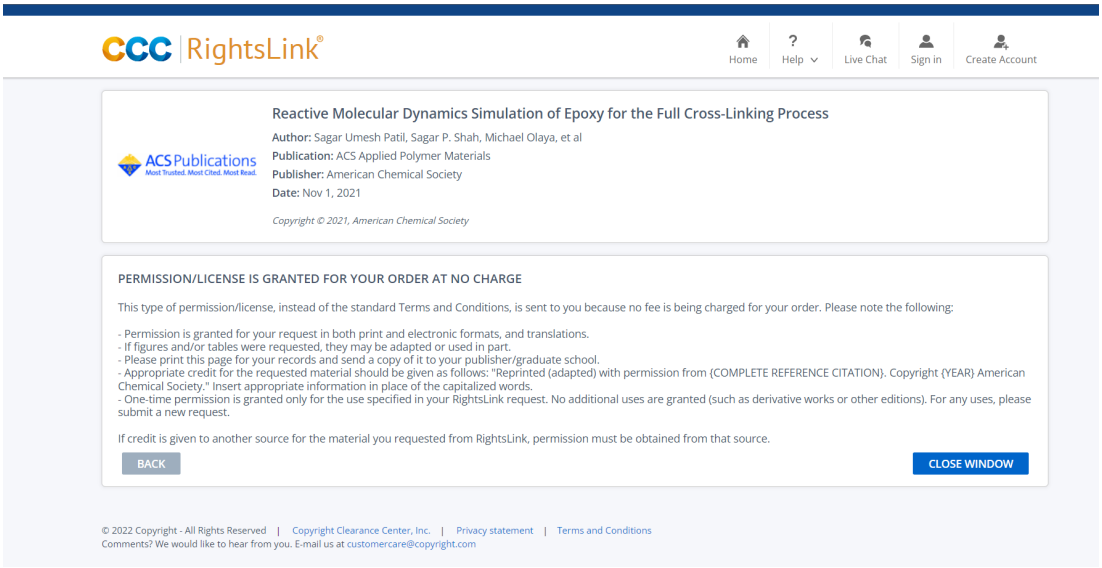

Figure D.5: Letter of permission from ACS Applied Polymer Materials